THE DRIVEN AND STOCHASTIC DYNAMICS OF MICRO AND NANOSCALE CANTILEVERS IN VISCOUS FLUID AND NEAR A SOLID BOUNDARY

BY

MATTHEW T. CLARK

Dissertation submitted to the Faculty of the
Virginia Polytechnic Institute and State University
in Partial Fulfillment of the Requirements for the Degree of
Doctor of Philosophy
in
Mechanical Engineering

Mark R. Paul, Chair
Scott T. Huxtable
Mark A. Stremler
Danesh K. Tafti
Brian Vick

October 24, 2008
Blacksburg, Virginia

Keywords: fluid dynamics, atomic force microscopy, fluctuation-dissipation theorem, actuation, detection

Abstract

THE DRIVEN AND STOCHASTIC DYNAMICS OF MICRO AND NANOSCALE CANTILEVERS IN VISCOUS FLUID AND NEAR A SOLID BOUNDARY

BY

MATTHEW T. CLARK

Micro and nanoscale systems are rapidly evolving to improve the resolution of experimental measurements. Experiments involving such small scale devices are difficult and expensive, and the available analytical theory to describe their dynamics is idealized. The dynamics of microscopic cantilevers in fluid are complicated and include significant contributions from many sources in an actual experiment. Some examples are: complex cantilever geometries, near-wall effects, thermal and external actuation techniques, and a variety of measurement techniques. Numerical simulations are a powerful approach to describe the dynamics of micro and nanoscale systems for the precise conditions of experiment. This thesis provides a numerical approach capable of addressing these inherent challenges and quantifies the dynamics of microscopic cantilevers in fluid for experimentally relevant conditions.

A thermodynamic approach based upon the fluctuation-dissipation theorem allows for the calculation of stochastic dynamics from deterministic dynamics. Using numerical simulations, the thermal motion can be described for the precise conditions of experiment. It is found that the measured dynamics of cantilevers differs depending on the quantity being measured. In particular, the dynamics of displacement and angle of the cantilever tip distribute energy differently to the higher flexural modes. The externally driven dynamics of microscale cantilevers in fluid are also considered. The driven dynamics are calculated using numerical

simulations of the cantilever response to a force impulse. It is found that the driven dynamics depend upon the type of actuation in addition to the quantity measured. A comparison of the driven dynamics to the corresponding stochastic dynamics yields insight into the nature of the Brownian force acting on the cantilever.

Another experimentally relevant condition is the use of cantilevers with V-shaped planforms in fluid. The resulting flow field is three-dimensional and complex in contrast to what is found for a long and slender rectangular cantilever. Despite the flow complexity, the stochastic and driven dynamics of the fundamental mode can be predicted using a two-dimensional model with an appropriately chosen length scale. An experimentally motivated magnetomotive actuation technique is investigated. Results show that this approach generates power spectra nearly equivalent to the noise spectra. Furthermore, the case of a V-shaped cantilever in fluid and oscillating in proximity of a solid boundary is investigated. In the presence of a solid surface the fluid damping and added mass of fluid on the cantilever are larger than for a cantilever far from boundaries. This results in a lower frequency and quality factor for the fundamental resonance. This can impede experimental efforts because broad peaks lack distinct features that can be used to identify experimental signals.

An option to overcome the large viscous damping is to take advantage of higher modes of cantilever oscillation. The higher frequency oscillations of the higher modes generate a smaller viscous boundary layer and have a reduced added mass. As a result, the quality factor increases with increasing mode number. The frequency dependence of the fluid dynamics around a fluctuating microscale cantilever is also studied. The mass of fluid entrained by the cantilever and the viscous damping quantify the interaction of a cantilever with the

surrounding fluid and are computed. Analytical expressions for these parameters are derived for moderate mode number. The techniques and findings of this thesis have broad applicability to a wide range of micro and nanotechnologies that rely upon understanding the dynamics of small scale structures in fluid.

Library Rights Statement

In presenting the dissertation *The driven and stochastic dynamics of micro and nanoscale cantilevers in viscous fluid and near a solid boundary* in partial fulfillment of the requirements for an advanced degree at Virginia Polytechnic Institute and State University, I agree that the Library shall make it freely available for inspection. I further agree that permission for copying as provided for by the Copyright Law of the U.S. (Title 17, U.S. Code) of this dissertation for scholarly purposes may be granted by the Librarian. It is understood that any copying or publication of this dissertation for financial gain shall not be allowed without my written permission.

I hereby grant permission to the VPI&SU Library to copy my dissertation for scholarly purposes.

October 24, 2008

Acknowledgments

I wish to acknowledge the many useful interactions I have had with members of the scientific community. This includes Jessica Arlett and Igor Bargatin of the Roukes group at Caltech and Melanie Favre and Sergey Sekatskii in Switzerland. In addition I want to thank the faculty of the Mechanical Engineering, Engineering Science and Mechanics, Physics and Math departemnts at Virginia Tech. I also send much appreciation to the professors at Rose-Hulman Institute of Technology for preparing me for graduate school. Most of all I wish to thank Mark Paul for providing guidance and encouragement throughout my graduate student career and my family and fiancée for their constant support.

Table of Contents

Abstract ii

Acknowledgments vi

Table of Contents vii

List of Tables x

List of Figures xiv

Nomenclature xxvi

1 Introduction 1

1.1 Research Motivation 1

1.2 Brief History of Science 2

1.3 Experimental Techniques: Microscopy Cantilevers 8

1.4 Open Challenges for Microscopic Cantilevers 11

1.4.1 Microscale Cantilevers in a Viscous Fluid 12

1.4.2 Externally Driven Dynamics of Microscale Cantilevers . . 15

1.4.3 The Fluctuations of a Microscale Cantilever in Fluid and Near a Solid Boundary 17

1.4.4 Fluid Dynamics Induced by Fluctuations in Higher Flexural Modes 18

1.5 Fluctuation-Dissipation Theorem 19

2 Dynamics of Micro and Nanoscale Cantilevers in Fluid 20

2.1 Chapter Overview 20

2.2 Stochastic Cantilever Dynamics: Linear Response Theory 21

2.3 Approximate Dynamics of a Cantilever in Fluid: Infinite Cylinder Theory 26
2.3.1 Cantilever Modal Frequencies and Mode Shapes 28
2.3.2 Analytical Description of Cantilever Dynamics in a Viscous Fluid 32
2.3.3 Thermally Driven Cantilever Fluctuations 34
2.3.4 Externally Driven Cantilever Fluctuations 40
2.4 Complete Cantilever Dynamics: Numerical Simulations 45
2.4.1 Thermally Driven Cantilever Fluctuations 45
2.4.2 Externally Driven Cantilever Fluctuations 46

3 Cantilever Tip-Deflection and Tip-Angle Formulations 48
3.1 Chapter Overview 48
3.2 Cantilever Response: Tip-Force and Tip-Torque 49
3.3 Modal Energy Distribution 52

4 The Stochastic and Driven Dynamics of a Rectangular Microscopic Cantilever in Fluid 55
4.1 Chapter Overview 55
4.2 The Stochastic Dynamics of a Rectangular Cantilever in Viscous Fluid 55
4.3 Ratio of the Driven to Noise Spectra for a Rectangular Cantilever in Fluid 61

5 The Stochastic and Driven Dynamics of V-shaped Cantilevers in Fluid 65
5.1 Chapter Overview 65
5.2 The Dynamics of the Veeco V-shaped Cantilever in Fluid 66

5.2.1 The Stochastic Dynamics of the Veeco V-shaped Cantilever in Fluid 72
5.3 Comparing the Driven and Noise Spectra for the V-shaped Olympus Cantilever 75

6 The Dynamics of Cantilevers in Fluid Near a Planar Boundary 79
6.1 Chapter Overview 79
6.2 Effects of a Solid Boundary 79

7 Numerical Resolution Study for Higher Modes 85
7.1 Chapter Overview 85
7.2 Analytical Predictions 85
7.3 Numerical Simulations of Multiple Cantilever Modes 89
7.3.1 Effects of Diminishing Time Step 92
7.3.2 Effects of Improving Spatial Resolution 94
7.3.3 Effects of Increasing Domain Size 95
7.4 Numerical Simulation of Individual Cantilever Modes 97

8 Quantifying the Mass Loading and Viscous Damping 100
8.1 Chapter Overview 100
8.2 Fluid Dynamics Around a Cantilever 100
8.3 Fluid Dynamics for Three-Dimensional Rectangular Cantilevers 102
8.4 Fluid Dynamics around a Cantilever for Multiple Modes 105

9 Conclusions 107

List of References 110

List of Tables

1 The time scale τ, displacement resolution X_{MIN}, and force sensitivity F_{SENS} for three small scale measurement devices. Values taken from [15, 36]. 12

2 The assumptions made for analytical and numerical calculations of cantilever noise and power spectra. 24

3 The resonant frequency in vacuum, effective mass, and spring constant for the first five modes of a cantilevered beam. The effective mass is constant for all modes, $m_{e,n} = 6.65$ng. 28

4 Summary of the cantilever geometries and material properties. (1) The rectangular cantilever. (2) The Veeco MLCT Type E microlever [76]. (3) The Olympus OMCL-TR400PSA lever. The geometry is given by the cantilever length L, width w, and height h. For the Veeco and Olympus cantilevers the total length between the two arms at the base is $b = 161.64\mu$m and $b = 106\mu$m. The cantilever spring constant k, torsional spring constant k_t, and resonant frequency in vacuum f_0 are determined using finite element numerical simulations. The cantilevers are immersed in water with density $\rho = 997$ kg/m^3 and dynamic viscosity $\mu_f = 8.59 \times 10^{-4}$ kg/m-s. 30

5 Mode coefficients for an applied force or an applied torque at the tip of a rectangular cantilever. 51

6 Energy ratios for each mode of a rectangular cantilever for an applied force or an applied torque at the tip. 52

7 The magnitude of stochastic fluctuations in tip-deflection and in tip-angle for the rectangular (1) and V-shaped (2) cantilevers. These values were obtained from numerical simulations simulations of the beams in vacuum. 55

8 The peak frequency and quality factor of the fundamental mode of the C2 rectangular cantilever in water determined by finite element simulations using the thermodynamic approach. (1) is computed using the cantilever tip-displacement due to the removal of a step force. (2) is computed using the cantilever tip-angle due to the removal of a point-torque. The frequency result is normalized by the resonant frequency in vacuum ω_0. Using the infinite cylinder approximation with a radius of $w/2$ the analytical predictions are $Q = 3.24$ and $\omega_f/\omega_0 = 0.34$. 59

9 The peak frequency and quality factor of the fundamental mode of the V-shaped cantilever determined by finite element simulations using the thermodynamic approach. (1) is computed using the cantilever tip-displacement due to the removal of a step force. (2) is computed using the cantilever tip-angle due to the removal of a point-torque. The third line represents theoretical predictions using the geometry of an equivalent rectangular beam given by $(L, 2w, h)$. The frequency result is normalized by the resonant frequency in vacuum ω_0. 70

10 The geometry of the equivalent rectangular beam that yields the exact values of k, ω_f, and Q for the V-shaped cantilever that have been determined from full finite-element numerical simulations. The length, width, and height of the equivalent beam (L', w', h') are calculated using Eqs. (103)-(104) and are normalized by the values of (L, w, h) for the V-shaped cantilever given in Table 4. . 72

11 Separations, quality factors, and resonant frequencies for the 8 simulations with different wall-cantilever separations. A † indicates results obtained by measuring tip-angle. 81

12 The geometry of the high aspect ratio cantilever used to investigate higher mode dynamics. The aspect ratios are $L/w = 20$ and $w/h = 10$ so that infinite cylinder assumptions are valid. Also shown are the bulk spring constant k and resonant frequency in vacuum f_0. The cantilever is submerged in fluid with density of ρ=997 kg/m^3 and viscosity of $\mu_f = 1 \times 10^{-5}$kg/m-s. 88

13 Peak frequency, quality factor, and Stokes length for the first two modes of the high aspect ratio cantilever in low viscosity fluid ($\rho = 997$kg/m^3, $\mu_f = 1 \times 10^{-5}$kg/m-s). 89

14 Peak frequency and quality factor for the first two modes of the cantilever as calculated from numerics for three different time steps. n_p is the number of time steps per mode two oscillation. The values for peak frequency and quality factor from infinite cylinder theory are shown in Table 13. All simulations have the same bounding box ($s_y = 10\delta_{s,1}$) and spatial resolution ($\Delta x = 0.375\delta_{s,1}$). 90

15 Peak frequency and quality factor for the first two modes of the cantilever as calculated from numerics for three different spatial resolutions, Δx. The values for peak frequency and quality factor from infinite cylinder theory are shown in Table 13. All simulations have identical time steps ($n_p = 20$) and bounding box size ($s_y = 10\delta_{s,1}$). 91

16 Peak frequency and quality for the first two modes of the cantilever as calculated from numerics for three different simulation domain sizes. The values for peak frequency and quality factor from infinite cylinder theory are shown in Table 13. All simulations have the same time step ($n_p = 30$) and spatial resolution ($\Delta x = 0.375\delta_{s,1}$). 93

17 Properties of the high aspect ratio cantilever and two different viscosity fluids used. The Stokes length for mode two $\delta_{s,2}$, the corresponding number of cells N_c, the quality factor Q_2, and the number of time steps for modes one and two, n_1 and n_2 respectively are shown. The total number of time steps is based on 20 points per mode two oscillation and three oscillations of the total ring-down, $t_{max,n} = 3\tau = 3(2\pi Q_n/\omega_{f,n})$. 95

List of Figures

1 A schematic showing the size of various physical systems. The plot ranges over 18 orders of magnitude. Most systems of interest for biology are at the top of this range. The dashed line indicates a larger span of scales. The E. coli image is from the NIH, and the microcantilever is from Olympus [56]. 3

2 A schematic of random fluctuations in displacement caused by the thermal motion of molecules. The deflection has been normalized. The mean squared deflection of current Atomic Force Microscopy cantilevers is on the order of a nanometer at room temperature, see Table. 7. 5

3 (left) An image of a commercially available cantilever used for atomic force microscopy [56]. A tip has been placed at the end of the cantilever in order to allow more resolved lateral measurement. (right) An image of a V-shaped cantilever taken from Ref. [3]. Microscopy cantilevers are typically composed of silicon or silicon nitride, and have thicknesses of $\sim 1\mu$m. 8

4 Images of the atomic structure of (a) graphite, (b) molybdenum disulfide, and (c,d) boron nitride obtained using an atomic force microscope. This image is from [3]. 9

5 Several spectral density peaks of the displacement of an oscillator $|\hat{u}(\omega)|^2$ are shown with quality of $Q = 1, 2, 3, 4, 5$. As the quality decreases, the peak broadens and shifts to lower frequency. R is the frequency based Reynolds number and can be thought of as a nondimensional frequency, see Eq. (16). 14

6 A schematic of a microscopic cantilever with length L and height h in proximity of a solid surface (not drawn to scale). The beam and wall are separated by a distance s and the time dependent tip displacement is given by $U(t)$. 17

7 (left) Analytical and numerical approach for calculating the noise spectrum. (right) Analytical and numerical approach for calculating the power spectrum. The approaches are for cantilever deflection, however the results for cantilever angle are derived in a similar manner. 22

8 (left) A schematic of the removal of a step source used in linear response theory. The source is normalized by Ψ_0 and t is time. The system response to this source is related to the autocorrelation. (right) The ringdown of the dynamical variable $A(t)$ and the autocorrelation of $a(t)$. 23

9 (left) The cantilever tip-deflection $U(t)$ is conjugate to a step point force at the tip F_0. (right) The cantilever tip-angle $\Theta(t)$ is conjugate to a step point torque at the tip τ_0. 24

10 The first four normalized mode shapes for a cantilever with uniform cross-section. 25

11 The vacuum resonance frequencies for the C2 rectangular cantilever as a function of mode number, $f_{0,n} = \omega_{0.n}/(2\pi)$. The dashed line is a curve fit, $f_{0,n}/(1000) = 205.3n^2 - 225.6n + 88.9$. (right) The dynamic spring constants for the C2 rectangular cantilever as a function of mode number. The dashed line is a power law curve fit, $k_n = 1.48n^{5.039}$. 27

12 Schematics of the two micron scale cantilever geometries considered (not drawn to scale). Panel (a), A rectangular cantilever with aspect ratios $L/h = 98.5$, $w/h = 14.5$, and $L/w = 6.8$. The cantilever is composed of silicon with density $\rho_c = 2329$ kg/m^3 and Youngs Modulus $E = 174$ GPa. Panel (b), A V-shaped cantilever with aspect ratios $L/h = 233$, $w/h = 30$, and $L/w = 7.8$. The total width between the two arms normalized by the width of a single arm is $b/w = 10.36$. The cantilever planform is an equilateral triangle with $\theta = \pi/3$. The cantilever is composed of silicon nitride with $\rho_c = 3100$kg/m^3 and $E = 172$GPa. The specific dimensions for the rectangular and V-shaped cantilever are given in Table 4. 31

13 Analytical predictions of the tip-deflection noise spectrum $G_u(\omega)$ using infinite cylinder approximations for three modes (solid) and modes 1 and 2 individually (dashed). 36

14 Analytical predictions of the tip-angle noise spectrum $G_\theta(\omega)$ using infinite cylinder approximations for three modes (solid) and modes 1 and 2 individually (dashed). 37

15 The cantilever can be driven by a sinusoidal force that is uniformly distributed along the length (left) or localized at the free end (right). 39

16 (left) The square of the angle of the mode shape at the tip as a function of mode number, n. This factor appears in the expression for tip-angle noise spectrum, and causes more energy to be distributed to higher modes. The dashed line is a quadratic fit, $\Phi_n'(x)^2 = 38.3n^2 - 33.4n + 3.2$. (right) The square of the integral of the mode shape as a function of mode number. This factor appears in the expression for power spectrum due to a uniform drive force, resulting in less energy in higher modes for this case than tip drive. The dashed line is an exponential fit, $\left(\int_0^1 \Phi_n dx\right)^2 = 1.46\exp(-0.983n)$. 41

17 Analytical predictions of the tip-deflection power spectrum for a uniformly distributed force (left) and a force localized at the tip (right). The applied forces vary sinusoidally in time. The spectra are calculated using infinite cylinder approximations for three modes (solid) and modes 1 and 2 individually (dashed). . 43

18 Analytical predictions of the tip-angle power spectrum for a uniformly distributed force (left) and a force localized at the tip (right). The applied forces vary sinusoidally in time. The spectra are calculated using infinite cylinder approximations for three modes (solid) and modes 1 and 2 individually (dashed). 44

19 The normalized transverse beam deflection U as a function of x for an applied force (solid) and applied torque (dashed) at the cantilever tip. 49

20 A log-linear plot of the magnitudes of the first five mode coefficients for a uniform cross-section beam. The squares are the coefficients for an applied tip-force, where the dashed line is a power law fit, $a_n = 0.827n^{-4.83}$. The circles are the coefficients for an applied tip-torque, where the dashed line is a power law fit, $a_n = 0.887n^{-3.56}$. 50

21 The normalized autocorrelation of the C2 rectangular cantilever for tip-deflection (solid) and tip-angle (dashed). (Inset) A detailed view of the autocorrelation at short time differences to illustrate the influence of higher modes in the tip-angle measurements. 56

22 The noise spectra of stochastic fluctuations in cantilever tip-angle (dashed) and tip-deflection (solid) from numerical simulations of the C2 rectangular cantilever. The curves are normalized to have the same area, however only the first two modes are shown. . . . 57

23 (left) The spectra of thermally driven fluctuations in cantilever tip deflection from numerical simulations (solid) and infinite cylinder theory (dashed) for the C2 rectangular cantilever. (right) The spectra of thermally driven fluctuations in cantilever tip angle from numerical simulations (solid) and infinite cylinder theory (dashed) for the C2 rectangular cantilever. 58

24 (left) The power spectra of an externally driven cantilever measured using tip-deflection from numerical simulations (solid) and analytical predictions of infinite cylinder theory (dashed) for the C2 cantilever. The cantilever is driven by a force uniformly distributed along the beam length that varies sinusoidally with time. (right) The power spectra of an externally driven cantilever measured using tip-angle from numerical simulations (solid) and analytical predictions ofinfinite cylinder theory (dashed) for the C2 cantilever. The cantilever is driven by a force uniformly distributed along the beam length that varies sinusoidally with time. 60

25 (left) The power spectra of an externally driven cantilever measuring tip-deflection from numerical simulations (solid) and analytical predictions of infinite cylinder theory (dashed) for the C2 cantilever. The cantilever is driven by a force localized at the tip that varies sinusoidally with time. (right) The power spectra of an externally driven cantilever measuring tip-angle from numerical simulations (solid) and analytical predictions of infinite cylinder theory (dashed) for the C2 cantilever. The cantilever is driven by a force localized at the tip that varies sinusoidally with time. 61

26 (left) The ratio for C2 of thermally to externally driven fluctuations in cantilever tip deflection from numerical simulations (solid) and infinite cylinder theory for three modes (dashed) and one mode (dash-dot). The noise and power spectrum for multiple modes are those in Eqs. (49) and (72). (right) The ratio for C2 of thermally to externally driven fluctuations in cantilever tip deflection from numerical simulations (solid) and infinite cylinder theory for three modes (dashed) and one mode (dash-dot). The noise and power spectrum for multiple modes are those in Eqs. (64) and (74). 62

27 The ratio for C2 of thermally to externally driven fluctuations in cantilever tip-deflection from numerical simulations (solid) and infinite cylinder theory for many modes (dashed) and one mode (dash-dot). The figure focuses on the low frequency behavior of the spectra ratio in Fig. 26. 63

28 A schematic of the V-shaped cantilever showing the cross-sections studied. Section $a - a$ is located at $z = 0$, $b - b$ is located at $x = 77\mu$m, and $c - c$ is located at $x = 108.8\mu$m. 65

29 The fluid flow near the tip of the cantilever as illustrated by the velocity vector field calculated from finite element numerical simulations. A cross section of the $x-y$ plane at $z=0$ is shown (see Fig. 12) that is a close-up view of the tip-region. The shaded region indicates the cantilever (because of the small deflections used in the simulations that cantilever does not appear to be deflected). (left) The flow field near the tip of the rectangular cantilever. This flow field is at t=6μs and the magnitude of the largest velocity vector shown is -0.3 nm/s. (right) The flow field near the tip of the V-shaped cantilever, cross-section $a-a$ in Fig. 28. This flow field is at t=7.2μs and the magnitude of the largest velocity vector shown is -26 nm/s. The shaded region indicates the tip region where the two single arms have merged. The open region to the left is where the two single arms have separated revealing the open region in the interior of the V-shaped cantilever. 66

30 The fluid velocity vector field at two axial positions along the Veeco V-shaped cantilever calculated from deterministic finite element numerical simulations. Cross sections of the $y-z$ plane are shown (see Fig. 12), the entire simulation domain is not shown and the shaded region indicates the cantilever. Both images are taken at t=7.2μs and the maximum velocity vector shown is -26 nm/s. (left) The $y-z$ plane at $x = 77\mu$m, cross-section $b-b$ in Fig. 28. The skewed width of a single arm of the cantilever in this cross-section is 18μm. The distance separating the two cantilever arms is 36μm. (right) The $y-z$ plane at $x = 108.8\mu$m. , cross-section $c-c$ in Fig. 28 This is the point at which the two single arms join to make a continuous cross-section of width $2w$. . . . 67

31 The normalized autocorrelation of equilibrium fluctuations in the tip-deflection $\langle u_1(0)u_1(t)\rangle$ (solid lined) and in tip-angle $\langle \theta_1(0)\theta_1(t)\rangle$ (dashed-line) for the Veeco V-shaped cantilever. The inset shows a close-up of the dynamics for short time differences to illustrate the influence of the higher modes in the tip-angle measurements. 68

32 The noise spectra for the Veeco V-shaped cantilever as determined from the tip-displacement G_u (solid line) and from tip-angle G_θ (dashed line). The curves are normalized to have an area of unity, with only the first two modes shown. 69

33 The noise spectrum of tip-deflection for the Veeco V-shaped cantilever as determined from numerical simulations and infinite cylinder approximations. It is evident that the approximate analytics can predict the peak location and width. However considerable variation is seen for the frequency dependence of the spectrum. 71

34 (left) A schematic of the iDrive actuation approach applied to a V-shaped microscopy cantilever. (right) A comparison of the experimentally measured thermally and externally driven spectra. The schematic and comparison come from the iDrive information sheet, Asylum Research [6]. 74

35 The spectra of thermally driven fluctuations in cantilever tip-angle from experiment (solid) and numerical simulations (dashed) for the Olympus V-shaped cantilever. Experimental measurements are from Asylum Research, to be published [27]. 75

36 (left) The power spectrum for the Olympus V-shaped cantilever tip-angle driven by the iDrive activation technique from experiment (solid) and numerical simulations (dashed). (right) The power spectrum in the vicinity of the first resonance peak for experiment (solid), numerical simulations of the iDrive impulse response (dashed), and simulations where the cantilever is driven by a sinusoidal iDrive force (squares). Experimental measurements are from Asylum Research, to be published [27]. 76

37 The ratio of fluctuations in Olympus V-shaped cantilever tip-angle for thermal and external driving forces. Results are shown for experiment using the iDrive power spectrum [27] (solid), numerics using the iDrive power spectrum (dashed), and numerics for a uniformly distributed force power spectrum. For the iDrive technique the ratio is nearly constant for moderate frequency, in contrast to the trend predicted by infinite cylinder theory. The uniform force and iDrive cases deviate significantly. 77

38 A schematic of the fluid flow regions around a cantilever in the vicinity of a solid surface (not drawn to scale). As the boundary moves into the Stokes layer the viscous flow must adjust. 80

39 Panel (left) The noise spectra G_u of stochastic fluctuations in cantilever tip-deflection for separations $s = 10, 12, 15, 20, 40\mu$m. Panel (right) the noise spectra G_θ of stochastic fluctuations in cantilever tip-angle for separations $s = 15, 25, 60\mu$m. The spectra have been normalized by the maximum value of G_u or G_θ. The smallest and largest values of separation are labeled with all other values appearing sequentially. 82

40 The variation of the peak frequency (panel (a)) and quality (panel (b)) of the fundamental mode of the V-shaped cantilever in fluid as a function of separation from a nearby wall. Results calculated using tip-deflection are circles, results using tip-angle are squares, and theoretical predictions using the results of Ref. [43] are triangles. The peak frequency and quality factor of the fundamental mode in an unbounded fluid are $\omega/\omega_f \approx 0.19$ and $Q \approx 2$ and are represented by the horizontal dashed line. The distance s is normalized by the Stokes length $\delta_s = 4.14\mu$m. 84

41 The quality factor Q as a function of Reynolds number R for a single mode. Also plotted are the real and imaginary parts of the hydrodynamic function for an infinite cylinder, Γ_r and Γ_i respectively. 86

42 The quality factor for the first 5 modes of the C2 cantilever using eigenfrequencies $\omega_{f,n}$ in fluid from infinite cylinder theory. The dashed line is a linear fit, $Q_n = 5.829n - 1.828$. 87

43 The Stokes lengths for the first 5 modes of the C2 cantilever using eigenfrequencies in fluid $\omega_{f,n}$ from infinite cylinder theory. The dashed line is a power law fit, $\delta_{s,n} = 2.32 \times 10^{-6}\ n^{-1.328}$. 88

44 Schematics of the numerical domain including the cantilever and fluid in the a) $x - y$ and b) $y - z$ planes. The bounding box is a no-slip wall. 90

45 (left) The fluid mass loading for the C2 cantilever calculated from the tip-deflection numerics (solid) and infinite cylinder theory (dashed). (right) The mass loading for the C2 cantilever with half the width, $w' = w/2$, calculated from the tip-deflection numerics (solid) and infinite cylinder theory (dashed). 102

46 (left) The viscous damping for the C2 cantilever calculated from the tip-deflection numerics (solid) and infinite cylinder theory (dashed). (right) The viscous damping for the C2 cantilever with half the width, $w' = w/2$, calculated from the tip-deflection numerics (solid) and infinite cylinder theory (dashed). 103

47 The three-dimensional (left) mass loading and (right) viscous damping for the V-shaped Veeco cantilever near a solid surface. The damping is shown for numerical simulations measuring cantilever tip-deflection. 104

Nomenclature

$\hat{}$	Denotes a parameter in the frequency domain
$\langle\rangle$	Ensemble average
$a(t)$	Stochastic fluctuations in a dynamical variable
$A(t)$	Deterministic response to the removal of a step source
a_n	Coefficients for the modal deflection of a cantilever
α_n	Mass prefactor for mode n to get the correct kinetic energy
β	Phase shift (rad)
$B_n(\omega)$	Function that accounts for the fluid force on an infinite cylinder.
c_n	Coefficient of the n^{th} cantilever mode
$\delta_{s,n}$	Stokes length for mode n, (m)
E	Young's modulus, (N/m^2)
E_t	Total beam energy, (J)
f_0	Resonant frequency in vacuum, (Hz)
f_s	Oscillation frequency, (Hz)
$f(t)$	Step force applied to an elastic system, (N)
$\hat{f}_n(\omega)$	Frequency dependence of cantilever deflection for mode n
F_0	Magnitude of a step force, (N)
F_D	External driving force applied to a beam, (N)
F'_B	Brownian force due to thermal motion, (N)
F_f	Force due to hydrodynamic effects, (N)
$G_F(\omega)$	Power spectral density of the Brownian force, (N^2/s)
$G_u(\omega)$	Noise spectrum of the autocorrelated stochastic oscillations in deflection, (m^2/s)
$G_\theta(\omega)$	Noise spectrum of the autocorrelated stochastic oscillations in angle, (rad^2/s)
$\gamma_f(\omega)$	Fourier transform of the fluid damping, (kg)
$\Gamma(\omega)$	Hydrodynamic function
h	Cantilever thickness, (m)
h'	Equivalent thickness of a rectangular cantilever, (m)

$\hbar$	Planck's constant (1.055×10^{-34} J-s)
I	Moment of inertia, (m^4)
k	Bending spring stiffness constant, (N/m)
k_t	Torsional spring stiffness constant, (N m)
k_B	Boltzmann's constant (1.38×10^{-23} J/K)
L	Cantilever length, (m)
L'	Equivalent length of a rectangular cantilever, (m)
m_c	Actual system mass, (kg)
m_e	Effective mass, (kg)
$m_f(\omega)$	Fourier transform of the added mass of fluid, (kg s)
M_i	Constants, $i = 1, 2, 3, ...$
μ	Mass per unit length, (kg/m)
μ_f	Dynamic viscosity of a fluid, (kg/(m-s))
n_p	Number of points per system oscillation
N_c	Number of cells in a simulation
ν_f	Fluid kinematic viscosity μ/ρ_l, (m^2/s)
ω	Frequency, (rad/s)
ω_0	Resonant frequency in vacuum for mode one, (rad/s)
$\omega_{0,n}$	Resonant frequency in vacuum for mode n, (rad/s)
$\omega_{f,n}$	Resonant frequency in fluid for mode n, (rad/s)
$\tilde{\omega}_n$	Frequency normalized by the resonant frequency in vacuum for mode n, (rad/s)
$\Phi_n(x)$	Cantilever mode shape for mode n.
Q	Quality number
R	Reynolds number
ρ_c	Solid density, (kg/m^3)
ρ	Fluid density, (kg/m^3)
s_x	Separation in x-direction between the cantilever and wall, (m)
s_y	Separation in y-direction between the cantilever and wall, (m)
s_z	Separation in z-direction between the cantilever and wall, (m)
$\psi(t)$	Step source applied to an elastic system
Ψ_0	Magnitude of the step source
t	Time, (s)
Δt	Time difference, (s)

T	Absolute temperature, (K)
$\tau(t)$	Step torque applied to an elastic system, (N m)
τ_0	Magnitude of a step torque, (N m)
$\theta(t)$	Stochastic fluctuations in cantilever tip-angle, (rad)
$\Theta(t)$	Deterministic cantilever tip-angle response to the removal of a step torque, (rad)
$\langle\theta^2\rangle$	Mean-squared angle, (rad^2)
$u(t)$	Stochastic fluctuations in cantilever tip-deflection (m)
$U(t)$	Deterministic cantilever tip-deflection response to the removal of a step force (m)
w	Cantilever width, (m)
w'	Equivalent width of a rectangular cantilever, (m)
$\langle u^2\rangle$	Mean-squared displacement in the x-direction, (m^2)
X_0	Initial displacement, (m)
Y_0	Amplitude of the Lorentzian fit, arbitrary units

1 Introduction

1.1 Research Motivation

Experimental techniques using micro and nanoscale systems are popular for studying chemical and biological systems. Approaches using microscopic systems are capable of sensing intermolecular forces in real time. In particular, microscopic cantilevers are a promising device to probe biological systems in their ambient environments. However, experiments that involve micro and nanoscale cantilevers are time intensive, difficult to construct, and expensive. Also, the motion of cantilevers in a viscous fluid is complex. Theoretical studies of such systems are valuable to characterize the underlying physical phenomena prior to construction. The understanding gained from theoretical studies describes the dynamics that experiments will encounter, and can guide the creation of novel experiments.

This thesis presents analytical and numerical studies of the dynamics of microscale cantilevers in fluid for several experimentally relevant conditions. The results presented are equally valid for nanoscale cantilevers, and the approach can be applied to a variety of small scale elastic structures. The current chapter provides a brief background of scientific research that has led to the current technology. Chapter 2 describes the approximate analytical model and the numerical approach used to describe the thermally and externally driven motion of cantilevers. Chapter 3 investigates the measured dynamics of microscopic cantilevers for two measurement approaches. The results indicate differences that are encountered in experiments due to the chosen measurement approach. Chapters 4 and 5 quantify the stochastic and driven dynamics of microscopic rectangular and V-shaped cantilevers in viscous fluid. The results in these chapters are precisely for the conditions measured in experiments. In Chapter 6, the case of a microscopic cantilever in fluid near a solid surface is considered. This

is a common configuration in experiments. The results quantify the increased added mass and viscous damping caused by a solid boundary. Chapter 7 investigates higher cantilever modes as a method for overcoming strong damping. The analytical study presented indicates the vast potential of higher modes. The numerical study describes the resolution and domain size necessary to quantify the precise dynamics of higher modes in fluid. Finally, Chapter 8 presents a numerical approach to calculate the fluid added mass and viscous damping for flow around a three-dimensional cantilever.

1.2 Brief History of Science

Prior to analyzing the dynamics of micro and nanoscale cantilevers, it is useful to understand the history of scientific research that led to the creation of such devices. For centuries, the desire to understand unexplained phenomena in everyday life has led people to study small scale objects. In particular, there has always been a strong desire to understand the numerous vital biological processes that are constantly occurring in living organisms. The advent of the optical microscope in the early 1600's allowed scientists the first opportunity to investigate the realm of individual biological cells. The subsequent discovery of cells as the building blocks of life yielded great insight into the structure of living things [48]. However, sharper resolution is necessary to understand how cell processes proceed. While an optical microscope allows people to see bacteria in their natural environment, the underlying processes of locomotion and reproduction remained a mystery.

Further insight into microscopic phenomena was gained from Max Planck's discovery that the energy released by an oscillating particle can only take discrete values [61]. This quantum theory and the discovery of the atomic nucleus

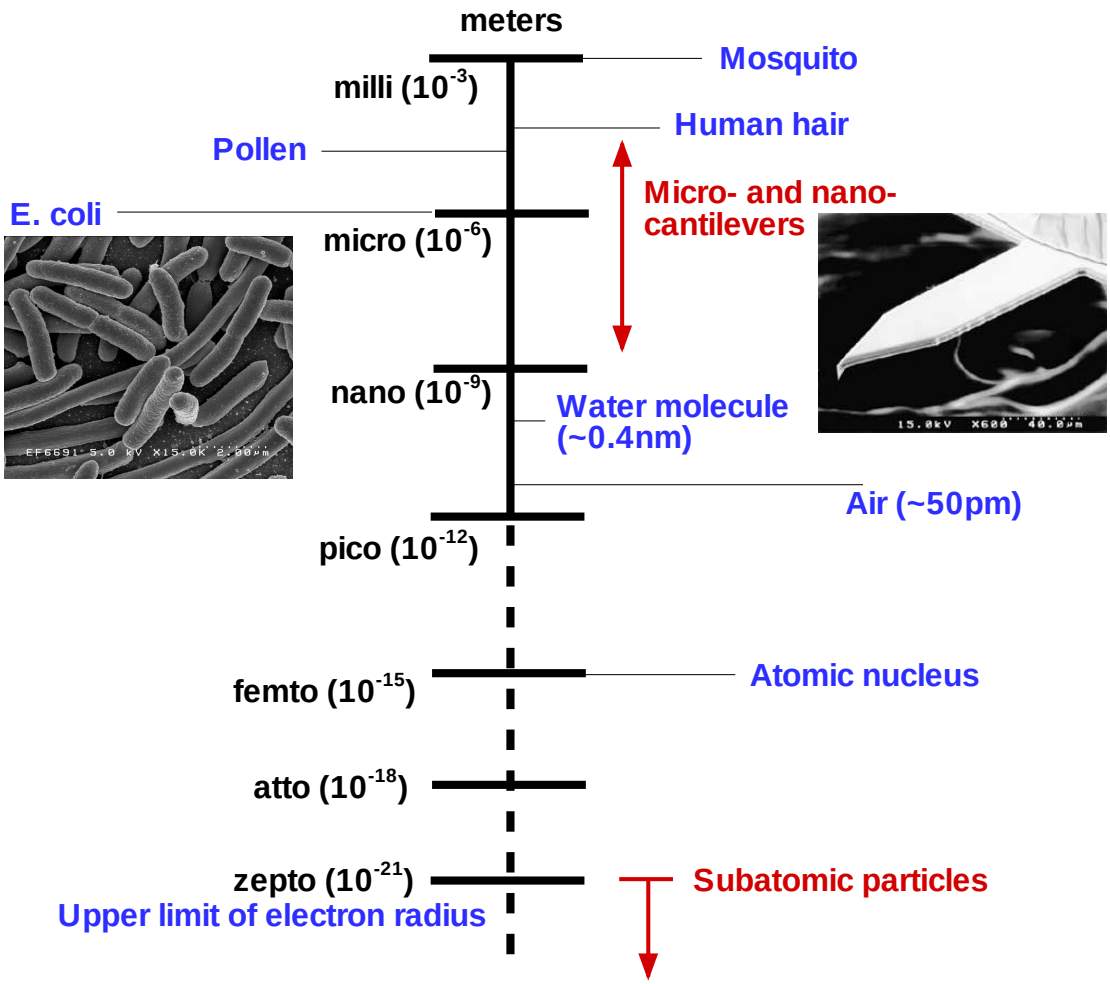

Figure 1: A schematic showing the size of various physical systems. The plot ranges over 18 orders of magnitude. Most systems of interest for biology are at the top of this range. The dashed line indicates a larger span of scales. The E. coli image is from the NIH, and the microcantilever is from Olympus [56].

by Ernest Rutherford yielded a firmer understanding of the interaction of individual subatomic particles [67]. Using the principles of quantum theory, Niels Bohr was able to describe the subatomic structure [12]. These discoveries, along with quantum mechanical advances by Werner Heisenberg [47], gave scientists an understanding of the properties of elements and explained the process of chemical reactions. All of these findings helped early scientists to understand properties of matter at the sub-Angstrom scale. To put small length scales in perspective, Fig. 1 gives some relevant objects and their sizes.

While quantum physics is always present it must only be accounted for under certain circumstances. In many microscopic studies quantum effects are negligible. In order for quantum effects to be important the system's oscillation energy must be on the order of its thermal energy. However, many times the quantum effects are small compared to thermal noise,

$$\frac{\hbar\omega}{k_B T} \ll 1. \tag{1}$$

Here $\hbar = 1.055 \times 10^{-34}$J-s is Planck's constant, ω is the frequency of oscillation, $k_B = 1.38 \times 10^{-23}$ J/K is Boltzmann's constant, and T is the absolute temperature. This expression indicates that at ambient temperatures the frequency must be on the order of $\omega \approx 1 \times 10^{13}$rad/s for quantum effects to be significant. For cryogenic conditions, $T \sim 10$ mK, quantum effects must be accounted for beyond $\omega \approx 1 \times 10^{9}$rad/s. Except in experiments designed to reach the quantum limit [72], these conditions are not common in microscopic systems. This is especially true when investigating biological systems, where temperatures are necessarily moderate, ($T \approx 300$K), and frequencies are typically on the order of Hertz ($\omega \approx 2\pi$rad/s).

Above the quantum limit the thermal energy of atoms must still be investigated. Thermal energy produces random motion in all objects. The thermally

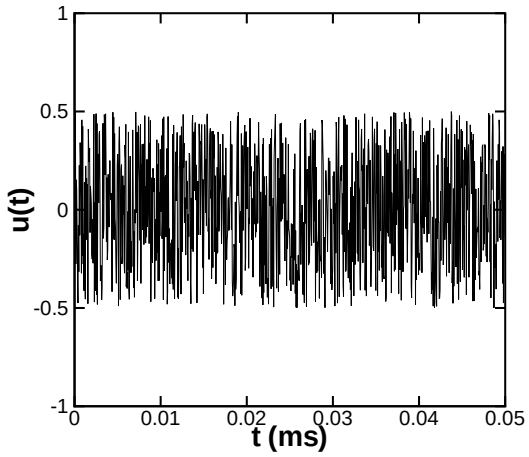

Figure 2: A schematic of random fluctuations in displacement caused by the thermal motion of molecules. The deflection has been normalized. The mean squared deflection of current Atomic Force Microscopy cantilevers is on the order of a nanometer at room temperature, see Table. 7.

driven motion, known as Brownian motion, was first observed and recorded in the random motion of pollen molecules in air at room temperature, using an optical microscope [14]. The pollen molecules exhibited random fluctuations in position due to the continual bombardment by the thermal motion of the surrounding air molecules. All objects at a finite temperature experience random fluctuations in space. For a microscopic cantilever the random fluctuations are accessible in measurements. An example of this random motion is shown in Fig. 2. However, the magnitude of these fluctuations makes them negligible in the macroscopic regime.

An important discovery was the relationship between the fluctuations at thermal equilibrium from atomic motion and the resulting friction [35]. This is now known as the fluctuation-dissipation theorem [57]. The fluctuation-dissipation theorem is based on the fact that the spontaneous fluctuations of an

object in thermal equilibrium are governed by the same physics as the dissipation on that object as it relaxes to equilibrium. A thermodynamic approach can be developed to describe fluctuating objects based on the fluctuation-dissipation theorem [18, 19]. This approach quantifies the energy transfer from the system to its surroundings through dissipative effects, and relates this to the energy absorption in equilibrium that leads to spontaneous fluctuations. An example of spontaneous equilibrium fluctuations are those caused by Brownian motion.

The thermal motion of a mechanical system can be used to calibrate the stiffness of a system. This is achieved by measuring the mean squared displacement and using the equipartition of energy theorem,

$$\frac{1}{2}k\left\langle u^2\right\rangle = \frac{1}{2}k_B T. \tag{2}$$

Here k is the bulk spring constant of the system, $\langle u^2 \rangle$ is the mean squared system displacement, and the $\langle\rangle$ denote an equilibrium ensemble average. The equipartition of energy theorem states that each quadratic mode of energy in a system (*e.g.* potential energy, kinetic energy, *etc.*) receives an equal amount of energy from the thermal bath proportional to the temperature [21]. Equation (2) indicates that knowing the temperature and measuring the mean squared displacement is sufficient to calculate the stiffness,

$$k = \frac{k_B T}{\langle u^2 \rangle}. \tag{3}$$

Limited detection resolution introduces error on the order of 5% into such calculations [16, 32].

The physical understanding gained from microscopic studies, quantum mechanics, and the fluctuation-dissipation theorem gives insight into the dynamics of micron and nanoscale systems. These principles govern subatomic particles and the motion of individual atoms. However, the motion of molecules is more

complex and is difficult to describe. In order to probe individual molecules, researchers have applied advances from particle physics to create experimental techniques for investigating systems with length scales of tens of nanometers.

The conventional refractive microscopes of Galileo and Hooke were able to view individual biological cells. However, they lacked the resolution to study length scales of microns. The limitation of optical methods means a different approach is necessary in order to investigate macromolecules and surface properties at the atomic scale. To achieve imaging at this scale, researchers used principles from particle physics. By bombarding a sample with electrons, the reflected electrons can be registered in order to obtain an image [54, 81]. This approach to sample imaging is now known as scanning electron microscopy. The scanning electron microscope allows scientists to visualize objects at the nanometer scale, though its use is limited to the study of electrical conductors. This tool achieved the observational requirements of researchers. It remained to improve techniques for manipulating and investigating systems with sizes on the order of molecules.

A major stumbling block to investigating molecular processes is the size of the experimental instruments. The need for improved force and time resolutions required novel and sensitive equipment. This demand was met by creating mechanical structures on the order of the molecules and cells of interest, see Fig. 1. These micro and nano electromechanical systems (MEMS and NEMS) include microfluidic devices, and micron and nanoscale elastic structures. These devices allow small scale objects to be directly manipulated and investigated. Richard Feynman [39] presented a famous description of the wide possibilities opened by the introduction of MEMS and NEMS and challenged the scientific community to push the limits of submicron scale technology. The progress made in techniques using particle physics and micro and nanoscale fabrication

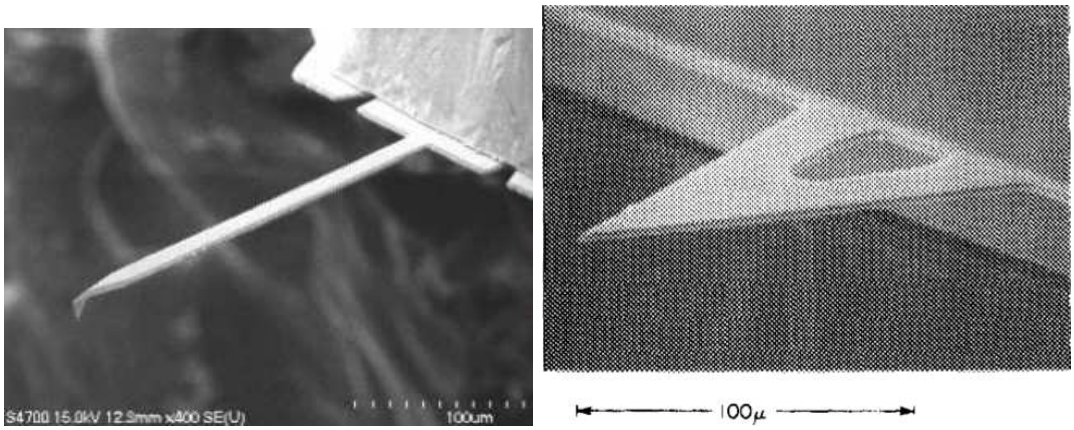

Figure 3: (left) An image of a commercially available cantilever used for atomic force microscopy [56]. A tip has been placed at the end of the cantilever in order to allow more resolved lateral measurement. (right) An image of a V-shaped cantilever taken from Ref. [3]. Microscopy cantilevers are typically composed of silicon or silicon nitride, and have thicknesses of $\sim 1\mu$m.

has led to the use of microscopic cantilevers. These cantilevers show promise of achieving the goal of probing the dynamics of individual molecules [23, 63, 64].

1.3 Experimental Techniques: Microscopy Cantilevers

The decades following Richard Feynman's well known talk, "There's plenty of room at the bottom" [39], brought vast improvements in experimental techniques. One novel technique with particular promise was the use of microscopic cantilevers to probe surfaces at atomic resolution and measure molecular forces. Some examples of such cantilevers for this purpose are shown in Fig. 3. The forces exerted on the cantilever by the sample cause the cantilever to oscillate. Measurements of the cantilever dynamics correlate to the applied forces. A scanning tunneling microscope was the initial approach for measuring the dynamics of a microscopic cantilever. The scanning tunneling microscope measures the quantum tunneling resistance between the tip and the cantilevered

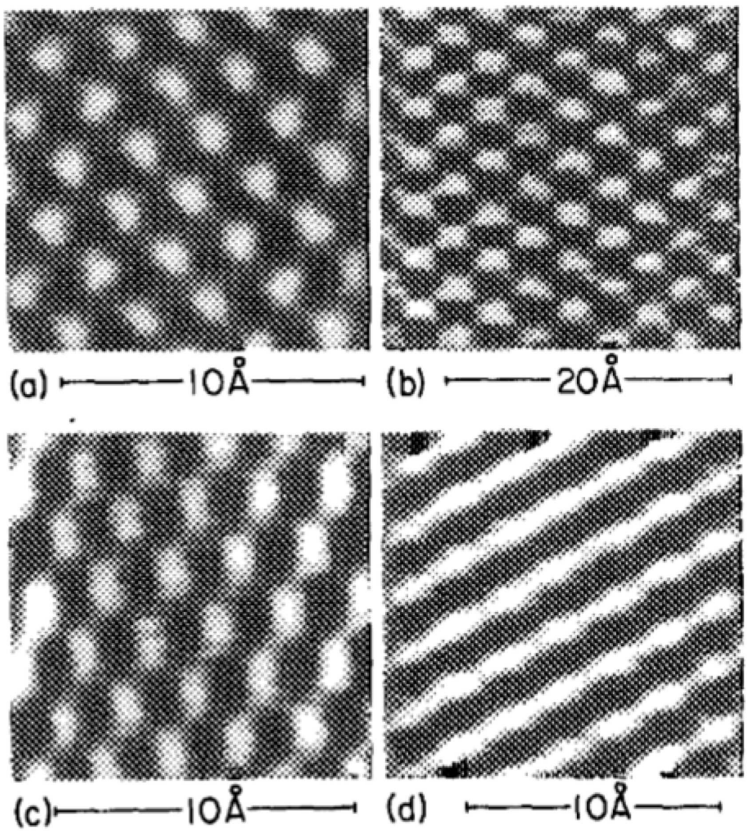

Figure 4: Images of the atomic structure of (a) graphite, (b) molybdenum disulfide, and (c,d) boron nitride obtained using an atomic force microscope. This image is from [3].

probe, which can be used to calculate displacement [11]. By using a scanning tunneling microscope to probe the displacements of a cantilever the surface of an insulator can be studied with Angstrom resolution [3]. The approach of using a microscopic cantilever to measure surface properties was termed atomic force microscopy, AFM [11]. The cantilevers have small mass and deflect to measurable displacements in response to inter-atomic forces, see Table 1. Atomic force microscopy is capable of measuring topography with atomic resolution for conductors and insulators without damaging the sample [3], see Fig. 4.

Early research using AFM produced images with atomic resolution of a non-conducting material [3]. In the study by Albrecht *et al.* [3] a triangular planform or V-shaped cantilever was used to decrease noise due to lateral bending modes, see Fig. 3 (right). However, more recent research has indicated that these probes exhibit lateral bending comparable to rectangular cantilevers [68]. The V-shaped cantilever also had the advantage of making it simpler to obtain single molecule contact between the probe and sample. Multiple contact points can cause the image to blur, see Fig. 4(d). Advances in MEMS and NEMS technology have circumvented this issue in rectangular cantilevers by using nanometer pyramidal tips and carbon nanotubes, see Fig. 3 (left).

The study by Albrecht *et al.* [3] took advantage of the thermal motion of atoms in the cantilever. When the cantilever approaches a sample, the attractive forces of the surface atoms cause the magnitude of oscillations to decrease. The average deflection of the cantilever tip as the sample is moved under it then relates directly to the topography of the sample surface. While other methods of drive have been applied, including piezoshaker and magnetomotive forcing [42], the thermal drive approach takes advantage of the inherent beam motion.

Further research applied atomic force microscopy in novel ways, such as analyzing surface properties and topography simultaneously [50]. Advances in detection techniques improved the scale of measurements through the advent of non-invasive detection approaches such as optical interferometry [37, 71]. Unlike the scanning tunneling microscope which calculated the displacement of the cantilever tip from the tunneling current, optical techniques measure the angle of the beam at its tip. This is accomplished by reflecting a laser off of the tip and reading the change in location on a photoreceptor. As the use of microscopic cantilevers broadened, challenges have been encountered that must be overcome.

1.4 Open Challenges for Microscopic Cantilevers

The fluctuation-dissipation theorem can be used to predict the stochastic dynamics of micro and nanoscale cantilevers for any conjugate pair of dynamical variables [60]. Past application of the thermodynamic approach has centered on measurements of fluctuations in deflection of the cantilever tip. This is a result of the experimental use of the scanning tunneling microscope for tip-deflection measurements. However, experimentalists commonly measure other parameters instead. These include strain, resistance, and the angle of the cantilever tip. Analytical expressions have been derived for the stochastic deflection and angle of the cantilever tip [69]. However, a comparison of how thermal energy is distributed among the modes of a cantilever for fluctuating tip-deflection and tip-angle has not been presented. It is useful to understand the fundamental differences observed by measuring different quantities so as to separate these effects from those of the system of interest. By studying the equation of motion for a cantilevered beam it is possible to quantify the dynamics of various measurable dynamical variables. This approach allows for a comparison of inherent physical differences in measurement techniques.

The success of atomic force microscopy [40] led scientific researchers to begin constructing more complex small scale structures [66, 78]. Advances in construction techniques, such as electron beam lithography, allowed structures to be more adaptable [55]. This method uses a photoresist layer to selectively etch material using an electron beam, allowing for the creation of structures with nearly atomic accuracy. Scientists coupled electronic systems to the mechanical structures to aid in actuation and detection. This class of electromechanically coupled systems is now encompassed by the field of MEMS [55]. The push for devices with higher sensitivity and better force resolution brought about the creation of devices with lengths on the order of nanometers, and the field of

	$\tau(\mu s)$	X_{MIN} (m)	F_{SENS} (N)
Microcantilever (AFM)	$1 \sim 100$	10^{-10}	$10^{-11} \sim 10^{-7}$
Nanocantilever	$0.1 \sim 0.001$	10^{-9}	$10^{-9} \sim 10^{-7}$
Optical Tweezers	$1 \sim 100$	10^{-9}	$10^{-13} \sim 10^{-10}$

Table 1: The time scale τ, displacement resolution X_{MIN}, and force sensitivity F_{SENS} for three small scale measurement devices. Values taken from [15, 36].

NEMS [66, 33]. Nanoscale structures made of silicon have fundamental frequencies in vacuum in the Gigahertz range, making them useful for real time investigation of biological processes [36]. By tailoring the geometry of micron and nanoscale structures it is possible to adapt them to analyze the systems of interest [82].

One approach to describe the equilibrium fluctuations of a microscopic cantilever involves calculating the response of the fluid-structure system to a stochastic thermal force and calculating statistics from repeated simulations. This approach would involve simulating the random motion of every atom in the cantilever and surrounding fluid. A time step of a few picoseconds is necessary in order to capture atomic collisions. In addition, the simulations must be repeated many times for various initial conditions, or allowed to run for extended periods in order to probe all possible phase space configurations. Such an approach is computationally inaccessible using even the most powerful supercomputers available [24]. This method of simulating the stochastic motion of every atom would generate identical results to those given by the fluctuation-dissipation method [57].

1.4.1 Microscale Cantilevers in a Viscous Fluid

The wide use of microscopic cantilevers, such as in atomic force microscopy to analyze surface properties and topography in vacuum and air, led researchers

to extend its use for other purposes. The short time scale and high force sensitivity of the small scale cantilevers [4] were favorable for investigating the dynamics of biological molecules [13, 34, 63, 64], see Table 1. Table 1 also shows capabilities of nanocantilevers and optical tweezers.

It is important to discuss whether the continuum hypothesis remains valid for these systems. The continuum hypothesis is valid when the Knudsen number is small,

$$\mathrm{Kn} = \frac{\lambda}{L} \ll 1. \tag{4}$$

For micro and nanoscale cantilevers in liquid the Knudsen number is $\mathrm{Kn} \approx 10^{-4}$ [24]. Optical tweezer measurements have excellent potential, however they are typically too soft, calibration can be difficult, and there is the possibility of damaging the sample.

The use of cantilevers for the investigation of biological systems presents some issues. Analysis of biological entities in their ambient liquid environments is impeded by the large dissipation on the cantilever due to strong viscous damping [45]. Strong viscous damping and large volume of fluid entrained by a cantilever, or added mass, can make measurement difficult. In particular, the fundamental resonance peak shifts to lower frequency and broadens. It is more difficult to capture the dynamics of the system of interest in this case [7]. Figure 5 shows a series of resonance peaks over a range of quality factor from 1 to 5. Peaks with higher quality factor are sharper and will be easier to distinguish from noise to due to measurement uncertainties. In order to develop a measurement technique capable of using a microscopic cantilever to analyze the dynamics of molecules in liquid, this large fluid damping must be overcome. This requires an understanding of the fluid-structure dynamics. However, the effects of a viscous fluid on an oscillating cantilever are not well described. A

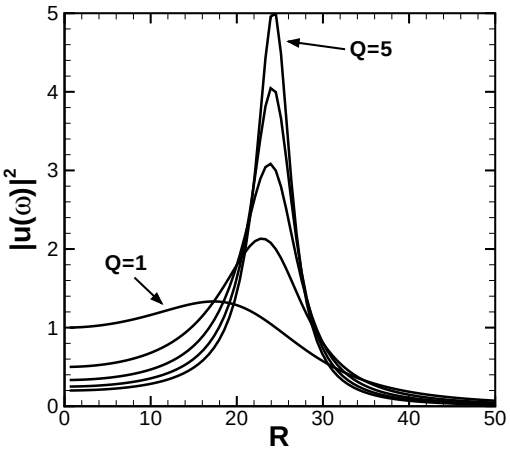

Figure 5: Several spectral density peaks of the displacement of an oscillator $|\hat{u}(\omega)|^2$ are shown with quality of $Q = 1, 2, 3, 4, 5$. As the quality decreases, the peak broadens and shifts to lower frequency. R is the frequency based Reynolds number and can be thought of as a nondimensional frequency, see Eq. (16).

description of the fluid dynamics on a small scale cantilever oscillating in viscous fluid is necessary in order to overcome the low quality oscillations.

There is no general analytical solution to the oscillations of a cantilever in viscous fluid. However, the force on an infinite cylinder oscillating in a viscous fluid is well known [65, 73]. For long and slender cantilevers in fluid with uniform cross-section, the dynamics of the fundamental mode can be modeled by assuming the flow at any point is equivalent to that around an infinite oscillating cylinder [69]. This approximation is valid for the fluid flow around microscale cantilevers. The original expression for the spectral density of thermal cantilever motion neglected the frequency dependence of the viscous damping [69], which has since been corrected [60]. The model of an infinite cylinder can be used with the thermodynamic approach based on the fluctuation-dissipation theorem to obtain the approximate stochastic dynamics of small scale cantilevers in fluid.

Infinite cylinder theory can also be applied to estimate the driven dynamics of a microscopic cantilever in fluid. The infinite cylinder model has also been extended to include the dynamics of higher cantilever modes in fluid [75], the coupled motion of multiple cantilevers in fluid [20], and the effects of a solid surface in the vicinity of the cantilever [28, 43].

In contrast to two-dimensional models, numerical simulations can be used to describe the complete fluid flow around an oscillating micro or nanoscale cantilever. This approach has the advantage of calculating the full three-dimensional flow characteristics. In addition, numerical simulations can be used to calculate dynamics for any experimentally relevant configuration. This includes any cantilever geometry, actuation approach, measured dynamical variable, and for multiple cantilevers in proximity coupled by a fluid [25]. Numerical simulations of the cantilever and the thermodynamic approach have yielded the noise spectrum for small scale cantilevers in fluid [59, 60] and the associated quality factor and mass loading for driven beams [9].

1.4.2 Externally Driven Dynamics of Microscale Cantilevers

Recent experiments have focused on novel techniques for driving the motion of microscopic cantilevers. Many approaches are in use today; piezo-shaker, an applied magnetic field [83], and thermal-elastic actuation [7]. As the device used in each case is similar, some parallel must exist between the stochastic dynamics of a cantilever and the motion resulting from an external driving force. For simple driving approaches, this investigation is straightforward using the two-dimensional model based on infinite cylinder approximations. In more complicated situations numerical simulations can be used to calculate the driven dynamics. The power spectrum for the precise cantilever geometry and actuation can be obtained from numerical simulations of the cantilever response

to an impulse force [69].

While the model based on infinite cylinder approximations can be useful to predict the motion of a microscale cantilever through a viscous fluid, it does not describe the motion when three-dimensional effects are significant. Even the earliest experiments with atomic force microscopes used triangular planform, or V-shaped, cantilevers, see Fig. 3 (right). When these cantilevers are operated in viscous fluid the flow is three-dimensional and a more detailed analysis is necessary. Approximations for the static properties of such cantilevers can be obtained from parallel beam theory [2, 17, 68, 70]. However, the stochastic dynamics of microscopic V-shaped cantilevers have not been well described. Using a numerical approach this is possible. The flow fields from deterministic numerical simulations give insight into the stochastic dynamics of the cantilever in fluid for the exact geometry used in experiment [23].

An interesting example is the iDrive system, which uses an oscillating current in a magnetic field to drive a V-shaped cantilever [6]. Experiments exhibit a frequency independent ratio of the thermal spectrum to the iDrive power spectrum. This is contrary to the predictions from infinite cylinder theory for the fundamental mode. The variation between the spectra ratio from experiment and infinite cylinder theory can be attributed to three-dimensional flow effects and higher mode dynamics. In order to understand the dynamics of this complex cantilever geometry and actuation, a full description of the three-dimensional motion is necessary. Using a numerical approach it is possible to separate the contributions from complex flow and the interactions between modes.

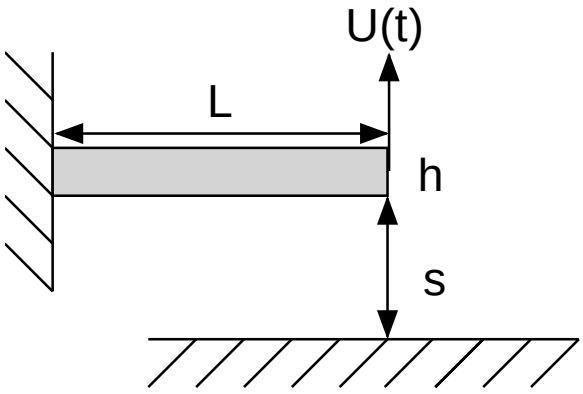

Figure 6: A schematic of a microscopic cantilever with length L and height h in proximity of a solid surface (not drawn to scale). The beam and wall are separated by a distance s and the time dependent tip displacement is given by $U(t)$.

1.4.3 The Fluctuations of a Microscale Cantilever in Fluid and Near a Solid Boundary

Descriptions of the three-dimensional motion of an oscillating microscopic cantilever far from boundaries do not completely describe the situations experienced in experiment. For example, measurements of surface topography and the dynamics of molecules require a beam in fluid to oscillate in the vicinity of a solid boundary [10]. Objects moving in fluid are affected by surrounding structures. This includes the coupled motion of spheres [51], infinite cylinders [20], microscale cantilevers [8, 25], and a resonating plate near a solid surface [46]. Analytical expressions for the motion of a cantilever as an infinite cylinder near a solid boundary give expressions for the added mass and viscous damping [28, 30, 43, 44]. Using numerical simulations and the fluctuation-dissipation theorem the complete solution can be quantified and compared directly with

experiment. A schematic of a cantilever near a wall is shown in Fig. 6. It is straightforward to extend such a study to the case of a cantilever inclined to a surface.

1.4.4 Fluid Dynamics Induced by Fluctuations in Higher Flexural Modes

Typical experiments using microscopic cantilevers analyze variations in fluctuations of the fundamental mode. In some cases the fundamental mode is not well suited for the measurement of interest, such as in viscous environments or near a surface where large fluid damping annihilates the first mode. One solution to circumvent this issue is to use the higher modes [13, 29, 41]. A cantilever oscillates at an infinite number of frequencies corresponding to orthonormal deflections of the cantilever. Each of these modes has a mode shape and corresponding eigenfrequency.

Approximate analytical expressions reveal that higher order modes have the advantage of better quality factor and higher resonant frequencies. However, a complete three-dimensional analysis is necessary to understand the complex fluid and structure dynamics. Approximate analytical solutions provide functions for the lumped two-dimensional fluid parameters. However, three-dimensional flows are neglected. Past applications of the fluctuation-dissipation theorem have derived the correlation functions and noise spectrum for the systems of interest [31]. The quality factor and peak frequency quantify the fluid parameters in the vicinity of the resonant peaks. It is useful to calculate the frequency dependent added mass and viscous damping on an oscillating cantilever. These results give a better understanding of fluid dynamics generated by a micro or nanoscale cantilever to aid further research into novel devices. As the spectral density of the Brownian force is directly related to the viscous

damping, an analysis of the fluid parameters also describes the Brownian force. This can be accomplished using numerical results for the full fluid-structure interaction and solving for the fluid parameters.

1.5 Fluctuation-Dissipation Theorem

The fluctuation-dissipation theorem describes the link between the Brownian force on an object due to the thermal motion of atoms and the damping that object experiences. In general this can be expressed as,

$$G_F(\omega) = 4k_B T \gamma_f(\omega), \tag{5}$$

$$G_F(\omega) = \left|\hat{F}_B(\omega)\right|^2. \tag{6}$$

In the above expression G_F is the spectral density of the Brownian force, k_B is Boltzmann's constant, T is the absolute temperature, and γ_f is the damping. For the case of micro and nanoscale cantilevers in fluid γ_f is the Fourier transform of the fluid viscous damping. Additional damping due to structural dissipation or clamping losses can also be accounted for if necessary. However, these effects are negligible in comparison to effects of the fluid. Equation (5) provides a relationship between a stochastic quantity G_F and a deterministic quantity γ_f. From this relationship it is evident that unless the viscous damping is independent of frequency, the Brownian force varies with frequency. In general the Brownian force is not constant across frequency and is therefore not white noise. That is, the force generated by the thermal motion of atoms is not delta correlated in time for real fluid-structure systems [24, 59]. The fluctuation-dissipation theorem is a powerful tool to describe the stochastic dynamics of a system from strictly deterministic calculations.

2 Dynamics of Micro and Nanoscale Cantilevers in Fluid

Micron and nanoscale cantilevers are of broad interest in science and technology. Often the motion of the cantilever is measured and quantified by the spectral density of the tip dynamics. For example, the spectral density of tip-deflection is given by the magnitude of the Fourier transform of the cantilever displacement. The spectrum depends upon the dynamical variable used. In addition, different types of driving yield different spectra. In the case of cantilever fluctuations excited by the thermal motion of atoms, the result is the noise spectrum. For an externally driven cantilever the spectrum is the power spectrum. Analytical expressions for these spectra are available using a two-dimensional approximation for the fluid dynamics. In order to quantify the complete three-dimensional cantilever motion it is necessary to apply a numerical approach. Such an approach is capable of calculating the noise and power spectra for any cantilever configuration.

2.1 Chapter Overview

This chapter presents analytical derivations for the noise and power spectra of tip-deflection and tip-angle. In addition, the numerical approach to calculating the noise and power spectra is described. This method uses the thermodynamic approach and linear response theory to determine the stochastic dynamics from deterministic motion. A description of the thermodynamic approach is presented, followed by the derivations using approximate analytics and a description of the numerical approach. Figure 7 gives a guide to the analytical derivations presented, in addition to the procedure for calculating the spectra from numerics. The assumptions made for analytics and numerics are shown Table 2.

2.2 Stochastic Cantilever Dynamics: Linear Response Theory

The fluctuation-dissipation theorem relates the stochastic motion of a system to its deterministic dynamics. In other words it relates the mechanism of energy dissipation, as a macroscopic object approaches equilibrium, to the mechanism of energy absorption in equilibrium due to the thermally induced motion of molecules. For a cantilever in fluid, the energy dissipation is dominated by the viscous interactions of the surrounding fluid molecules.

Using the fluctuation-dissipation theorem the stochastic fluctuations of a cantilever in viscous fluid can be calculated from deterministic computations of the viscous dissipation. In the case where the system is quite complicated, it is simpler to use linear response theory [59]. Linear response theory states that for a small perturbation, the conjugate dynamical variable that describes the elastic system will be linearly coupled to the applied perturbation. It is convenient to look at the special case of the removal of a step source,

$$\psi(t) = \begin{cases} \Psi_0 & \text{for } t < 0 \\ 0 & \text{for } t \geq 0. \end{cases} \tag{7}$$

Here Ψ_0 is the constant magnitude of the step source. A schematic of the normalized step source is plotted in Fig. 8(left). The response of the corresponding dynamical variable is then directly related to the autocorrelation of equilibrium fluctuations in that variable,

$$\langle a(0)a(t)\rangle = k_B T \frac{A(t)}{\Psi_0}. \tag{8}$$

The left side of Eq. (8) is the equilibrium autocorrelation in fluctuations of $a(t)$. In our notation lower-case variables denote stochastic quantities, such as the fluctuations in the dynamical variable, $a(t)$. Upper-case variables denote deterministic quantities, such as the deterministic response of the system to the removal of a step source, $A(t)$. The deterministic response $A(t)$ and the

stochastic autocorrelation $\langle a(0)a(t)\rangle$ are shown schematically in Fig. 8(right). Equation (8) is valid for any linear step perturbation applied to the system.

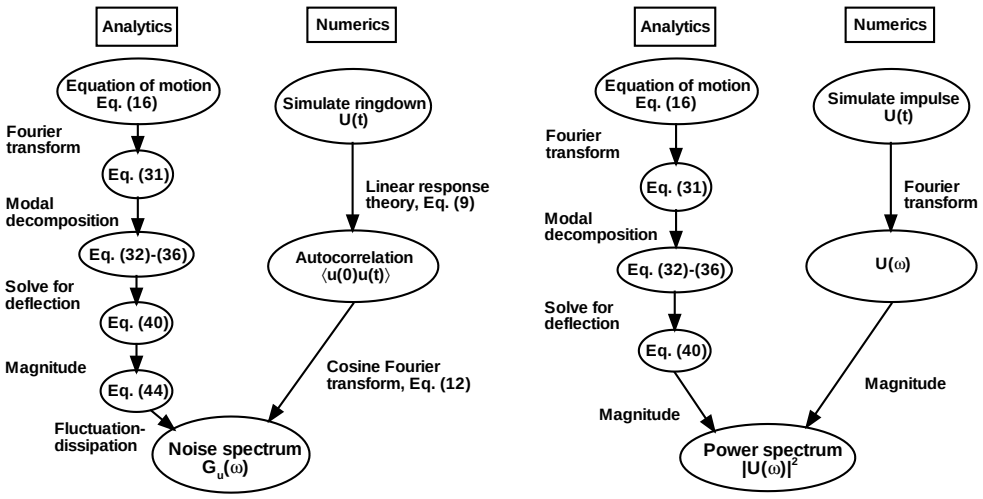

Figure 7: (left) Analytical and numerical approach for calculating the noise spectrum. (right) Analytical and numerical approach for calculating the power spectrum. The approaches are for cantilever deflection, however the results for cantilever angle are derived in a similar manner.

The cases of cantilever tip-deflection and tip-angle measurements are considered in order to connect with experimental efforts. For experiments using a scanning tunneling microscope [11] or peizoelectric measurements [5] the tip-deflection is measured, and the conjugate perturbation is a step point-force applied at the cantilever tip as shown in Fig. 9(left). An expression for the autocorrelation of fluctuations in cantilever tip-deflection has been derived previously [59]. The corresponding applied force is,

$$f(t) = \begin{cases} F_0 & \text{for } t < 0 \\ 0 & \text{for } t \geq 0. \end{cases} \tag{9}$$

The autocorrelation of equilibrium tip-deflection fluctuations is related to the

deterministic deflection resulting from the removal of the step force,

$$\langle u(0)u(t)\rangle = k_B T \frac{U(t)}{F_0}. \tag{10}$$

Here $u(t)$ is the stochastic fluctuation of cantilever tip-deflection and $U(t)$ is the deterministic response of the cantilever tip-deflection to the removal of a step point force.

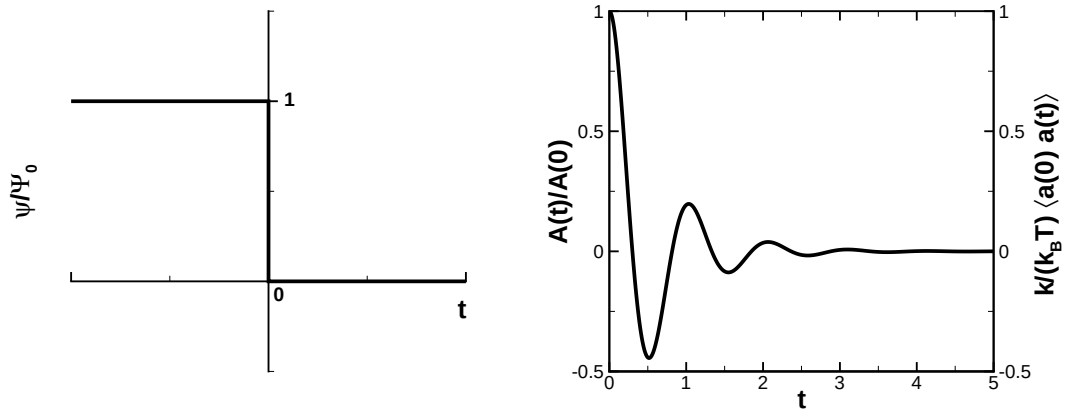

Figure 8: (left) A schematic of the removal of a step source used in linear response theory. The source is normalized by Ψ_0 and t is time. The system response to this source is related to the autocorrelation. (right) The ringdown of the dynamical variable $A(t)$ and the autocorrelation of $a(t)$.

In experiments it is also common to use optical techniques to measure the angle of the cantilever tip [40]. For this measurement approach, the cantilever tip-angle is conjugate to a step point-torque applied at the cantilever tip as shown in Fig. 9(right),

$$\tau(t) = \begin{cases} \tau_0 & \text{for } t < 0 \\ 0 & \text{for } t \geq 0. \end{cases} \tag{11}$$

The fluctuations in cantilever tip-angle $\theta(t)$ are then related to the response of the cantilever to the step torque $\Theta(t)$ by,

$$\langle \theta(0)\theta(t)\rangle = \frac{k_B T}{\tau_0}\Theta(t). \tag{12}$$

Analytics	Numerics
Classical mechanics	Classical mechanics
Continuum hypothesis	Continuum hypothesis
Uniform cross-section	
Homogenous properties	
Two-dimensional flow	
Infinite fluid	

Table 2: The assumptions made for analytical and numerical calculations of cantilever noise and power spectra.

Using Eq. (10) or (12) yields the autocorrelation of stochastic tip-deflection or tip-angle directly from the deterministic response of the cantilever to the removal of a step force or torque.

It should be emphasized that the deterministic tip-deflection or tip-angle response can be calculated using analytical theory, simplified models, or numerical simulations. The expressions above show that the deterministic motion of a cantilevered beam is directly related to the stochastic dynamics of that beam. An analysis of the deterministic dynamics of a microscopic cantilever will therefore yield important insight into its stochastic motion.

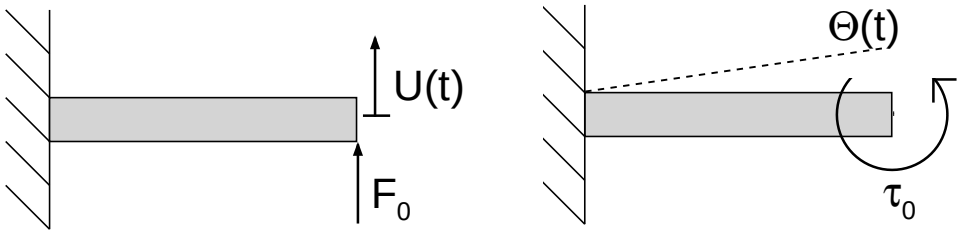

Figure 9: (left) The cantilever tip-deflection $U(t)$ is conjugate to a step point force at the tip F_0. (right) The cantilever tip-angle $\Theta(t)$ is conjugate to a step point torque at the tip τ_0.

The tip-deflection and tip-angle noise spectra are the spectral density of cantilever tip-deflection and tip-angle due to the Brownian force. These spectra are directly related to the autocorrelation of equilibrium fluctuations in the corresponding variable. The noise spectra are calculated using the real part of the Fourier transform,

$$G_u(\omega) = 4\int_0^\infty \langle u(0)u(t)\rangle \cos(\omega t)dt, \tag{13}$$

$$G_\theta(\omega) = 4\int_0^\infty \langle \theta(0)\theta(t)\rangle \cos(\omega t)dt. \tag{14}$$

Here the 4 comes from the definition of the spectral density for a random process [59]. These are the noise spectra for the cantilever tip motion and represent precisely the quantity measured in experiments. In this notation the subscript of G indicates the variable over which the noise spectrum is measured: G_θ is the noise spectrum for equilibrium fluctuations of tip-angle and G_u is the noise spectrum for equilibrium fluctuations of tip-displacement.

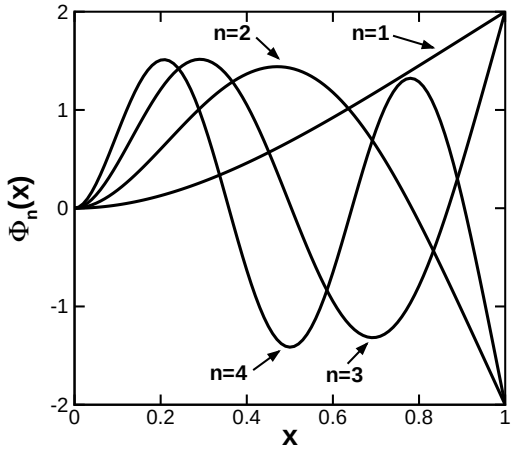

Figure 10: The first four normalized mode shapes for a cantilever with uniform cross-section.

There is no general analytical expression for the interaction between a three-dimensional cantilever and a viscous fluid. Instead, approximate models must be employed. The most common model is a two-dimensional approximation for the flow around a cantilever in fluid. The flow is modeled as that around an infinite cylinder oscillating transversely in viscous fluid. This model assumes that the cantilever has a uniform cross-section and is long and thin. In this case there is no three-dimensional flow around the bulk of the cantilever, and the flow around the end is neglected. Analytical expressions for the spectra of cantilever fluctuations due to thermal and external driving forces can be derived using infinite cylinder theory. The resulting expressions give insight into the dynamics of microscopic cantilevers. In situations where the two-dimensional approximations are not valid, the three-dimensional fluid-structure dynamics must be computed using numerical simulations.

2.3 Approximate Dynamics of a Cantilever in Fluid: Infinite Cylinder Theory

The infinite cylinder approximation is a popular model for viscous fluid flow around a microscopic rectangular cantilever [29, 69]. This model assumes that the beam is much longer than it is wide or thick ($L \gg w \gg h$), such that three-dimensional flow characteristics can be neglected. A solution to the Navier-Stokes equation for the force exerted by a fluid on an infinite cylinder was presented by Stokes [73]. The hydrodynamic function $\Gamma(\omega)$ presented by Rosenhead [65] is the dimensionless force per unit length on an infinite cylinder due to the surrounding fluid. For moderate flexural mode number ($n \lesssim 4$) the flow is two-dimensional and the hydrodynamic function is,

$$\Gamma(\omega) = 1 + \frac{4iK_1(-i\sqrt{iR})}{\sqrt{iR}K_0(-i\sqrt{iR})}. \tag{15}$$

In this expression $i = \sqrt{-1}$, K_0 and K_1 are modified Bessel functions, and R is the frequency based Reynolds number given by,

$$R = \frac{\omega w^2}{4\nu_f}. \tag{16}$$

Here w is the cantilever width, ν_f is the kinematic viscosity of the fluid, and ω is frequency. For the case of large mode number the flow along the beam length can not be neglected and the hydrodynamic function becomes a function of mode number [75]. In this discussion the calculations are confined to the first three modes and the hydrodynamic function given in Eq. (15) is sufficiently accurate. A modified expression for the hydrodynamic function on a rectangular cross-section is available [74] that is valid over a broad range of Reynolds number [69]. Assuming that the flow everywhere on the beam is given by an oscillating cylinder, it remains to compute the beam motion using Euler-Bernoulli beam theory [49].

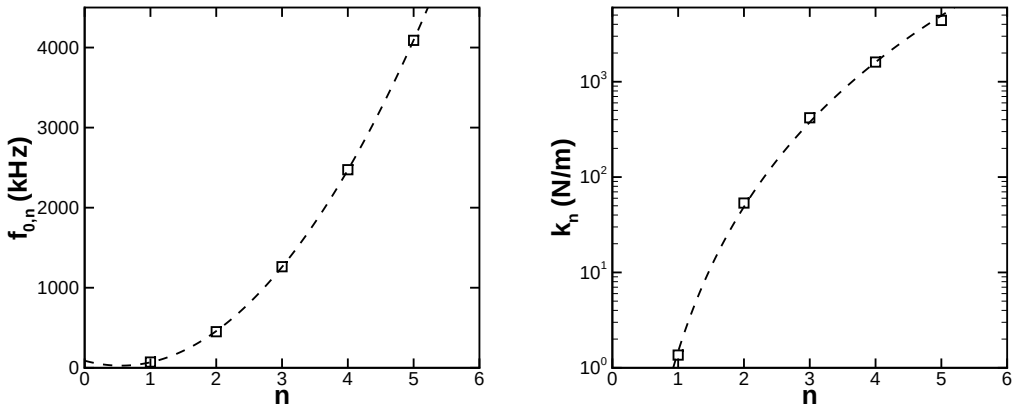

Figure 11: The vacuum resonance frequencies for the C2 rectangular cantilever as a function of mode number, $f_{0,n} = \omega_{0.n}/(2\pi)$. The dashed line is a curve fit, $f_{0,n}/(1000) = 205.3n^2 - 225.6n + 88.9$. (right) The dynamic spring constants for the C2 rectangular cantilever as a function of mode number. The dashed line is a power law curve fit, $k_n = 1.48n^{5.039}$.

n	$\omega_{0,n}(10^3$ rad/s)	$m_{e,n}$ (kg)	k_n (N/m)
1	452	$m_c/4$	1.360
2	2830	–	53.41
3	7930	–	418.7
4	15500	–	1608.0
5	25700	–	4393.9

Table 3: The resonant frequency in vacuum, effective mass, and spring constant for the first five modes of a cantilevered beam. The effective mass is constant for all modes, $m_{e,n} = 6.65$ng.

2.3.1 Cantilever Modal Frequencies and Mode Shapes

The Euler-Bernoulli beam equation must be solved with the fluid force acting on its surface [75]. The Euler-Bernoulli beam equation is valid for beams with uniform cross-section, homogenous material properties, and small deflections in a single direction. It is given by,

$$\mu\frac{\partial^2 U(x,t)}{\partial t^2} + \frac{EI}{L^4}\frac{\partial^4 U(x,t)}{\partial x^4} = F_f(x,t) + F_D(x,t), \tag{17}$$

where μ is the mass per unit length, L is the cantilever length, E is Young's modulus, $I = wh^3/12$ is the moment of inertia for a rectangular cantilever, $F_f(x,t)$ is the force due to the fluid-structure interaction, $F_D(x,t)$ is the external driving applied to the beam, and $U(x,t)$ is the transverse deflection of the beam along the length. Also, $x = x^*/L$ is the normalized axial coordinate and forces F_f and F_D are per unit length.

A cantilevered beam oscillates at an infinite number of frequencies corresponding to an infinite number of modes [49]. The modes of free vibration for a beam can be calculated from the unforced Euler-Bernoulli beam equation,

$$\mu\frac{\partial^2 U(x,t)}{\partial t^2} + \frac{EI}{L^4}\frac{\partial^4 U(x,t)}{\partial x^4} = 0. \tag{18}$$

By assuming a solution of the form $U(x,t) = \Phi_n(x)\cos(\omega_n t + \beta)$ this partial

differential equation reduces to the ordinary differential equation,

$$\frac{d^4\Phi_n(x)}{dx^4} - c_n^4\Phi_n(x) = 0. \tag{19}$$

In the above equation n is the mode number, $c_n^4 = \mu\omega_{0,n}^2 L^4/EI$ are the eigenvalues for each mode, and $\omega_{0,n}$ are the resonant frequencies in vacuum for each mode,

$$\omega_{0,n} = \frac{c_n^2}{L^2}\sqrt{\frac{EI}{\mu}}. \tag{20}$$

The vacuum frequencies are shown in Table 3 and plotted in Fig. 11 (left). The solution to Eq. (19) is [49, 80],

$$\begin{aligned}\Phi_n(x) &= M_1\left[\cos c_n x + \cosh c_n x\right] + M_2\left[\cos c_n x - \cosh c_n x\right] \\ &+ M_3\left[\sin c_n x + \sinh c_n x\right] + M_4\left[\sin c_n x - \sinh c_n x\right].\end{aligned} \tag{21}$$

This equation gives the deflection of a beam for a given mode, where the M_i are constants. These constants are determined from the fixed and free boundary conditions for a cantilever. At the fixed end $\Phi_n(0) = \Phi_n'(0) = 0$, which yields $M_1 = M_3 = 0$. At the free end $\Phi_n''(1) = \Phi_n'''(1) = 0$, which yield an expression for M_2 and M_4,

$$M_4 = M_2\frac{-\cos(c_n) - \cosh(c_n)}{\sin(c_n) + \sinh(c_n)}. \tag{22}$$

Substituting into Equation (21) gives,

$$\begin{aligned}\Phi_n(x) &= -\left(\cos c_n + \cosh c_n\right)\left(\cos c_n x - \cosh c_n x\right) \\ &- \left(\sin c_n - \sinh c_n\right)\left(\sin c_n x - \sinh c_n x\right).\end{aligned} \tag{23}$$

This expression can be normalized such that the deflection of each mode is the same. The result is,

$$\begin{aligned}\Phi_n(x) &= \left(\cos c_n x - \cosh c_n x\right) \\ &+ \frac{\cos c_n L + \cosh c_n L}{\sin c_n L + \sinh c_n L}(\sinh c_n x - \sin c_n x).\end{aligned} \tag{24}$$

	$L(\mu\text{m})$	$w(\mu\text{m})$	$h(\mu\text{m})$	k (N/m)	k_t (N-m/rad)	f_0 (kHz)
(1)	197	29	2	1.3	1.6×10^{-8}	71
(2)	140	15.6	0.6	0.1	8.9×10^{-10}	38
(3)	100	13.4	0.4	0.08	2.5×10^{-10}	32

Table 4: Summary of the cantilever geometries and material properties. (1) The rectangular cantilever. (2) The Veeco MLCT Type E microlever [76]. (3) The Olympus OMCL-TR400PSA lever. The geometry is given by the cantilever length L, width w, and height h. For the Veeco and Olympus cantilevers the total length between the two arms at the base is $b = 161.64\mu$m and $b = 106\mu$m. The cantilever spring constant k, torsional spring constant k_t, and resonant frequency in vacuum f_0 are determined using finite element numerical simulations. The cantilevers are immersed in water with density $\rho = 997$ kg/m^3 and dynamic viscosity $\mu_f = 8.59 \times 10^{-4}$ kg/m-s.

The eigenvalue c_n is the n^{th} solution to the characteristic equation,

$$1 + \cos c_n \cosh c_n = 0. \tag{25}$$

The first 4 normalized mode shapes are shown in Fig. 10. The first mode increases continually, and higher modes have more complex shapes. Each mode shape $\Phi_n(x)$ has n nodes (or points where $\Phi_n(x) = 0$) including the shared node at $x = 0$. It should be noted that even number modes have tip-deflection with signs opposite to odd numbered modes.

Using the mode shapes it is possible to calculate the spring constant for each mode. For a given applied force the displacement of each mode at the tip can be quantified by the dynamic spring constants k_n for each mode. These values can be calculated by equating the bending energy of the mode with the potential energy of a mass on a spring by

$$\frac{1}{2}k_n\Phi_n^2(1) = \frac{EI}{2L^3}\int_0^1 \Phi_n''(x)^2 dx. \tag{26}$$

The integral on the right side of Eq. (26) is equal to c_n^4. The dynamic spring constants for the first five modes are shown in Table 3 and plotted in Fig. 11

(right) for the C2 cantilever, see Table 4. The convention used to define the cantilever geometry is shown in Fig. 12 (left). The bulk cantilever spring constant can be calculated from beam theory [49],

$$k = \frac{3EI}{L^3}. \tag{27}$$

The dynamic spring constants for each mode are related to the bulk cantilever spring constant by,

$$k_n = \frac{c_n^4}{12}k = \frac{c_n^4 EI}{4L^3}. \tag{28}$$

Note that c_n increases with mode number, so the modal spring constants increase with mode number. This indicates that the oscillations of higher modes are successively smaller in magnitude.

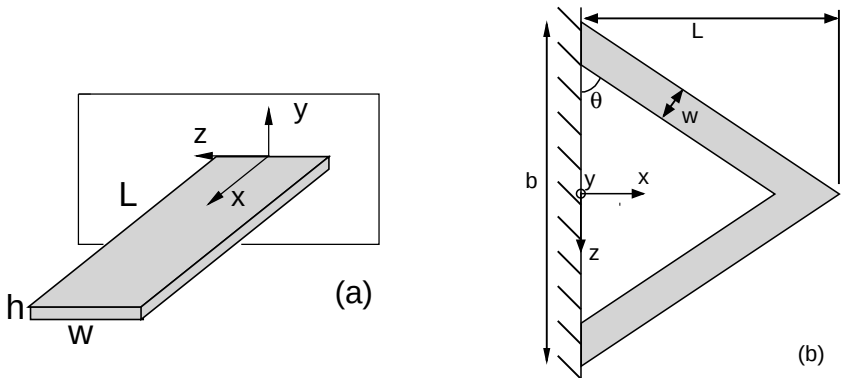

Figure 12: Schematics of the two micron scale cantilever geometries considered (not drawn to scale). Panel (a), A rectangular cantilever with aspect ratios $L/h = 98.5$, $w/h = 14.5$, and $L/w = 6.8$. The cantilever is composed of silicon with density $\rho_c = 2329$ kg/m^3 and Youngs Modulus $E = 174$ GPa. Panel (b), A V-shaped cantilever with aspect ratios $L/h = 233$, $w/h = 30$, and $L/w = 7.8$. The total width between the two arms normalized by the width of a single arm is $b/w = 10.36$. The cantilever planform is an equilateral triangle with $\theta = \pi/3$. The cantilever is composed of silicon nitride with $\rho_c = 3100$kg/m^3 and $E = 172$GPa. The specific dimensions for the rectangular and V-shaped cantilever are given in Table 4.

2.3.2 Analytical Description of Cantilever Dynamics in a Viscous Fluid

The Fourier transform of the fluid force per unit length acting on a two-dimensional cantilever is,

$$\hat{F}_f(\omega) = m_{cyl}\omega^2\Gamma(\omega)\hat{U}(x|\omega), \tag{29}$$

where $\Gamma(\omega)$ is the hydrodynamic function, $m_{cyl} = (\pi/4)\rho w^2$ is the mass of a cylinder of fluid per unit length, and ρ is the density of the fluid. The hat notation ($\hat{}$) indicates a Fourier transform, and $\hat{U}(x|\omega)$ is the Fourier transform of the cantilever deflection. The notation $(x|\omega)$ indicates that x is in real space and t is in Fourier space. The convention used for the Fourier transform pair is,

$$\hat{U}(\omega) = \int_{-\infty}^{\infty} U(t)e^{i\omega t}dt, \tag{30}$$

$$U(t) = \frac{1}{2\pi}\int_{-\infty}^{\infty} \hat{U}(\omega)e^{-i\omega t}d\omega. \tag{31}$$

The fluid force F_f is the force on a cross-section of the cantilever [74]. For an infinite cylinder the fluid force is defined in terms of the hydrodynamic function for a cylindrical cross-section [65], see Eq. (15). The Fourier transform of Eq. (17) is,

$$\frac{\partial^4\hat{U}(x|\omega)}{\partial x^4} - \frac{\mu L^4}{EI}\omega^2\hat{U}(x|\omega) = \frac{L^4}{EI}\left(\hat{F}_f(x|\omega) + \hat{F}_D(x|\omega)\right). \tag{32}$$

This is the equation of motion for the deflection of a cantilever in fluid for an arbitrary driving force. For small deflections the fluid does not couple the modes and the cantilever deflection can be separated into contributions from individual modes,

$$\hat{U}_n(x|\omega) = \hat{f}_n(\omega)\Phi_n(x), \tag{33}$$

$$\hat{U}(x|\omega) = \sum_{n=1}^{\infty}\hat{U}_n(x|\omega). \tag{34}$$

In the above expressions $\hat{U}(x|\omega)$ is the total beam deflection and $\hat{U}_n(x|\omega)$ is the frequency dependent beam deflection as a function of axial distance x for mode n. Also, $\hat{f}_n(\omega)$ is the frequency dependence of the cantilever dynamics for each mode and accounts for the cantilever motion in response to the fluid and driving forces. Substituting Eq. (33) and (34) into the equation of motion Eq. (32) yields,

$$\sum_{n=1}^{\infty}\left(\frac{\partial^4\Phi_n(x)}{\partial x^4}\hat{f}_n(\omega)-\frac{L^4}{EI}\omega^2\hat{f}_n(\omega)\Phi_n(x)(\mu+m_{cyl}\Gamma(\omega))\right)= \sum_{n=1}^{\infty}\frac{L^4}{EI}\hat{F}_D(x|\omega). \tag{35}$$

This expression can be simplified by multiplying both sides by $\Phi_m(x)$ and integrating over the length of the cantilever. The mode shapes form an orthonormal basis set,

$$\int_0^1\Phi_n(x)\Phi_m(x)dx=\begin{cases}1 & \text{for } n=m\\ 0 & \text{for } n\neq m\end{cases}. \tag{36}$$

Applying this to Eq. (35) yields,

$$c_n^4\hat{f}_n(\omega)-\frac{L^4}{EI}\omega^2\hat{f}_n(\omega)(\mu+m_{cyl}\Gamma(\omega))=\frac{L^4}{EI}\int_0^1\hat{F}_D(x'|\omega)\Phi_n(x')dx'. \tag{37}$$

Solving for the frequency dependent motion of an individual cantilever mode yields,

$$\hat{f}_n(\omega)=\frac{\int_0^1\Phi_n(x')s_D(x'|\omega)dx'}{c_n^4-B_n^4(\omega)}. \tag{38}$$

In this expression $B_n(\omega)$ accounts for the force of the fluid and is related to the hydrodynamic function,

$$B_n(\omega)=c_1\left(\frac{\omega}{\omega_0}\right)^{1/2}\left[1+\frac{\pi\rho w}{4\rho_c h}\Gamma(\omega,n)\right]^{1/4}. \tag{39}$$

Here ω_0 is the resonant frequency of the first cantilever mode in vacuum, ρ_c is the cantilever density, ρ is the fluid density, and w and h are the cantilever

width and height. For moderate mode number the hydrodynamic function in Eq. (39) is independent of mode number [75] and therefore $B_n(\omega) = B(\omega)$ and is independent of mode number. The function $s_D(x|\omega)$ is the Fourier transform of the normalized external force on the beam,

$$s_D(x|\omega) = \frac{L^4}{EI}\hat{F}_D(x|\omega). \tag{40}$$

The Fourier transform of the cantilever deflection due to an arbitrary driving force $\hat{F}_D$ as a function of frequency for mode n is then,

$$\hat{U}_n(x|\omega) = \frac{L^4\Phi_n(x)}{EI(c_n^4 - B^4(\omega))}\int_0^1 \Phi_n(x')\hat{F}_D(x'|\omega)dx', \tag{41}$$

where,

$$\hat{U}(x|\omega) = \sum_{n=1}^{\infty}\hat{U}_n(x|\omega). \tag{42}$$

This is the deflection of a cantilever in fluid due to any driving force. For a cantilever driven by the Brownian force this expression will yield the stochastic fluctuations, while for an external driving it yields the driven oscillations of the cantilever.

2.3.3 Thermally Driven Cantilever Fluctuations

For the case of a thermally excited cantilever the driving force $\hat{F}_D(x|\omega) = \hat{F}'_{B,n}(\omega)$. Note that $\hat{F}'_{B,n}(\omega)$ is a force per unit length for each mode unlike $\hat{F}_B(\omega)$, where $|\hat{F}_B(\omega)|^2 = G_F$. In order to obtain the correct shape for mode n the relationship between these two must be,

$$L\int_0^1 F'_{B,n}(\omega)\Phi_n(x')dx' = \hat{F}_B(\omega). \tag{43}$$

Applying the Brownian force in Eq. (17) yields a Langevin equation; a stochastic partial differential equation. Note that Eq. (43) is the same integral found in

the numerator of Eq. (38). The deflection for mode n in fluid due to a Brownian force is then,

$$\hat{u}_n(x|\omega) = \frac{L^3}{EI}\frac{\hat{F}_B(\omega)}{c_n^4 - B^4(\omega)}\Phi_n(x). \tag{44}$$

The deflection is stochastic as indicated by the lower case variable $\hat{u}_n(x|\omega)$. The magnitude of this is the noise spectrum of deflections for an individual mode,

$$|\hat{u}_n(x|\omega)|^2 = \frac{L^6}{(EI)^2}\frac{|\hat{F}_B(\omega)|^2}{|c_n^4 - B^4(\omega)|^2}\Phi_n^2(x). \tag{45}$$

The noise spectrum for the deflection of the beam including all modes is then,

$$|\hat{u}(x|\omega)|^2 \;=\; \left|\sum_{n=1}^{\infty}\frac{L^3}{EI}\frac{\Phi_n(x)}{c_n^4 - B^4(\omega)}\right|^2 |\hat{F}_B(\omega)|^2 \tag{46}$$

In the absence of an exact analytical expression, Γ is obtained from infinite cylinder approximations. The cantilever noise spectrum is the precise quantity measured in experiments.

The spectral density of the Brownian force is proportional to the viscous damping through the fluctuation-dissipation theorem,

$$|\hat{F}_B(\omega)|^2 = G_F(\omega) = 4k_BT\gamma_f(\omega). \tag{47}$$

Substituting this result into the noise spectrum of Eq. (45) yields the result for mode n,

$$G_{u,n}(x|\omega) = \frac{4k_BTL^6}{(EI)^2}\frac{\gamma_f(\omega)}{|c_n^4 - B^4(\omega)|^2}\Phi_n^2(x). \tag{48}$$

Similarly, the noise spectrum for the total beam motion is calculated by substituting Eq. (47) into Eq. (46),

$$G_u(x|\omega) \;=\; 4k_BT\gamma_f(\omega)\left(\frac{L^3}{EI}\right)^2\left|\sum_{n=1}^{\infty}\frac{\Phi_n(x)}{c_n^4 - B^4(\omega)}\right|^2. \tag{49}$$

This expression assumes the viscous damping $\gamma_f(\omega)$ is independent of mode number. This is valid for moderate mode number, $n \lesssim 4$ [75]. The tip-deflection

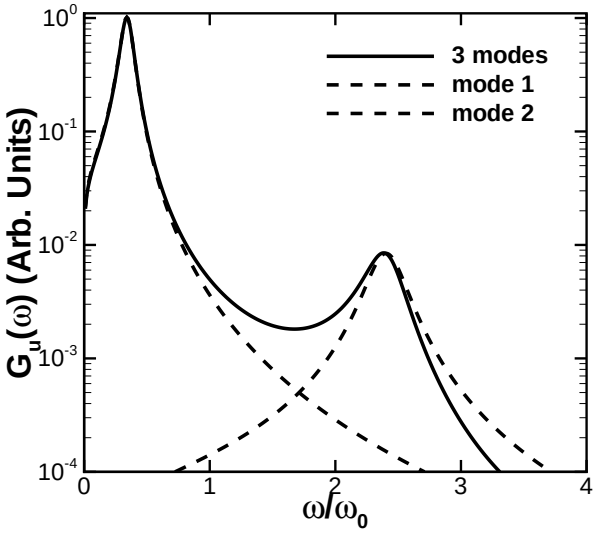

Figure 13: Analytical predictions of the tip-deflection noise spectrum $G_u(\omega)$ using infinite cylinder approximations for three modes (solid) and modes 1 and 2 individually (dashed).

noise spectrum for the total cantilever motion is shown in Fig. 13 along with the contributions from modes one and two. The differences between the total cantilever noise spectrum and the individual mode spectra are due to phase shifts between the individual modes.

The noise spectrum must satisfy equipartition of energy. For simplicity the noise spectrum for an individual mode is considered, though the discussion is equally relevant to the total cantilever noise spectrum. Substituting $B(\omega)$ in the modal noise spectrum Eq. (48) gives,

$$G_{u,n}(x|\omega) = \frac{4k_BTL^6}{(EI)^2} \frac{\gamma_f(\omega)}{\left| c_n^4 (1 - \left(\frac{c_1}{c_n}\right)^4 \left(\frac{\omega}{\omega_0}\right)^2 (1 + T_0\Gamma(\omega)) \right|^2} \Phi_n^2(x). \tag{50}$$

The ratio of the coefficients c_n can be written as a ratio of mode frequencies,

$$\frac{\omega_0}{\omega_{0,n}} = \left(\frac{c_1}{c_n}\right)^2 \tag{51}$$

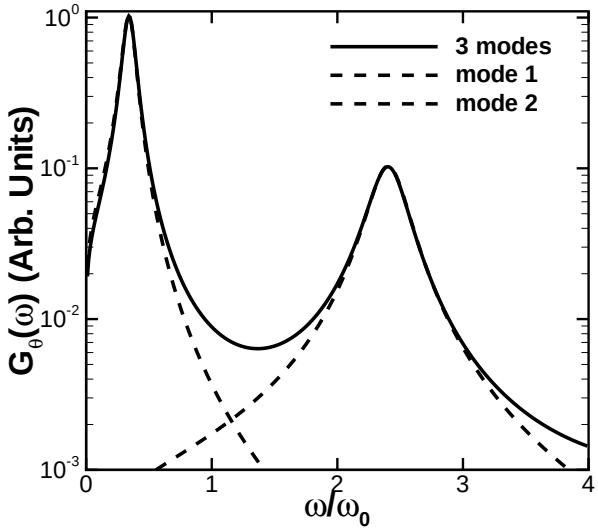

Figure 14: Analytical predictions of the tip-angle noise spectrum $G_\theta(\omega)$ using infinite cylinder approximations for three modes (solid) and modes 1 and 2 individually (dashed).

Here $\omega_{0,n}$ is the resonance frequency in vacuum for mode n given by Eq. (20). Substituting Eq. (51), the equation for the bulk spring constant Eq. (27), and the normalized frequency $\tilde{\omega}_n = \omega/\omega_{0,n}$ into Eq. (50) yields,

$$G_{u,n}(x|\omega) = \frac{36 k_B T}{k^2} \frac{\gamma_f(\omega)}{\left|c_n^4((1-\tilde{\omega}_n^2(1+T_0\Gamma_r(\omega))) + i\tilde{\omega}_n^2 T_0 \Gamma_i(\omega))\right|^2} \Phi_n^2(x). \quad (52)$$

In this expression Γ_i and Γ_r are the real and imaginary parts of the hydrodynamic function given in Eq. (15),

$$\Gamma(\omega) = \Gamma_r(\omega) + i\Gamma_i(\omega). \quad (53)$$

The viscous fluid damping can be written in terms of the imaginary part of the hydrodynamic function,

$$\gamma_f(\omega) = m_{cyl}\omega_n \tilde{\omega}_n \Gamma_i(R_n\tilde{\omega}_n) = m_c T_0 \omega_n \tilde{\omega}_n \Gamma_i(R_n\tilde{\omega}_n). \quad (54)$$

Eq. (52) can be simplified by substituting in Eq. (54) and the relationship between the bulk spring constant k and the modal spring constants k_n given in Eq. (28). Calculating the magnitude of the resulting expression gives,

$$G_{u,n}(x|\omega) = \frac{3k_BT}{(k_n/c_n^4)^2}\frac{m_cT_0\omega_n\tilde{\omega}_n\Gamma_i}{c_n^8((1-\tilde{\omega}_n^2(1+T_0\Gamma_r))^2+(\tilde{\omega}_n^2T_0\Gamma_i)^2)}\Phi_n^2(x). \tag{55}$$

This can be further simplified by the relation between effective mass, modal spring constant and resonant frequency in vacuum, $m_{e,n} = \alpha_n m_c = k_n/\omega_{0,n}^2$. Here α_n is the coefficient such that the kinetic energy of a lumped mass is equal to the kinetic energy of the cantilevered beam for each mode, and $m_c = \rho_c Lwh$ is the actual cantilever mass. The spring constants k_n are given by Eq. (28) and the resonant frequencies from beam theory Eq. (20). The spring constant, coefficient α_n, and resonant frequency for a mode are related by,

$$\omega_{0,n}^2 = \frac{k_n}{\alpha_n m_c}, \tag{56}$$

$$\alpha_n = \frac{k_n}{m_c\omega_{0,n}^2}. \tag{57}$$

The coefficient $\alpha = 1/4$ for all cantilever modes and therefore yields a constant $m_{e,n}$ for all modes. Substituting this result into Eq. (55) gives,

$$G_{u,n}(x|\omega) = |u_n(x|\omega)|^2 = \frac{k_BT}{\omega_n k_n}\frac{T_0\tilde{\omega}_n\Gamma_i}{((1-\tilde{\omega}_n^2(1+T_0\Gamma_r))^2+(\tilde{\omega}_n^2T_0\Gamma_i)^2)}\Phi_n^2(x). \tag{58}$$

This is the noise spectrum of fluctuations in cantilever deflection for mode n at any point on the beam as a function of frequency. Using the normalized mode shapes from Eq. (24) and taking the value at the tip ($x = 1$), the noise spectrum of tip-deflection fluctuations is then identical to the expression shown in [59],

$$G_{u,n}(\omega) = \frac{4k_BT}{\omega_n k_n}\frac{T_0\tilde{\omega}_n\Gamma_i}{((1-\tilde{\omega}_n^2(1+T_0\Gamma_r))^2+(\tilde{\omega}_n^2T_0\Gamma_i)^2)}. \tag{59}$$

The beam motion must satisfy equipartition of energy [21]. Each quadratic mode of energy absorbs $k_BT/2$ from the thermal bath. Therefore the potential

energy of each mode receives $k_BT/2$ of energy,

$$\frac{1}{2}k_n\left(\frac{1}{2\pi}\int_0^\infty G_{u,n}(\omega)d\omega\right) = \frac{k_BT}{2}, \tag{60}$$

or, more compactly,

$$\frac{1}{2\pi}\int_0^\infty G_{u,n}(\omega)d\omega = \frac{k_BT}{k_n}. \tag{61}$$

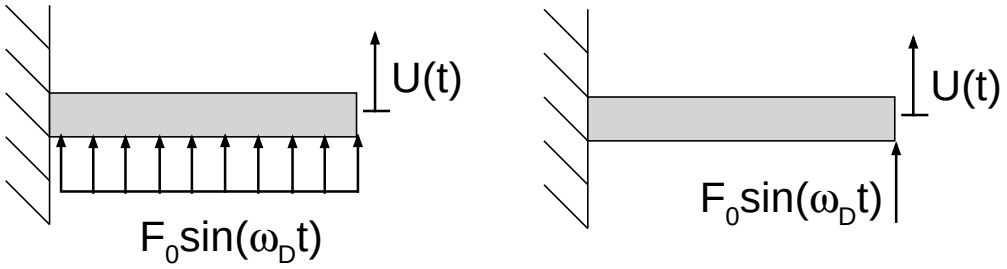

Figure 15: The cantilever can be driven by a sinusoidal force that is uniformly distributed along the length (left) or localized at the free end (right).

It is straightforward to derive the noise spectrum of equilibrium fluctuations in cantilever angle in a similar manner by using,

$$\hat{\theta}_n(x|\omega) \;=\; \hat{f}_n(\omega)\Phi_n'(x),. \tag{62}$$

In this equation $\Phi_n'(x)$ is the derivative of the mode shape with respect to x. This is related to the deflection in Eq. (33) by,

$$\hat{\theta}_n = \tan^{-1}\left(\frac{\partial\hat{u}_n}{\partial x}\right) = \tan^{-1}\left(\hat{f}_n(\omega)\frac{d\Phi_n}{dx}\right) \approx \hat{f}_n(\omega)\Phi_n'(x), \tag{63}$$

for small angles. The noise spectrum of fluctuations in cantilever angle is then,

$$G_\theta(x|\omega) \;=\; 4k_BT\gamma_f(\omega)\left(\frac{L^3}{EI}\right)\left|\sum_{n=1}^{\infty}\frac{\Phi_n'(x)}{c_n^4 - B_n^4(\omega)}\right|^2. \tag{64}$$

The expression for a single mode is,

$$G_{\theta,n}(x|\omega) = |\theta_n(x|\omega)|^2 = \frac{k_B T}{\omega_n k_n} \frac{T_0 \tilde{\omega}_n (\Phi_n'(x))^2 \Gamma_i}{((1-\tilde{\omega}_n^2(1+T_0\Gamma_r))^2 + (\tilde{\omega}_n^2 T_0 \Gamma_i)^2)}. \tag{65}$$

The tip-angle noise spectrum for the total cantilever motion is shown in Fig. 14 along with the contributions from modes one and two. The noise spectrum of tip-angle fluctuations must also satisfy equipartition of energy,

$$\frac{1}{2\pi} \int_0^\infty G_{\theta,n}(\omega) d\omega = \frac{k_B T}{k_{t,n}}. \tag{66}$$

Here $k_{t,n}$ is the torsional spring constant for mode n. The tip-angle noise spectrum distributes more energy to higher modes than the tip-deflection noise spectrum. This is due to the factor of $\Phi_n'(1)^2$ that arises in Eq. (65). The angle of the mode shape at the tip increases with mode number, while the magnitude of the mode shape at the tip is constant. This is evident from Fig. 10. The trend of $\Phi_n'(1)^2$ with mode number is shown in Fig. 16 (left)

2.3.4 Externally Driven Cantilever Fluctuations

Equations (49) and (64) quantify the motion of an infinite cylinder in fluid due to the Brownian force. This model approximates the dynamics of micro or nanoscale cantilevers in fluid in response to the thermal motion of atoms. Another case of interest is the dynamics of a cantilever in response to an externally applied driving. Expressions for the spectral density of externally driven cantilever dynamics can be derived in a similar manner to the noise spectrum in order to calculate the power spectrum. For the case of a sinusoidal driving force applied uniformly along the cantilever,

$$F_D(x,t) = F_0 \sin \omega_D t. \tag{67}$$

A schematic of this drive mechanism is shown in Fig. 15(left). In the frequency domain the driving force is,

$$\hat{F}_D(x|\omega) = F_0 \pi (\delta(\omega - \omega_D) + \delta(\omega + \omega_D)), \tag{68}$$

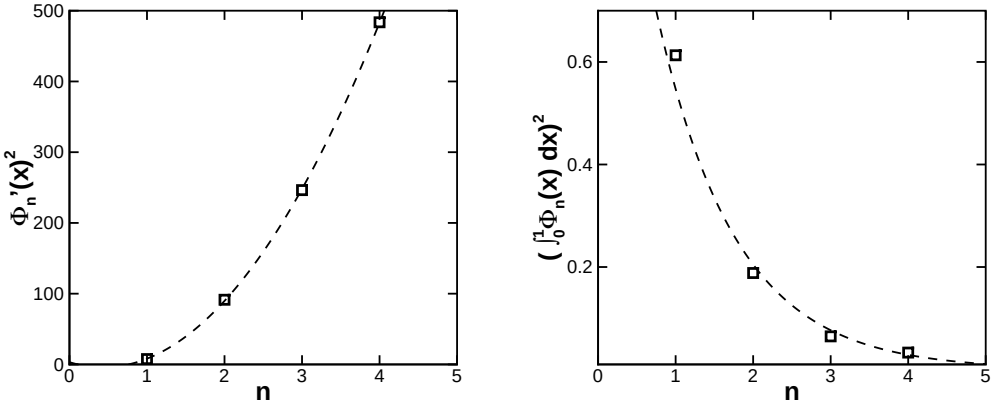

Figure 16: (left) The square of the angle of the mode shape at the tip as a function of mode number, n. This factor appears in the expression for tip-angle noise spectrum, and causes more energy to be distributed to higher modes. The dashed line is a quadratic fit, $\Phi_n'(x)^2 = 38.3n^2 - 33.4n + 3.2$. (right) The square of the integral of the mode shape as a function of mode number. This factor appears in the expression for power spectrum due to a uniform drive force, resulting in less energy in higher modes for this case than tip drive. The dashed line is an exponential fit, $\left(\int_0^1 \Phi_n dx\right)^2 = 1.46\exp(-0.983n)$.

where δ is the Dirac delta function. Substituting this into Eq. (41) yields,

$$\hat{U}_n(x|\omega) = \frac{L^4 F_0 \pi \Phi_n(x)}{EI(c_n^4 - B^4(\omega))}(\delta(\omega - \omega_D) + \delta(\omega + \omega_D)) \int_0^1 \Phi_n(x')dx'. \tag{69}$$

The only frequency for which this expression is nonzero occurs at $\omega = \pm\omega_D$. Considering this expression only at the drive frequency and then sweeping the drive frequency over all positive frequency gives,

$$\hat{U}_n(x|\omega) = \frac{L^4 F_0 \pi \Phi_n(x)}{EI(c_n^4 - B^4(\omega))} \int_0^1 \Phi_n(x')dx'. \tag{70}$$

The power spectrum of fluctuations in cantilever deflection for mode n is calculated as the modulus squared of Eq. (70),

$$|\hat{U}_n(x|\omega)|^2 = \left(\frac{\pi F_0}{2k_n}\right)^2 \frac{\left(\int_0^1 \Phi_n(x')dx'\right)^2}{(1 - \tilde{\omega}_n^2(1 + T_0\Gamma_r))^2 + (\tilde{\omega}_n^2 T_0 \Gamma_i)^2} \Phi_n^2(x). \tag{71}$$

Eq. (71) quantifies the cantilever oscillations for an individual mode in response to a sinusoidal force uniformly distributed along the beam. The corresponding power spectrum for the total cantilever deflection including all modes is,

$$|\hat{U}(x|\omega)|^2 = \left(\frac{L^4 F_0 \pi}{EI}\right)^2 \left|\sum_{n=1}^{\infty} \frac{\Phi_n(x)}{(c_n^4 - B_n^4(\omega))} \int_0^1 \Phi_n(x')dx'\right|^2 . \tag{72}$$

Eq. (72) is precisely the spectrum of interest in experiments measuring deflection due to a uniform force. The power spectrum of cantilever tip-deflection due to a uniform force is shown in Fig. 17 (left) along with the spectra for modes one and two.

Similarly, the power spectrum of fluctuations in cantilever angle for mode n due to a spatially uniform force that varies sinusoidally in time is,

$$|\hat{\Theta}_n(x|\omega)|^2 = \left(\frac{\pi F_0}{2k_n}\right)^2 \frac{\left(\int_0^1 \Phi_n(x')dx'\right)^2}{(1-\tilde{\omega}_n^2(1+T_0\Gamma_r))^2 + (\tilde{\omega}_n^2 T_0 \Gamma_i)^2} (\Phi_n'(x))^2. \tag{73}$$

The corresponding power spectra for the total cantilever angle including all modes is,

$$|\hat{\Theta}(x|\omega)|^2 = \left(\frac{L^4 F_0 \pi}{EI}\right)^2 \left|\sum_{n=1}^{\infty} \frac{\Phi_n'(x)}{(c_n^4 - B^4(\omega))} \int_0^1 \Phi_n(x')dx'\right|^2 . \tag{74}$$

Eq. (74) is precisely the spectrum of interest in experiments measuring cantilever angle in response to a uniform force. The power spectrum of cantilever tip-angle due to a uniform force is shown in Fig. 18 (left) along with the spectra for modes one and two.

In order to investigate how the driving method affects the frequency dependence of the power spectrum, consider a sinusoidal drive force applied at the cantilever tip. A schematic of this drive mechanism is shown in Fig. 15(right). For this case,

$$\hat{F}_D(x|\omega) = \pi F_0 \delta(x-1), \tag{75}$$

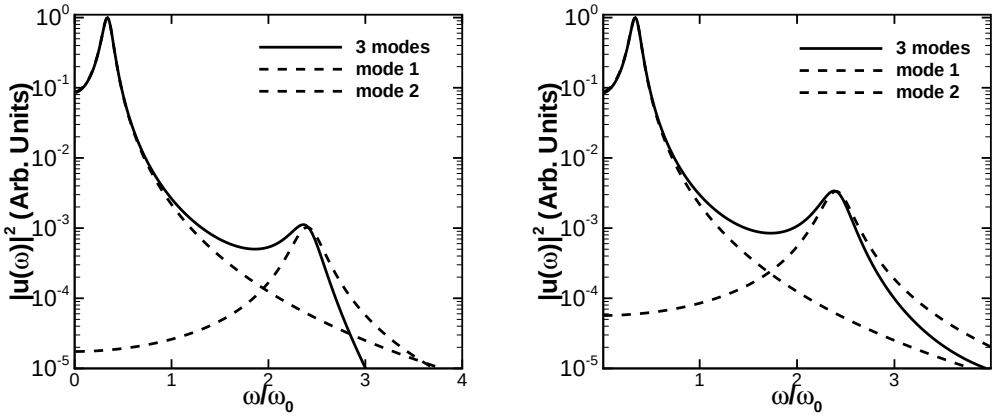

Figure 17: Analytical predictions of the tip-deflection power spectrum for a uniformly distributed force (left) and a force localized at the tip (right). The applied forces vary sinusoidally in time. The spectra are calculated using infinite cylinder approximations for three modes (solid) and modes 1 and 2 individually (dashed).

and the power spectrum is,

$$|\hat{U}_n(x|\omega)|^2 = \left(\frac{\pi F_0}{2k_n}\right)^2 \frac{\Phi_n^2(x)}{((1-\tilde{\omega}_n^2(1+T_0\Gamma_r))^2 + (\tilde{\omega}_n^2 T_0\Gamma_i)^2)}. \tag{76}$$

Eq. (76) quantifies the cantilever oscillations for an individual mode in response to a force localized at the cantilever free tip that varies sinusoidally in time. The power spectrum including contributions from all modes is,

$$|\hat{U}(x|\omega)|^2 = \left(\frac{L^4 F_0 \pi}{EI}\right)^2 \left|\sum_{n=1}^{\infty} \frac{\Phi_n(x)}{(c_n^4 - B_n^4(\omega))}\right|^2. \tag{77}$$

Equation (77) is precisely the spectrum of interest in experiments measuring deflection due to a tip force. The power spectrum of cantilever tip-deflection due to a tip force is shown in Fig. 17 (right) along with the spectra for modes one and two.

Similarly, the power spectrum of fluctuations in cantilever angle for mode n

due to a sinusoidally varying force at the tip is,

$$|\hat{\Theta}_n(x|\omega)|^2 = \left(\frac{\pi F_0}{2k_n}\right)^2 \frac{\Phi_n'(x)^2}{((1-\tilde{\omega}_n^2(1+T_0\Gamma_r))^2 + (\tilde{\omega}_n^2 T_0\Gamma_i)^2)}, \tag{78}$$

and for all modes,

$$|\hat{\Theta}(x|\omega)|^2 = \left(\frac{L^4 F_0 \pi}{EI}\right)^2 \left|\sum_{n=1}^{\infty} \frac{\Phi_n'(x)}{(c_n^4 - B_n^4(\omega))}\right|^2. \tag{79}$$

The power spectrum of cantilever tip-angle due to a tip force is shown in Fig. 18 (right) along with the spectra for modes one and two.

The integral in Eqs. (71) and (73) decreases with mode number, see Fig. 16 (right). This indicates that a uniformly applied driving force will distribute less energy to higher modes than a driving force at the tip. It should be noted that the frequency dependence of each mode is the same for all power spectra derived here. The only difference is the relative magnitudes of the resonant peaks as a result of the actuation technique.

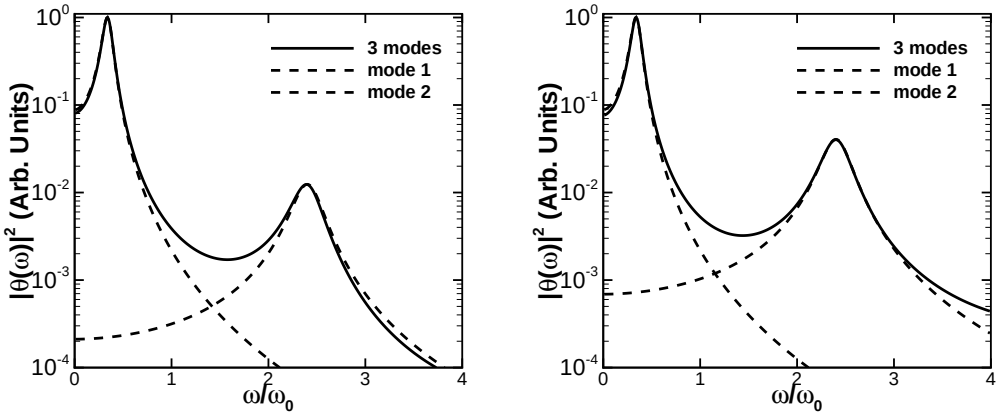

Figure 18: Analytical predictions of the tip-angle power spectrum for a uniformly distributed force (left) and a force localized at the tip (right). The applied forces vary sinusoidally in time. The spectra are calculated using infinite cylinder approximations for three modes (solid) and modes 1 and 2 individually (dashed).

These expressions for the noise and power spectra are accurate when the flow around a cantilever can be assumed two-dimensional. In some cases this assumption can not be made, such as when the geometry is complex or the beam is not long and thin. For these cases it is necessary to calculate the complete three-dimensional flow. Numerical simulations of the cantilever in fluid can quantify the full fluid-structure interaction for any cantilever geometry. Also, results can be calculated for any dynamical variable of interest in experiments. An overview of the numerical approach used in calculating the spectra of thermally and externally driven oscillations follows.

2.4 Complete Cantilever Dynamics: Numerical Simulations

The approximate solution for a cantilever in viscous fluid as an infinite oscillating cylinder is a powerful one. It has been shown to accurately model the noise spectrum for a rectangular cantilever [59]. For some cases, however, it is necessary to account for the three-dimensional nature of fluid flow over a cantilever. In these instances the cantilever dynamics can be quantified using numerical simulations. Numerical simulations also have the ability to calculate deterministic dynamics for any actuation. The spectrum of thermally induced cantilever fluctuations can be calculated using linear response theory and the fluctuation-dissipation theorem. In addition, the power spectrum of externally driven cantilever oscillations can be calculated from the response to an impulse force.

2.4.1 Thermally Driven Cantilever Fluctuations

As discussed earlier, the fluctuation-dissipation theorem relates the stochastic equilibrium fluctuations of a cantilever in fluid to the fluid dissipation. Using linear response theory and the thermodynamic approach based on the fluctuation-dissipation theorem, the autocorrelation of equilibrium fluctuations

is related to the response of the cantilever to the removal of a step force or torque for tip-deflection or tip-angle respectively, see Section 2.2.

The step force must be applied at the cantilever tip in order to satisfy equipartition of energy. A uniform step force will result in the integral of the mode shape appearing in the expression, which does not show up in Eq. (59). Therefore, the cantilever tip-deflection or tip-angle autocorrelation can be determined by computing the corresponding ringdown and substituting into Eq. (10) or (12), respectively. The noise spectra of fluctuations in cantilever tip-deflection and tip-angle can the be obtained using Eqs. (13) and (14).

2.4.2 Externally Driven Cantilever Fluctuations

For the case of an externally driven cantilever the spectrum can be calculated from numerical simulations of the response to an impulse force [69]. By simulating the cantilever response to the particular impulse force of interest the power spectrum can be calculated for any actuation. The impulse that corresponds to a tip localized driving force is,

$$\hat{F}_D = F_0 \pi \delta(x-1). \tag{80}$$

Substituting this force into Eq. (41) gives,

$$\hat{U}_n(x|\omega) = \frac{L^4 F_0 \pi \Phi_n(x)}{EI(c_n^4 - B^4(\omega))} \tag{81}$$

Calculating the modulus squared of Eq. (81) and simplifying yields the same result shown in Eq. (76) and is the desired result for the power spectrum. The power spectrum of externally driven oscillations in cantilever tip-deflection and tip-angle are,

$$|U(\omega)|^2 = \hat{U}_I(\omega)\hat{U}_I^*(\omega), \tag{82}$$

$$|\Theta(\omega)|^2 = \hat{\Theta}_I(\omega)\hat{\Theta}_I^*(\omega). \tag{83}$$

In the above expressions $\hat{U}_I$ and $\hat{\Theta}_I$ are the Fourier transform of the tip-deflection and tip-angle impulse response, respectively. In this notation the * indicates the complex conjugate. Numerical simulations are capable of simulating the impulse response due to any actuation and for any measured variable. Eq. (82) and (83) are the spectra obtained in experiment when the tip-deflection or tip-angle are measured in response to an external drive mechanism. Alternatively, the power spectrum can be obtained by actuating the cantilever with a sinusoidally fluctuating force. However, this approach is computationally prohibitive as it requires a long-time simulation to be run for each frequency.

3 Cantilever Tip-Deflection and Tip-Angle Formulations

3.1 Chapter Overview

Microscopic cantilevers are a popular experimental tool for probing surface properties [3], topography [50], and individual molecules [63]. The first methods employed to measure the motion of a microscale cantilever were the scanning tunneling microscope [11] and optical interferometry [37]. A scanning tunneling microscope measures the tunneling current and calculates the cantilever tip-deflection. Piezoelectric measurement is another experimental method that calculates the tip-deflection. Optical interferometry measures the angle of the cantilever tip. The tip-deflection and tip-angle are fundamentally different dynamical variables. In order to use a measurement technique effectively it is necessary to understand how the cantilever dynamics depend upon the quantity measured.

A description of the dynamics of a cantilever are described by the Euler-Bernoulli beam equation, see Eq. (17). Analysis of this equation will shed insight on the dynamics of different dynamical variables. Tip-deflection and tip-angle are of particular interest, however various other measurable quantities can be studied using a similar approach. The variation between the dynamics of cantilever tip-angle and tip-deflection can be described by analyzing the steady response of a cantilever to a tip-force or tip-torque and carrying out a modal expansion. The results are directly applicable to experiments and indicate the differences that will be observed by changing which quantity is measured. Many of the results discussed in Chapter 3 have been published in the *Journal of Applied Physics* [26].

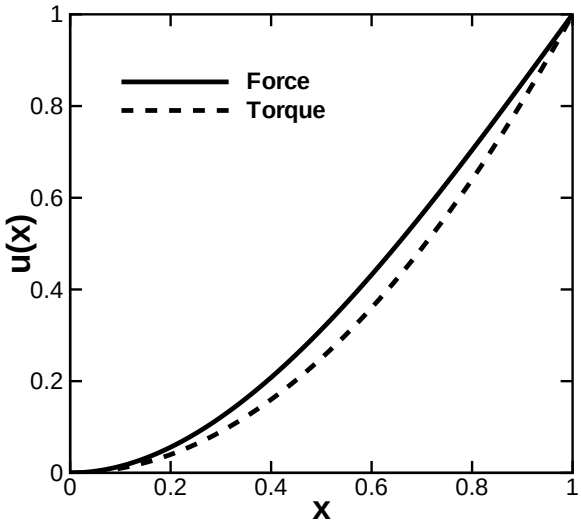

Figure 19: The normalized transverse beam deflection U as a function of x for an applied force (solid) and applied torque (dashed) at the cantilever tip.

3.2 Cantilever Response: Tip-Force and Tip-Torque

In order to describe the inherent differences for fluctuations in cantilever tip-deflection and tip-angle it is necessary to describe the deterministic motion of a cantilever in vacuum. For small deflections, uniform cross-section, and homogenous material properties the deterministic dynamics of a beam in one dimension are described by the Euler-Bernoulli beam equation, Eq. (17). This equation and appropriate boundary conditions can be used to describe the one dimensional flexural deflection of a beam. For the case of steady displacement of a beam in vacuum this equation can be simplified by eliminating the temporal derivative and the forcing terms. The resulting equation is,

$$EI\frac{d^4U(x)}{dx^4} = 0. \tag{84}$$

This equation can be solved directly by integration to yield,

$$U(x) = \frac{M_1}{6}x^3 + \frac{M_2}{2}x^2 + M_3x + M_4. \tag{85}$$

Here the M_i are arbitrary constants and are determined from the boundary conditions. This is the general solution for the steady deflection of any beam in the absence of external body forces. For the case of a cantilevered beam one end of the beam is fixed, which is described by the boundary conditions $U(0) = U'(0) = 0$. These conditions give the result that the constants $M_3 = M_4 = 0$.

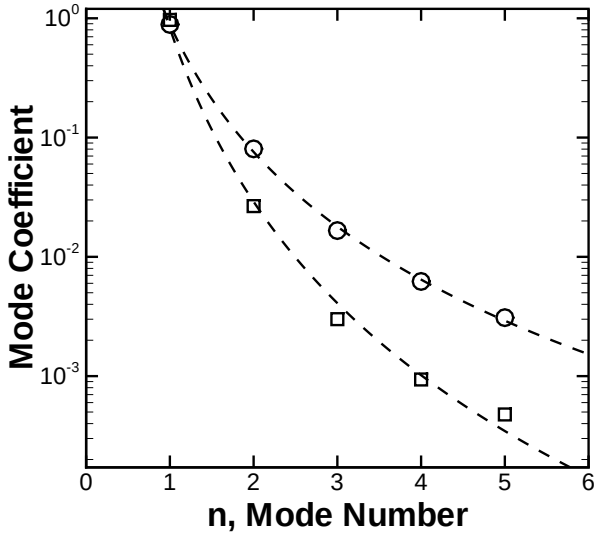

Figure 20: A log-linear plot of the magnitudes of the first five mode coefficients for a uniform cross-section beam. The squares are the coefficients for an applied tip-force, where the dashed line is a power law fit, $a_n = 0.827n^{-4.83}$. The circles are the coefficients for an applied tip-torque, where the dashed line is a power law fit, $a_n = 0.887n^{-3.56}$.

The displacement of a cantilevered beam due to a point force of magnitude F_0 applied at the tip is calculated using the boundary conditions for a shear applied at the free end,

$$U''(1) = 0, \tag{86}$$

$$U'''(1) = \frac{F_0}{EI}. \tag{87}$$

a_n	Force	Torque
$n = 1$	0.9707	0.8908
$n = 2$	-0.0247	-0.0788
$n = 3$	0.0032	0.0165
$n = 4$	-0.0008	-0.0060
$n = 5$	0.0003	0.0028

Table 5: Mode coefficients for an applied force or an applied torque at the tip of a rectangular cantilever.

Using these boundary conditions the displacement is,

$$U(x) = \frac{F_0 L^3}{2EI}\left(\frac{x^3}{3} - x^2\right), \quad 0 \leq x \leq 1. \tag{88}$$

The displacement of a cantilever due to a torque applied at the tip with magnitude τ_0 is calculated using the following boundary conditions,

$$U''(1) = \frac{\tau_0}{EI}, \tag{89}$$

$$U'''(1) = 0. \tag{90}$$

The displacement of the cantilever due to a point torque is,

$$U_\tau(x) = \frac{\tau_0 L^2}{2EI}x^2, \quad 0 \leq x \leq 1. \tag{91}$$

It is straightforward to obtain the angle of the cantilever from the displacement using $\tan\Theta(x) = U'_\tau(x)$. The displacement for the torque-angle formulation is quadratic in space in contrast to the cubic form obtained for the force-deflection formulation. The two displacements are plotted in Fig. 19 and it is apparent that they yield different results. In order to quantify the differences between these two cases, the contributions from each mode of the beam must be calculated.

e_n	Force	Torque
$n = 1$	0.97068	0.61308
$n = 2$	0.02472	0.18830
$n = 3$	0.00315	0.06473
$n = 4$	0.00082	0.03309
$n = 5$	0.00030	0.02669

Table 6: Energy ratios for each mode of a rectangular cantilever for an applied force or an applied torque at the tip.

3.3 Modal Energy Distribution

Using the cantilever modes found in Section 2.3.1 it is possible to decompose the steady deflection of the beam due to a tip-torque or a tip-force into individual mode contributions. The steady displacement due to a force applied at the cantilever tip is the superposition of all modes with appropriate modal coefficients a_n,

$$U(x) = \sum_{n=1}^{\infty} a_n \Phi_n(x). \tag{92}$$

Note that in this equation x refers to the normalized distance along the length of the beam. The modal coefficients are calculated using orthogonality of the mode shapes. Multiplying both sides by $\Phi_m(x)$ and integrating over the length of the beam results in,

$$\int_0^1 U(x)\Phi_m(x)\ dx = \sum_{n=1}^{\infty} a_n \int_0^1 \Phi_n(x)\Phi_m(x)\ dx. \tag{93}$$

The integral on the right side of Eq. (93) is only non-zero when $n = m$. Solving for the modal coefficients yields,

$$a_n = \frac{\int_0^1 U(x)\Phi_n(x)\ dx}{\int_0^1 \left(\Phi_n(x)\right)^2\ dx}. \tag{94}$$

The modal coefficients for the case of an applied tip-torque can be calculated in a similar manner. The mode coefficients are shown in Table 5 for mode

shapes and cantilever deflection with tip values of unity. The magnitudes of these coefficients are shown in Fig. 20 for the $n \leq 5$. The mode coefficients derived here for the deflection of a rectangular cantilever are consistent with those presented in the literature [52].

The first mode and all other odd modes have tip-deflections and angles in the same direction as the bulk beam deflection. It is for this reason that coefficients of even modes have negative signs. Adding the absolute values of the coefficients gives the total beam displacement, so the magnitude of the coefficients quantify the relative magnitude of deterministic oscillations in each mode. For the case of a force applied at the cantilever tip the coefficients relate the bulk spring constant to the dynamic spring constant for each mode,

$$k_n = \frac{k}{|a_n|}. \tag{95}$$

Here $k = 3EI/L^3$ is the bulk spring constant of the cantilever [49]. The motion of the whole cantilever is the sum of contributions from all modes, therefore the displacement of the tip is,

$$U(1) = \sum_{n=1}^{\infty} U_n(1). \tag{96}$$

The displacement of the cantilever tip for each mode is related to the spring constant of each mode by $U_n(L) = F_0/k_n$. Therefore the bulk cantilever spring constant is related to the modal stiffnesses by,

$$\frac{1}{k} = \sum_{n=1}^{\infty} \frac{1}{k_n}. \tag{97}$$

The fluctuation-dissipation theorem and linear response theory show that the deterministic oscillations are directly related to the stochastic fluctuations. Therefore the mode coefficients shown in Table 5 indicate the relative magnitudes of stochastic fluctuations in the corresponding dynamic variable.

Another way of looking at the modes is to examine how much energy is distributed to each mode. This is accomplished by calculating the total energy of the deflected beam for an applied force,

$$E_t = \frac{EI}{2L} \int_0^1 \left(U''(x)\right)^2 dx, \tag{98}$$

and similarly for an applied torque. The fraction of the total energy in each mode is calculated from the mode shapes and the modal coefficients,

$$e_n = \frac{EI}{2LE_t} \int_0^1 \left(a_n \Phi_n''(x)\right)^2 dx. \tag{99}$$

Values of the energy ratio are shown in Table 6.

For the force-deflection scheme the first mode contributes nearly all of the total cantilever energy. Using the torque-angle scheme the first mode contributes only a little over half of the total motion. This means that tip-angle measurements will distribute 35.8% more energy to higher modes than tip-deflection measurements. In fact, this analysis shows that mode five for the tip-angle formulation will have more energy than mode two for the tip-deflection case. In the realm of experiment this means that stochastic fluctuations in cantilever tip-angle will show larger contributions in modes beyond the first. This variation in modal energy distribution can be used in experiment by measuring tip-deflection or tip-angle in order to minimize or maximize the contributions from higher modes, respectively. Higher order modes have the advantage of lower noise magnitude, which allows the resolution of measurements to be improved [13]. In addition, higher modes are activated at higher frequencies and therefore enable measurements to be taken at even shorter time scales.

4 The Stochastic and Driven Dynamics of a Rectangular Microscopic Cantilever in Fluid

4.1 Chapter Overview

The discussions in the previous chapters model the motion of microscopic cantilevers in fluid. The analytical solutions are based on the assumption that the flow at any point on the cantilever is equivalent to that around a cylinder. This approach neglects three-dimensional flow effects. Using numerical simulations and a thermodynamic approach, the complete three-dimensional fluid-structure interaction can be calculated. Finite element simulations are used here to calculate the cantilever dynamics [38]. This method is applied to describe the dynamics of realistic cantilevers in fluid for thermal and external drive mechanisms. The results are precisely the quantities measured in experiments using microscopic rectangular cantilevers.

4.2 The Stochastic Dynamics of a Rectangular Cantilever in Viscous Fluid

The stochastic dynamics of a cantilever in viscous fluid are quantified using the thermodynamic approach based on the fluctuation-dissipation theorem, see Section 2.4.1. This approach relates stochastic motion to deterministic calculations. The complete deterministic dynamics of a cantilever in fluid are accessible using numerical simulations. This approach calculates the three-dimensional,

	$\langle u_1^2 \rangle^{1/2}$(nm)	$\langle \theta_1^2 \rangle^{1/2}$(rad)
(1)	5.6	5.0×10^{-7}
(2)	20	7.0×10^{-9}

Table 7: The magnitude of stochastic fluctuations in tip-deflection and in tip-angle for the rectangular (1) and V-shaped (2) cantilevers. These values were obtained from numerical simulations simulations of the beams in vacuum.

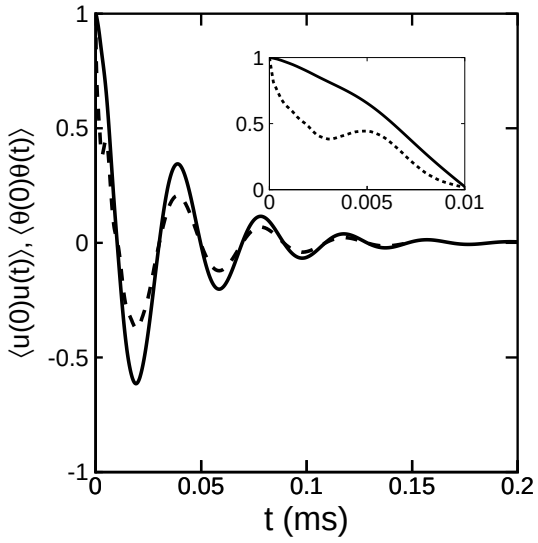

Figure 21: The normalized autocorrelation of the C2 rectangular cantilever for tip-deflection (solid) and tip-angle (dashed). (Inset) A detailed view of the autocorrelation at short time differences to illustrate the influence of higher modes in the tip-angle measurements.

time dependent, fluid-solid interaction problem. Numerical simulations are valid for any geometry or measurement approach. The deterministic numerical simulations use a finite element approach that is described elsewhere [38, 84].

The equilibrium fluctuations in cantilever tip-displacement for a rectangular cantilever in water have been described elsewhere [22, 25, 59, 60]. In the following these results are compared with the stochastic dynamics as determined by the equilibrium fluctuations of the cantilever tip-angle. Differences observed between the stochastic dynamics of tip-deflection and tip-angle fluctuations indicate fundamental differences relevant to experiment. The rectangular micron scale C2 cantilever is studied. The geometry of this cantilever is given in Table 4.

As discussed in Section 2.2 the autocorrelations in equilibrium fluctuations

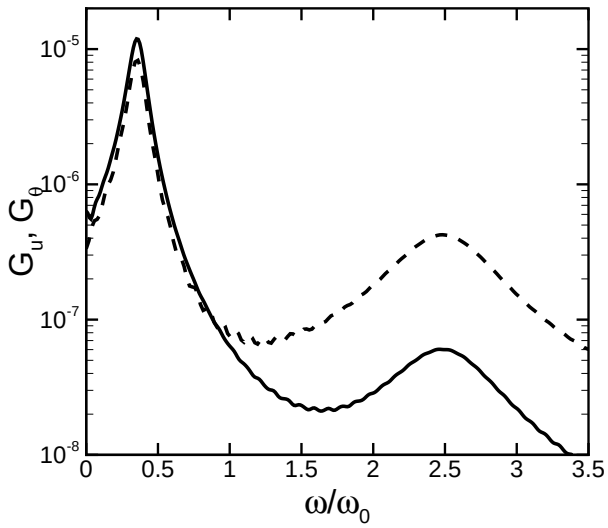

Figure 22: The noise spectra of stochastic fluctuations in cantilever tip-angle (dashed) and tip-deflection (solid) from numerical simulations of the C2 rectangular cantilever. The curves are normalized to have the same area, however only the first two modes are shown.

follow immediately from the ring down of the cantilever due to the removal of a step force (to yield $\langle u(0)u(t)\rangle$) or step point-torque (to yield $\langle\theta(0)\theta(t)\rangle$). The autocorrelations of the rectangular cantilever equilibrium fluctuations are shown in Fig. 21. The magnitude of the noise is quantified by the root mean squared tip-angle and tip-deflection, which are listed in Table 7.

A comparison of the autocorrelations yields some interesting features. At short times $\langle\theta(0)\theta(t)\rangle$ shows the presence of higher harmonic contributions. This is shown more clearly in the inset of Fig. 21. This illustrates that the autocorrelation of equilibrium cantilever tip-angle fluctuations are more sensitive to higher mode dynamics.

The real part of the Fourier transform of the autocorrelations yield the noise

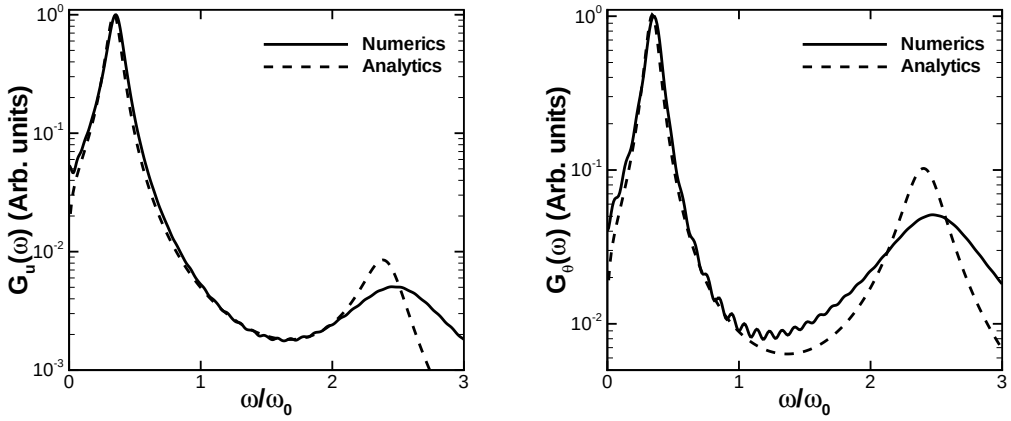

Figure 23: (left) The spectra of thermally driven fluctuations in cantilever tip deflection from numerical simulations (solid) and infinite cylinder theory (dashed) for the C2 rectangular cantilever. (right) The spectra of thermally driven fluctuations in cantilever tip angle from numerical simulations (solid) and infinite cylinder theory (dashed) for the C2 rectangular cantilever.

spectra shown in Fig. 22. The equipartition theorem of energy yields,

$$\frac{1}{2\pi}\int_0^\infty G_u(\omega)d\omega = \frac{k_BT}{k}, \tag{100}$$

$$\frac{1}{2\pi}\int_0^\infty G_\theta(\omega)d\omega = \frac{k_BT}{k_t}, \tag{101}$$

where k and k_t are the transverse and torsional spring constants for the total cantilever motion, respectively. The values of the spring constants for the C2 cantilever are shown in Table 4. The curves in Fig. 22 are normalized to have a total area of unity. Using this normalization the area under a peak is an indication of the amount of energy contained in a particular mode. Fig. 22 shows only the first two modes, although the numerical simulations include all of the modes (within the numerical resolution of the finite element simulation). The energy distribution across the first two modes shows the significance of the second mode for the tip-angle dynamics.

Using a simple harmonic oscillator approximation it is straight forward to

	ω_f/ω_0	Q
(1)	0.35	3.34
(2)	0.36	3.26

Table 8: The peak frequency and quality factor of the fundamental mode of the C2 rectangular cantilever in water determined by finite element simulations using the thermodynamic approach. (1) is computed using the cantilever tip-displacement due to the removal of a step force. (2) is computed using the cantilever tip-angle due to the removal of a point-torque. The frequency result is normalized by the resonant frequency in vacuum ω_0. Using the infinite cylinder approximation with a radius of $w/2$ the analytical predictions are $Q = 3.24$ and $\omega_f/\omega_0 = 0.34$.

compute the peak frequency ω_f and quality factor Q for the cantilever in fluid. Using a single mode approximation yields the values shown in Table 8. As expected there is a significant reduction in the cantilever frequency when compared with the resonant frequency in vacuum ω_0 and the quality factor is quite low because of the strong fluid dissipation. The values of ω_f and Q for tip-angle and tip-dispacement are nearly equal. This is expected since the displacements and angles are very small, resulting in negligible coupling between the modes. Any differences in ω_f and Q are attributed to the use a single mode approximation.

It is useful to compare these results with the commonly used approximation of an oscillating, infinitely long cylinder with radius $w/2$ [59, 69, 74]. The spectra calculated from numerical simulations are shown in Fig. 23(left) and (right) along with infinite cylinder results for the tip-deflection and tip-angle, respectively. Note that the numerical grid spacing and time step limit the resolution of the noise spectrum near the second resonance. The cantilever used has an aspect ratio of $L/w \approx 7$ and the infinite cylinder theory is quite good at predicting ω_f and Q for the fundamental mode.

This discussion quantifies the stochastic dynamics for the force-deflection

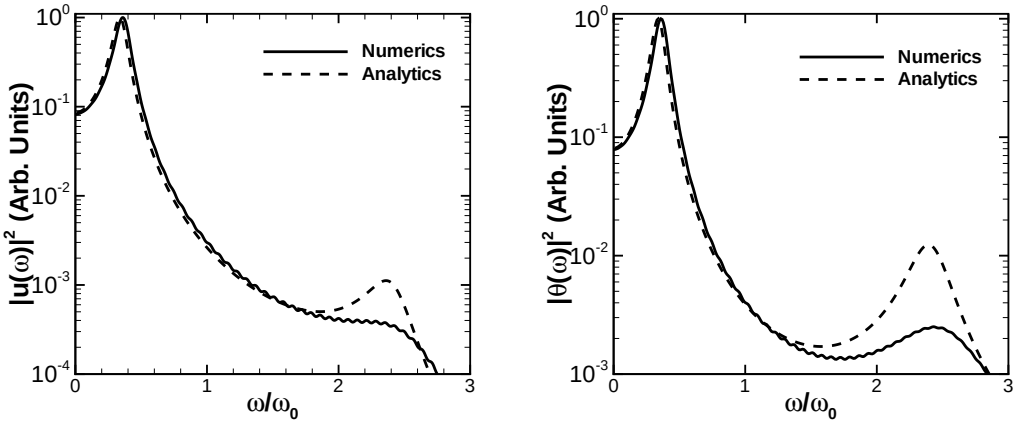

Figure 24: (left) The power spectra of an externally driven cantilever measured using tip-deflection from numerical simulations (solid) and analytical predictions of infinite cylinder theory (dashed) for the C2 cantilever. The cantilever is driven by a force uniformly distributed along the beam length that varies sinusoidally with time. (right) The power spectra of an externally driven cantilever measured using tip-angle from numerical simulations (solid) and analytical predictions ofinfinite cylinder theory (dashed) for the C2 cantilever. The cantilever is driven by a force uniformly distributed along the beam length that varies sinusoidally with time.

and torque-angle schemes. In particular the stochastic dynamics of a rectangular cantilever in fluid are compared for the two cases. The results of numerical simulations indicate that the peak frequency and quality factor are identical for different measured variables. However, the distribution of thermal energy between modes changes depending on the measured variable. This is a result of the different mode activation affected by a tip-torque as opposed to an applied tip-force. Also, approximate analytical expressions for the cantilever as an infinite cylinder accurately predict the peak frequency and quality factor in this case.

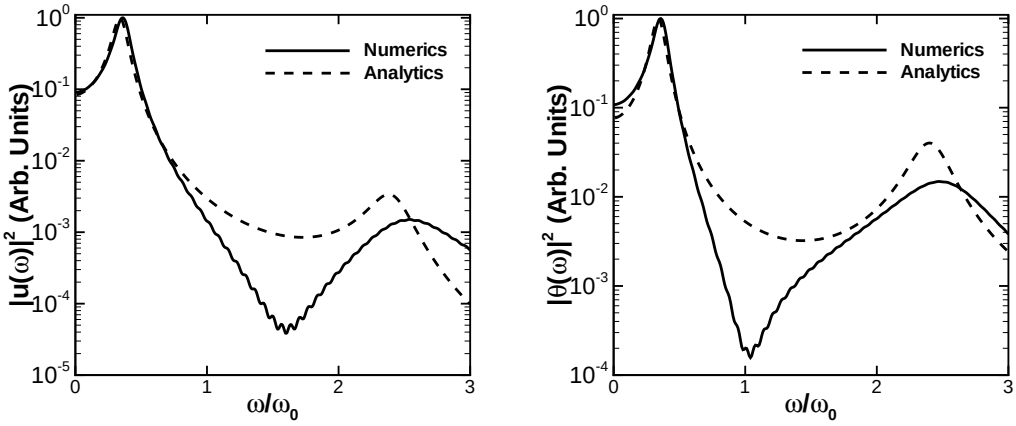

Figure 25: (left) The power spectra of an externally driven cantilever measuring tip-deflection from numerical simulations (solid) and analytical predictions of infinite cylinder theory (dashed) for the C2 cantilever. The cantilever is driven by a force localized at the tip that varies sinusoidally with time. (right) The power spectra of an externally driven cantilever measuring tip-angle from numerical simulations (solid) and analytical predictions of infinite cylinder theory (dashed) for the C2 cantilever. The cantilever is driven by a force localized at the tip that varies sinusoidally with time.

4.3 Ratio of the Driven to Noise Spectra for a Rectangular Cantilever in Fluid

Another physically relevant case is a cantilever actuated by an external mechanism. Numerical simulations are capable of describing the complete fluid-structure dynamics for any actuation method. The driven motion of the C2 cantilever of [69] in viscous fluid is studied. The power spectrum is calculated from the modulus squared of the cantilever response to an impulse force. The impulse response is determined using numerical simulations. The power spectrum for a uniformly distributed driving force is shown for tip-deflection and tip-angle measurements in Fig. 24. The power spectrum for an external driving localized at the cantilever tip is shown in Fig. 25 for tip-deflection and tip-angle

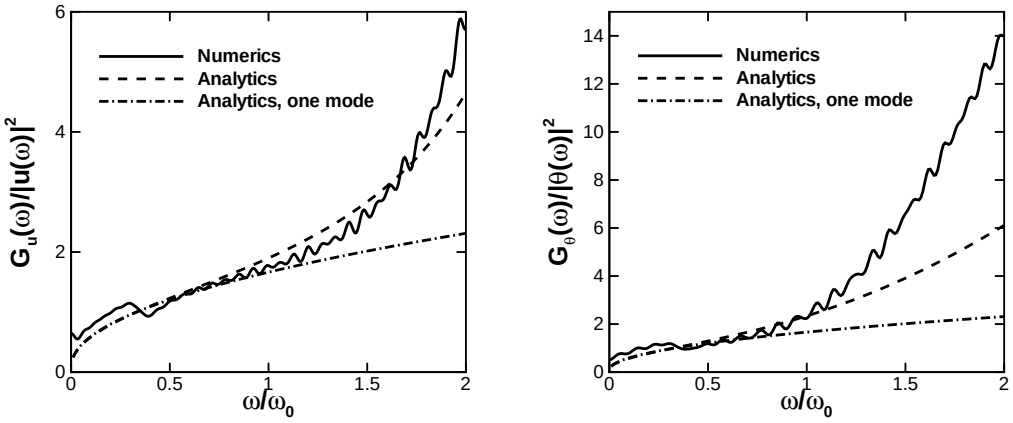

Figure 26: (left) The ratio for C2 of thermally to externally driven fluctuations in cantilever tip deflection from numerical simulations (solid) and infinite cylinder theory for three modes (dashed) and one mode (dash-dot). The noise and power spectrum for multiple modes are those in Eqs. (49) and (72). (right) The ratio for C2 of thermally to externally driven fluctuations in cantilever tip deflection from numerical simulations (solid) and infinite cylinder theory for three modes (dashed) and one mode (dash-dot). The noise and power spectrum for multiple modes are those in Eqs. (64) and (74).

measurements. In all cases the first two modes are shown. Results from numerical simulations have limited temporal and spatial resolution, and so the fluid damping for the second mode is not completely resolved. However, it is evident that the prediction of the spectra using infinite cylinder theory is relatively accurate.

The ratio of the noise to the power spectrum is shown in Fig. 26. The ratio of the noise spectrum to the power spectrum yields the ratio of the magnitude of the Brownian force to the magnitude of the drive forcing. When the magnitude of the drive force is constant for all frequency, the ratio of the noise to power spectrum is directly related to the Brownian force. The ratio of Eq. (58) to

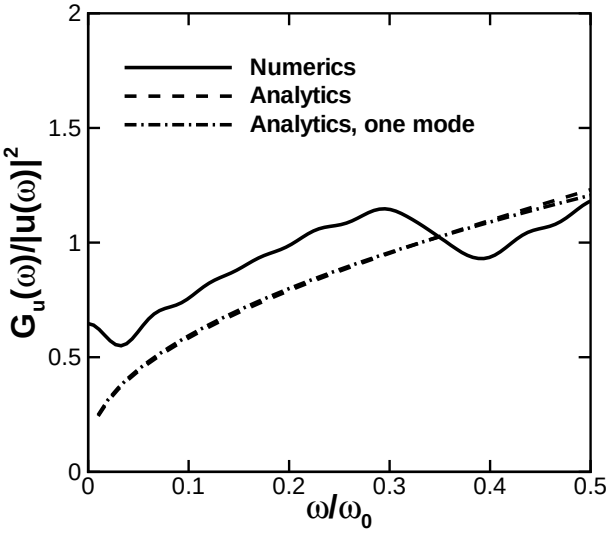

Figure 27: The ratio for C2 of thermally to externally driven fluctuations in cantilever tip-deflection from numerical simulations (solid) and infinite cylinder theory for many modes (dashed) and one mode (dash-dot). The figure focuses on the low frequency behavior of the spectra ratio in Fig. 26.

Eq. (76) yields,

$$\frac{G_u(x|\omega)}{|U_n(x|\omega)|^2} = \frac{4k_BTk_n}{(\omega_n\pi F_0)^2}T_0\omega\Gamma_i(\omega) \propto 4k_BT\gamma_f(\omega). \tag{102}$$

The Fourier transform of the viscous damping is directly linked to the spectral density of the Brownian force, see Eq. (5). In Fig. 26 the ratio of the spectra for three infinite cylinder modes is shown along with the single mode result. It is evident that the Brownian forcing varies with mode and it is necessary to incorporate all modes in order to accurately predict the frequency dependence. These plots also compare the multiple mode spectra ratio for infinite cylinder theory and numerical simulations. It is evident that, for this choice of cantilever, infinite cylinder theory accurately predicts the frequency dependence of the spectra.

A further consideration to investigate is the low frequency behavior of the

spectra ratio, and therefore the viscous damping. A detailed view of the low frequency spectra ratio is shown in Fig. 27. Infinite cylinder theory neglects the nonlinear convective inertia term in the Naviar-Stokes equation. For this unsteady Stokes flow, the viscous boundary layer grows inversely with frequency, growing to infinity as the frequency goes to zero. This means at low frequencies the viscous damping approaches zero and the resulting flow from the cantilever motion propagates everywhere into the surrounding fluid. This is known as the Stokes paradox [58]. It comes about in the low frequency regime because the assumption that convective inertia is negligible becomes invalid. The numerical simulations account for this inertia term, and therefore the fluid damping approaches a finite value for this data.

This section has shown that for long and slender rectangular cantilevers the frequency dependence of the noise and power spectra, and the ratio of the spectra, can be calculated using infinite cylinder approximations. It is necessary to investigate the manner in which Brownian forcing and externally driven motion vary for complex geometries and novel actuation techniques.

5 The Stochastic and Driven Dynamics of V-shaped Cantilevers in Fluid

5.1 Chapter Overview

Approximate analytical expressions describe the noise and power spectra for cantilevers in fluid where three-dimensional flows are negligible. The resonance peak width and location for a cantilever in fluid are well predicted by the infinite cylinder model under these circumstances. However, the accuracy of this model is unknown for the case of cantilevers with complex three-dimensional geometries. The dynamics of microscopic V-shaped cantilevers are of particular interest for experiments [3].

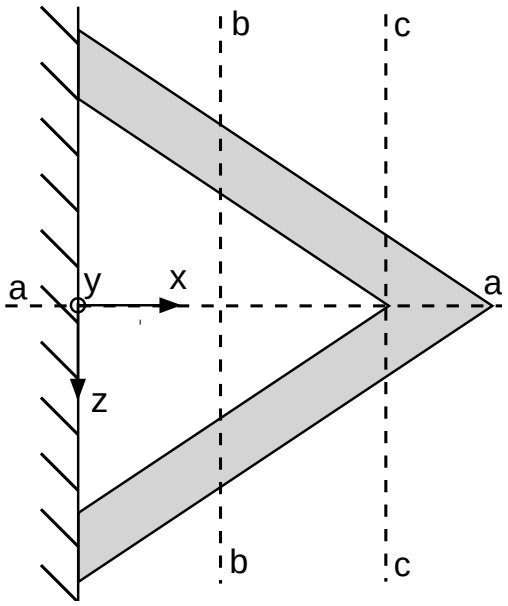

Figure 28: A schematic of the V-shaped cantilever showing the cross-sections studied. Section $a - a$ is located at $z = 0$, $b - b$ is located at $x = 77\mu$m, and $c - c$ is located at $x = 108.8\mu$m.

This chapter explores the stochastic and driven dynamics of V-shaped cantilevers in fluid. An integral component of any theoretical model is an analytical

description of the resulting fluid flow field caused by the oscillating cantilever. The fluctuation-dissipation theorem allows for the stochastic dynamics of the fluid and cantilever to be described by deterministic calculations. The deterministic finite element simulations performed yield a quantitative picture of the resulting fluid dynamics. Exploring the flow fields further yields insight into the dominant features that contribute to the cantilever dynamics.

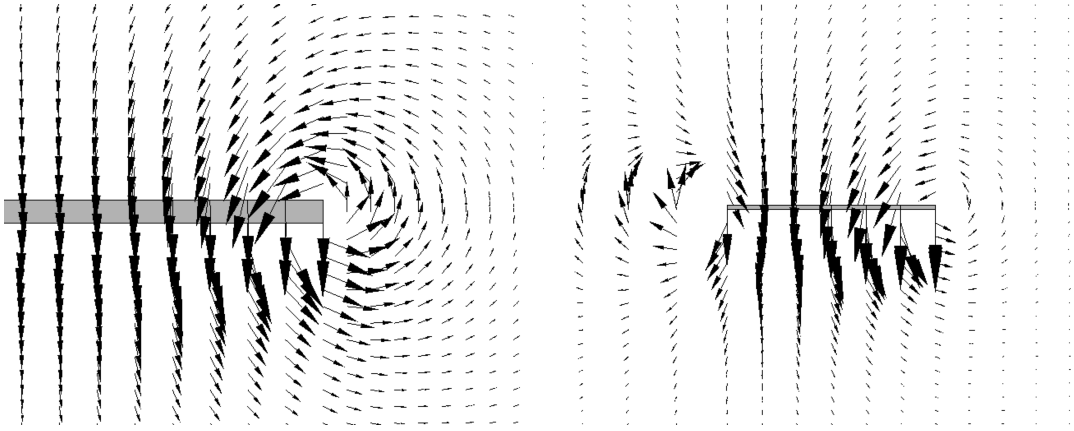

Figure 29: The fluid flow near the tip of the cantilever as illustrated by the velocity vector field calculated from finite element numerical simulations. A cross section of the $x-y$ plane at $z=0$ is shown (see Fig. 12) that is a close-up view of the tip-region. The shaded region indicates the cantilever (because of the small deflections used in the simulations that cantilever does not appear to be deflected). (left) The flow field near the tip of the rectangular cantilever. This flow field is at t=6μs and the magnitude of the largest velocity vector shown is -0.3 nm/s. (right) The flow field near the tip of the V-shaped cantilever, cross-section $a-a$ in Fig. 28. This flow field is at t=7.2μs and the magnitude of the largest velocity vector shown is -26 nm/s. The shaded region indicates the tip region where the two single arms have merged. The open region to the left is where the two single arms have separated revealing the open region in the interior of the V-shaped cantilever.

5.2 The Dynamics of the Veeco V-shaped Cantilever in Fluid

As discussed earlier, for long and slender rectangular cantilevers the flow field is often approximated by that of a cylinder of diameter w undergoing

transverse oscillations. This approach assumes that the fluid flow is essentially two-dimensional in the $y-z$ plane and neglects any flow over the tip of the cantilever. The flow field around a rectangular cantilever is compared to that around the V-shaped MLCT Type E microlever from Veeco [76]. The convention used for the geometry is shown in Fig. 12, and the geometry is given in Table 4. This particular cantilever is of interest in experiments that use the Brownian driven cantilever motion to investigate the dynamics of molecules [23].

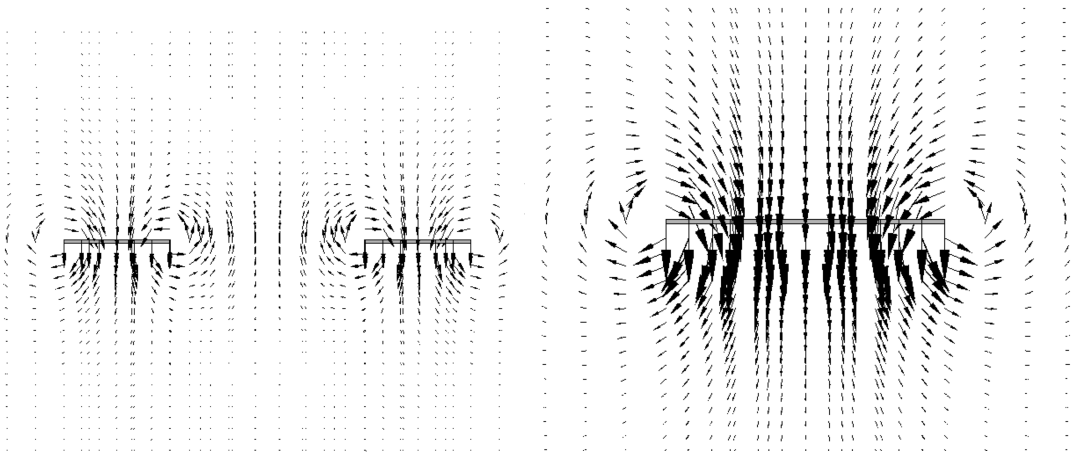

Figure 30: The fluid velocity vector field at two axial positions along the Veeco V-shaped cantilever calculated from deterministic finite element numerical simulations. Cross sections of the $y-z$ plane are shown (see Fig. 12), the entire simulation domain is not shown and the shaded region indicates the cantilever. Both images are taken at t=7.2μs and the maximum velocity vector shown is -26 nm/s. (left) The $y-z$ plane at $x = 77\mu$m, cross-section $b-b$ in Fig. 28. The skewed width of a single arm of the cantilever in this cross-section is 18μm. The distance separating the two cantilever arms is 36μm. (right) The $y-z$ plane at $x = 108.8\mu$m. , cross-section $c-c$ in Fig. 28 This is the point at which the two single arms join to make a continuous cross-section of width $2w$.

Figure 29 (left) illustrates the tip flow for the C2 rectangular cantilever using vectors of the fluid velocity in the $x-y$ plane at $z = 0$. The figure is a close-up view near the tip of the cantilever. It is evident that the flow over the rectangular cantilever is nearly uniform in the axial direction leading up to the

tip. However, near the tip there is a significant tip flow that decays rapidly in the axial direction away from the tip. The increasing significance of the tip flow as the cantilever geometry becomes shorter (for example, by simply decreasing L) is not certain and remains an interesting open question [79]. However, for the geometry used here it is clear that this tip-flow is negligible based upon the accuracy of the analytical predictions using the two-dimensional model.

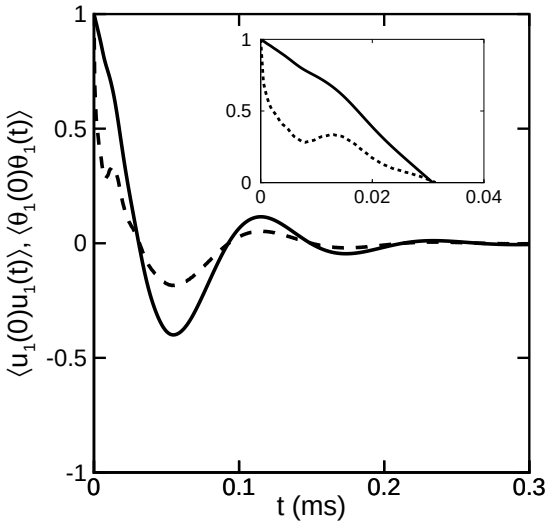

Figure 31: The normalized autocorrelation of equilibrium fluctuations in the tip-deflection $\langle u_1(0)u_1(t)\rangle$ (solid lined) and in tip-angle $\langle \theta_1(0)\theta_1(t)\rangle$ (dashed-line) for the Veeco V-shaped cantilever. The inset shows a close-up of the dynamics for short time differences to illustrate the influence of the higher modes in the tip-angle measurements.

For cantilevers with non-uniform cross-section the assumptions of infinite cylinder theory are not valid. However, it is interesting to investigate the accuracy of this model for more complex geometries in order to test its validity. As for the rectangular cantilever, the fluid flow around the Veeco V-shaped cantilever is calculated using a three-dimensional finite element simulation [23].

Figure 29 (right) illustrates the tip flow for the Veeco V-shaped cantilever, again by showing velocity vectors in the $x - y$ plane at $z = 0$. The shaded region indicates the part of the cantilever where the two arms have merged. To the right of the shaded region illustrates flow off the tip and to the left indicates flow that circulates back in between the two individual arms.

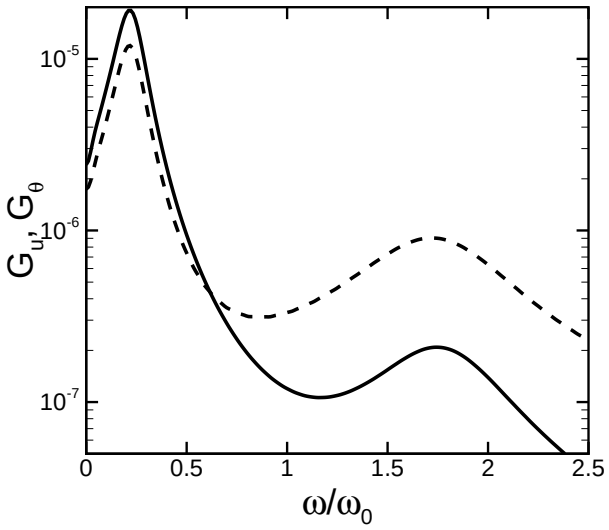

Figure 32: The noise spectra for the Veeco V-shaped cantilever as determined from the tip-displacement G_u (solid line) and from tip-angle G_θ (dashed line). The curves are normalized to have an area of unity, with only the first two modes shown.

In order to illustrate the three-dimensional nature of this flow, the flow field in the $y-z$ plane is shown at two axial locations in Fig. 30. Figure 30(left) is at axial location $x = 77\mu$m. The two shaded regions indicate the two arms of the cantilever. Each arm is generating a flow with a viscous boundary layer (Stokes layer) as expected from previous work on rectangular cantilevers. However, the Stokes layers interact in a complicated manner near the center. It is expected that as one goes from the base of the cantilever to the tip that these fluid

structures would transition from non-interacting to strongly-interacting.

Figure 30(right) illustrates the flow field at axial location $x = 108.8\mu$m, the axial location at which the two arms of the cantilever merge to form the tip region. The length of the shaded region is therefore 36μm or twice that of a single arm shown in Fig. 30(left). For this tip region the flow field is similar to what would be expected of a single rectangular cantilever of this width.

	ω_f/ω_0	Q
(1)	0.21	1.98
(2)	0.22	2.04
$(L, 2w, h)$	0.19	1.98

Table 9: The peak frequency and quality factor of the fundamental mode of the V-shaped cantilever determined by finite element simulations using the thermodynamic approach. (1) is computed using the cantilever tip-displacement due to the removal of a step force. (2) is computed using the cantilever tip-angle due to the removal of a point-torque. The third line represents theoretical predictions using the geometry of an equivalent rectangular beam given by $(L, 2w, h)$. The frequency result is normalized by the resonant frequency in vacuum ω_0.

Overall, it is clear that the fluid flow field is more complex for a V-shaped cantilever than for the long and slender rectangular beam. For a V-shaped cantilever the flow is three-dimensional near the tip region where the two arms join together. Therefore changes in the width of a V-shaped cantilever legs will affect the quality factor and peak frequency [9].

Central to the flow field dynamics are the interactions of the two Stokes layers caused by the oscillating cantilever arms. The thickness of these Stokes layers are expected to scale with the frequency of oscillation as $\delta_s/r \sim R^{-1/2}$ where r is the half-width of the cantilever and $R = \omega r^2/\nu_f$ is a frequency based Reynolds number (often called the frequency parameter). For the relevant case of a cylinder of radius r oscillating at frequency ω the solution to the unsteady

Stokes equations yields a distance of approximately $5\delta_s$ to capture 99% of the fluid velocity in the viscous boundary layer [20]. For a single arm of the V-shaped cantilever this distance is nearly 10μm. In comparison, the total distance between the two arms at the base is 125μm. This separation is large enough such that the two Stokes layers have negligible interactions near the base. However, as the arms approach one another with axial distance the Stokes layers overlap and eventually merge at the tip. In addition, the velocity of the cantilever and therefore the surrounding fluid increases with distance along the beam. So as the two viscous boundary layers interact, the magnitude of the velocity is increasing. This region of moderate to strong interaction is therefore dominating the fluid damping and mass loading.

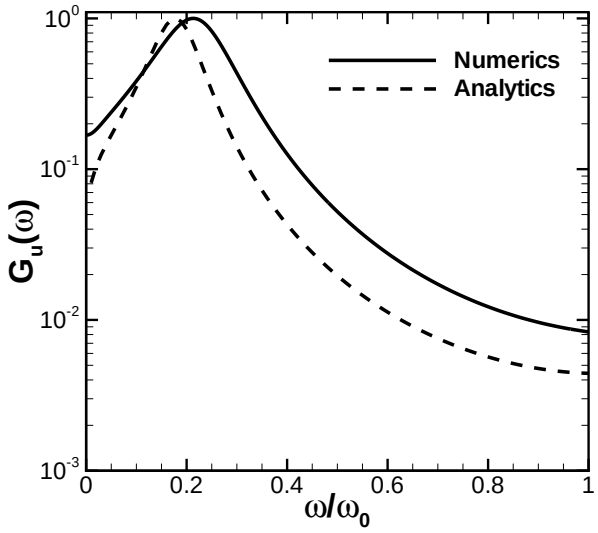

Figure 33: The noise spectrum of tip-deflection for the Veeco V-shaped cantilever as determined from numerical simulations and infinite cylinder approximations. It is evident that the approximate analytics can predict the peak location and width. However considerable variation is seen for the frequency dependence of the spectrum.

5.2.1 The Stochastic Dynamics of the Veeco V-shaped Cantilever in Fluid

Despite the complicated interactions of the three-dimensional flow caused by the cantilever tip and the axial merging of the two Stokes layers, a V-shaped cantilever behaves as a damped simple harmonic oscillator. The autocorrelations in tip-angle and tip-displacement that are found using full finite element numerical simulations are shown in Fig. 31. It is again clear that the tip-angle dynamics have significant contributions from the higher modes, see the inset of Fig. 31. The area normalized noise spectra are shown in Fig. 32. Here again it is evident that more energy is distributed to higher modes for the torque-angle formulation.

Using a simple harmonic oscillator analogy a peak frequency and a quality factor can be determined from the first mode in the noise spectra of Fig. 32. These values are given in the first two rows of Table 9. The quality factor of the fundamental cantilever resonance is $Q \approx 2$ and the peak frequency is reduced significantly, $\omega_f/\omega_0 \approx 0.2$, compared to the resonant frequency in the absence of a surrounding viscous fluid.

L'/L	w'/w	h/h'
0.8	1.9	0.8

Table 10: The geometry of the equivalent rectangular beam that yields the exact values of k, ω_f, and Q for the V-shaped cantilever that have been determined from full finite-element numerical simulations. The length, width, and height of the equivalent beam (L', w', h') are calculated using Eqs. (103)-(104) and are normalized by the values of (L, w, h) for the V-shaped cantilever given in Table 4.

It is insightful and of practical use to determine the geometry of the equivalent rectangular beam that would yield the precise values of k, ω_f, and Q

calculated for the fundamental mode of the V-shaped cantilever from full finite-element numerical simulations. For the rectangular beam the equations are well known (c.f. Ref. [59]) and yield a unique value of length L', width w', and height h' as shown below,

$$k = \frac{3EI}{L'^3} = \frac{Ew'h'^3}{4L'^3}, \tag{103}$$

$$Q = \frac{m_f\omega_f}{\gamma_f} = \frac{\frac{4\rho_c h'}{\pi\rho_f w'} + \Gamma_r(w', \omega_f)}{\Gamma_i(w', \omega_f)}, \tag{104}$$

where the peak frequency in fluid ω_f is determined from the maximum of the noise spectrum of the first mode,

$$G_u = \frac{4k_BT}{k}\frac{1}{\omega_0} \times \frac{T_0\tilde{\omega}\Gamma_i(R_0\tilde{\omega})}{[(1-\tilde{\omega}^2(1+T_0\Gamma_r(R_0\tilde{\omega})))^2 + (\tilde{\omega}^2T_0\Gamma_i(R_0\tilde{\omega}))^2]}. \tag{105}$$

In the above equations $\tilde{\omega} = \omega/\omega_0$ is the normalized frequency, m_f is the equivalent mass of the cantilever plus the added fluid mass, γ_f is the fluid damping, Γ is the hydrodynamic function for an infinite cylinder, Γ_r is the real part of Γ, and Γ_i is the imaginary part of Γ. Equations (103) and (104) can be solved to yield values for the unknown geometry of the equivalent rectangular beam L', w', and h' which are given in Table 10. The equivalent beam is shorter, thinner, and wider than the V-shaped cantilever. Importantly, the width of the equivalent beam is nearly twice that of a single arm of the V-shaped cantilever.

These results suggest that the parallel beam approximation (PBA) [2, 68, 70, 17] commonly used to determine the spring constant for a V-shaped cantilever may also provide a useful geometry for determining the dynamics of V-shaped cantilevers in fluid. In this approximation the V-shaped cantilever is replaced by an equivalent rectangular beam of length L, width $2w$, and height h to yield a simple analytical expression for the spring constant. This has been shown

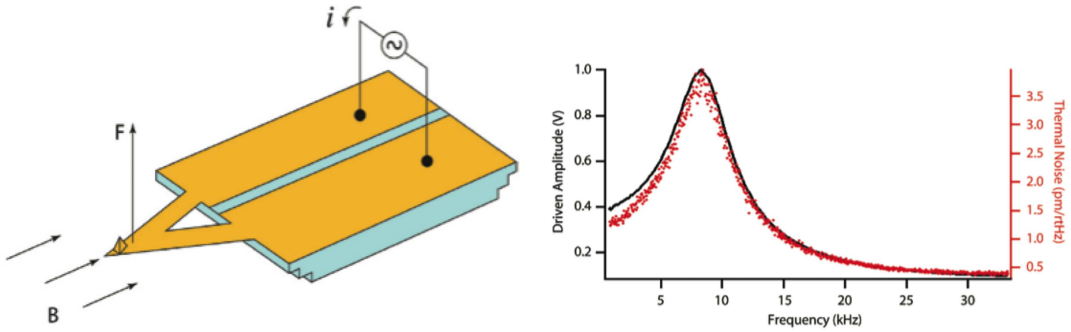

Figure 34: (left) A schematic of the iDrive actuation approach applied to a V-shaped microscopy cantilever. (right) A comparison of the experimentally measured thermally and externally driven spectra. The schematic and comparison come from the iDrive information sheet, Asylum Research [6].

to be quite successful for V-shaped cantilevers that have arms that are not significantly skewed. The results of using the geometry of this approximation to determine ω_f and Q from the two-dimensional cylinder approximation are shown on the third row of Table 9. It is clear that the predicted peak frequency and quality factor are quite accurate. However, the noise spectrum predicted by the two-dimensional approximations exhibits substantial error, see Fig. 33. It is expected that the results for the peak parameters will remain useful for cantilever geometries that do not deviate significantly from that of an equilateral triangle as studied here. An exploration of the breakdown of this approximation is possible using the methods described but is beyond the scope of the current efforts.

The fluid dynamics generated by the motion of a V-shaped cantilever in fluid are more complex than those for a rectangular cantilever. However, the stochastic dynamics of a V-shaped cantilever can be approximated by those of an infinite cylinder with the appropriate width. Another experimentally relevant consideration is the dynamics of a cantilever driven by an external mechanism.

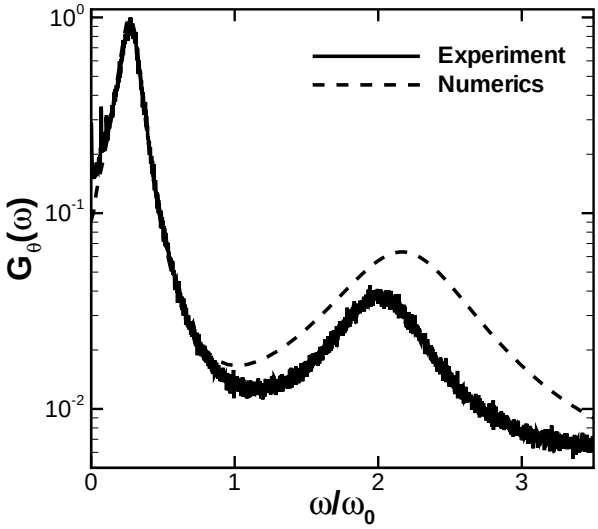

Figure 35: The spectra of thermally driven fluctuations in cantilever tip-angle from experiment (solid) and numerical simulations (dashed) for the Olympus V-shaped cantilever. Experimental measurements are from Asylum Research, to be published [27].

5.3 Comparing the Driven and Noise Spectra for the V-shaped Olympus Cantilever

Recent experiments use the Olympus V-shaped microcantilever with a novel iDrive actuation technique [6, 56]. The geometry of the Olympus V-shaped cantilever is given in Table 4. The iDrive approach uses an applied magnetic field and current flowing through the cantilever in order to generate a distributed driving force as shown in Fig. 34(left). Here results from experiments involving this cantilever and actuation are compared with results from numerical simulations. The noise spectrum of stochastic fluctuations in cantilever tip-angle is shown in Fig. 35 for these cases. The two yield nearly identical results for low frequency up to the beginning of the second mode peak as seen in Fig. 34(right). Some discrepancy is expected, as the numerical simulation treats the cantilever

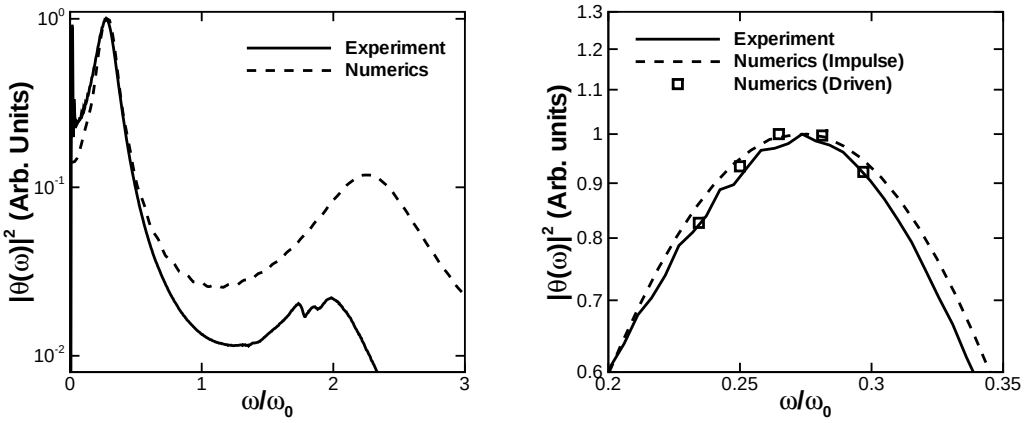

Figure 36: (left) The power spectrum for the Olympus V-shaped cantilever tip-angle driven by the iDrive activation technique from experiment (solid) and numerical simulations (dashed). (right) The power spectrum in the vicinity of the first resonance peak for experiment (solid), numerical simulations of the iDrive impulse response (dashed), and simulations where the cantilever is driven by a sinusoidal iDrive force (squares). Experimental measurements are from Asylum Research, to be published [27].

as a solid silicon nitride cantilever while the physical cantilever is likely plated and contains electrical components. Also, the limited resolution in the simulation does not completely quantify the fluid-structure interaction for the second mode.

A similar comparison is seen for the power spectrum of the V-shaped cantilever using an iDrive actuation, see Fig 36(left). The power spectrum from numerics in this figure is calculated using an impulse force spatially distributed in the manner of the iDrive technique. As with the noise spectrum the frequency dependence is consistent up to the second peak. In both cases the second mode peak has a higher magnitude for numerics than experiment. The power spectrum is also calculated using numerical simulations with the cantilever driven at five individual frequencies. This involved applying a sinusoidally varying force

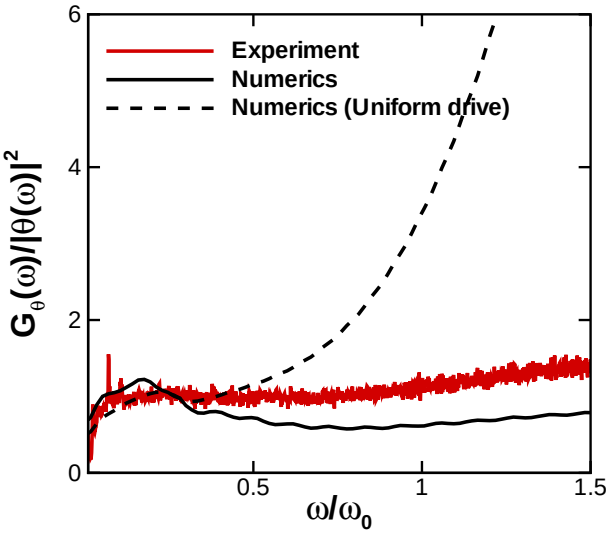

Figure 37: The ratio of fluctuations in Olympus V-shaped cantilever tip-angle for thermal and external driving forces. Results are shown for experiment using the iDrive power spectrum [27] (solid), numerics using the iDrive power spectrum (dashed), and numerics for a uniformly distributed force power spectrum. For the iDrive technique the ratio is nearly constant for moderate frequency, in contrast to the trend predicted by infinite cylinder theory. The uniform force and iDrive cases deviate significantly.

and allowing the transients to decay. The magnitude of the steady oscillations for a drive frequency is the value of the power spectrum at that frequency. Such simulations require more than a week each. Results from this approach are shown in Fig. 36(right) along with the numerical impulse and experimental results. From this plot we see that the impulse response is equivalent to the driven simulation approach. In addition, both approaches agree with the results from experiments.

Figure 37 shows the ratio of the noise spectrum of equilibrium fluctuations in tip-angle to the power spectrum from numerics and experiment. The ratio using the iDrive actuation power spectrum is nearly constant over the frequency

range shown. This is contrary to the predictions of infinite cylinder theory (see the dashed curves in Fig. 26), and may be attributed to the complex three-dimensional geometry or the novel actuation technique.

Figure 37 shows the ratio of noise to power spectra using a uniformly distributed actuation, see Fig. 15(left). The results for the two driving mechanisms yield a significantly different frequency dependence. This indicates that the method of actuation changes the shape of the power spectrum and therefore the ratio of thermally to externally driven spectra. The differences in the power spectrum are from $s_D(x|\omega)$ in Eq. (38). By varying the amount of energy the drive force distributes to each mode it is possible to change the relative magnitudes of the resonance peaks. This is accomplished by varying the spatial distribution of the forcing. The iDrive technique distributes the energy in such a way that the power spectrum and noise spectrum are nearly identical. In contrast, a uniform force yields a much lower relative magnitude for the second peak than the noise spectrum. This indicates that the method of drive has a strong affect on the frequency dependence for the ratio of the noise to power spectrum.

6 The Dynamics of Cantilevers in Fluid Near a Planar Boundary

6.1 Chapter Overview

It is necessary to quantify the dynamics of micro and nanoscale cantilevers for the conditions of experiment. The results of Chapters 2, 4, and 5 show examples of applying the thermodynamic approach to describe the motion of cantilevers far from solid surfaces, for example when calibrating the cantilever. This chapter investigates the effects of operating a small scale cantilever in fluid and in proximity to a solid surface. This discussion is confined to a study of the stochastic cantilever dynamics, though a similar study for the externally driven dynamics is a straightforward extension. The presence of a planar boundary changes the stochastic dynamics of the cantilever by disrupting the flow, see Fig. 38. This causes an increase in the added mass and viscous damping from the fluid. These results indicate in what range of cantilever-wall separations effects of a solid boundary are significant. Also, the trend in the quality factor and resonant frequency of the fundamental peak of the noise spectrum is quantified for separations ranging from no surface interaction to a strong interaction. This is useful to predict the stochastic dynamics of cantilevers in experiment as they approach a solid boundary.

6.2 Effects of a Solid Boundary

In practice, the cantilever is never placed in an unbounded fluid. Instead, it is common for the cantilever to be placed near solid planar boundaries. The influence of nearby boundaries must be accounted for to provide a more complete description of the dynamics. In many cases the cantilever is purposefully brought near a surface in order to probe some interaction with the cantilever or to probe features of the surface. To specify this discussion, the situation depicted in Fig. 6 showing a cantilever a distance s from a planar boundary

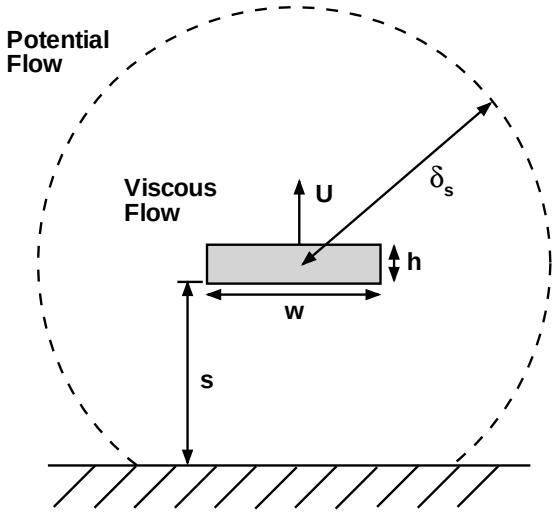

Figure 38: A schematic of the fluid flow regions around a cantilever in the vicinity of a solid surface (not drawn to scale). As the boundary moves into the Stokes layer the viscous flow must adjust.

is considered. The following discussion studies the case where the cantilever exhibits flexural oscillations in the direction perpendicular to the boundary. However, it should be emphasized that this approach is general and can be used to explore arbitrary cantilever orientations and oscillation directions if desired. The fluid is assumed to be unbounded in all other directions. The boundary will influence the dynamics of the cantilever [10, 46, 53], resulting in a reduction in the resonant frequency and quality factor. This has been described theoretically for the case of a long and thin cantilever of simple geometry where the fluid dynamics have been assumed two-dimensional [28, 29, 43, 44].

In the following the thermodynamic approach is applied with finite element numerical simulations to quantify the dynamics of the Veeco V-shaped cantilever as a function of its separation from a boundary. A total of 8 simulations have

Case	$s(\mu\text{m})$	s/h	s/δ_s	Q	ω_f/ω_0
1 †	60	100.0	14.5	2.03	0.216
2	40	66.7	9.7	1.98	0.213
3 †	25	41.7	6.0	1.94	0.213
4	20	33.3	4.8	1.79	0.207
5 †	15	25.0	3.6	1.62	0.200
6	15	25.0	3.6	1.59	0.197
7	12	20.0	2.9	1.38	0.178
8	10	16.7	2.4	1.23	0.154

Table 11: Separations, quality factors, and resonant frequencies for the 8 simulations with different wall-cantilever separations. A † indicates results obtained by measuring tip-angle.

been performed over a range of separations from 10 to 60μm using both the tip-deflection and tip-angle formulations, see Table 11. The noise spectra for these simulations are shown in Fig. 39. Using the insights from numerical simulations of the cantilever in an unbounded fluid it is expected that the relevant length scale for the fluid dynamics is twice the width of a single arm, $2w$. Using the peak frequency of the cantilever in unbounded fluid yields a Stokes length $\delta_s = 4.14\mu$m,

$$\frac{\delta_s}{w} = R^{-1/2} = \sqrt{\frac{\nu_f}{\omega_f w^2}}. \tag{106}$$

For the cases studied $2.5 \lesssim s/\delta_s \lesssim 15$, which covers the range from what is expected to be a strong influence of the wall to a negligible influence. Figure 39 clearly shows a reduction in the peak frequency and a broadening of the peak as the cantilever is brought closer to the boundary. In fact, for the smaller separations the peak is quite broad and the trend suggests that eventually the peak will become annihilated as the cantilever is brought closer to the boundary.

Using the noise spectra, a peak frequency ω_f and a quality factor Q can be calculated for the fundamental mode as a function of separation from the

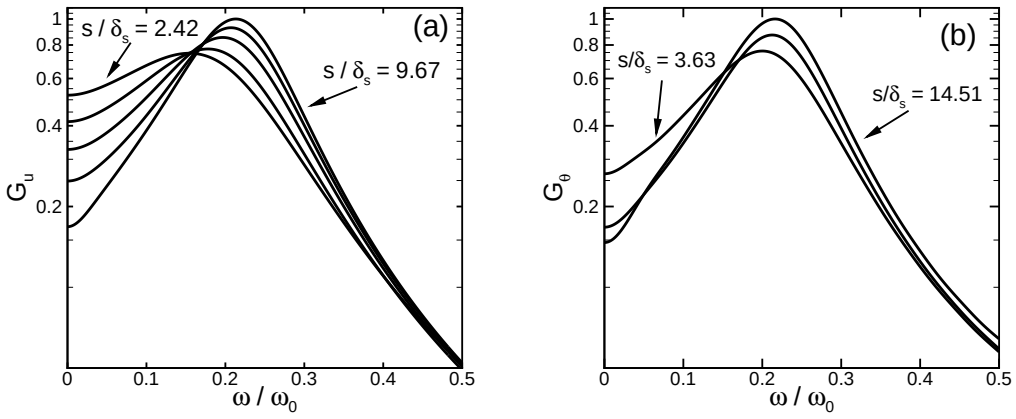

Figure 39: Panel (left) The noise spectra G_u of stochastic fluctuations in cantilever tip-deflection for separations $s = 10, 12, 15, 20, 40\mu$m. Panel (right) the noise spectra G_θ of stochastic fluctuations in cantilever tip-angle for separations $s = 15, 25, 60\mu$m. The spectra have been normalized by the maximum value of G_u or G_θ. The smallest and largest values of separation are labeled with all other values appearing sequentially.

boundary. These parameters are plotted in Fig. 40. The horizontal dashed line represents the value of the peak frequency and quality factor in the absence of bounding surfaces using the two-dimensional infinite cylinder approximation [59] where the cylinder width has been chosen to be $2w$. It is clear that for separations greater than $s/\delta_s \gtrsim 7$ the V-shaped cantilever is not significantly affected by the presence of the boundary, in good agreement with [20]. However, as the separation decreases below this value the peak frequency and quality factor decrease rapidly. These variations are in agreement with those presented by Basak, *et al.* for quality factor and added mass for the C2 microcantilever [9].

The triangles in Fig. 40 represent the theoretical predictions of Green and Sader [43, 44] using a two-dimensional approximation for a beam of uniform cross-section that accounts for the presence of the boundary, and again uses a width of $2w$. Despite the complex and three-dimensional nature of the flow

field the theory is able to accurately predict the quality factor over the range of separations explored. The frequency of the peak for the V-shaped cantilever shows some deviation from these predictions.

In general, an increase in the period of oscillation for a submerged object is attributed to the mass of fluid entrained by the object [73]. The lower peak frequency calculated for the V-shaped cantilever using a two-dimensional solution indicates an over-prediction of the added mass. This is due to the three-dimensional flow around the tip being neglected. It is reasonable to expect the cantilever tip to carry a smaller amount of fluid than a section of the beam body moving with the same velocity, see Fig. 29. The quality factor relates to the ratio of the mass loading and the viscous dissipation and is less sensitive to deviations incurred from the two-dimensional approximation. Despite neglecting three-dimensional flow around the cantilever tip, the two-dimensional model for the fluid flow around the V-shaped cantilever gives an accurate prediction of the peak frequency and quality factor.

The lower bound of wall-cantilever separation s is a result of limitations of the numerical scheme. The minimum separation is significantly larger than the size of a single molecule. It is expected that the use of adaptive meshing will allow for investigation of smaller gaps. However, the results present a trend that is expected to continue for smaller separations. In experiments the cantilever may be inclined to the surface, causing different flow dynamics [3, 30]. It is straightforward to use the approach applied here to study the affects of such a configuration.

These results indicate that for gaps smaller than $5\delta_s$ the first mode peak begins to be annihilated. The larger mass of fluid entrained by the cantilever and large viscous damping cause the quality factor to diminish. One approach to overcome the strong fluid effects is to tailor the geometry to achieve higher

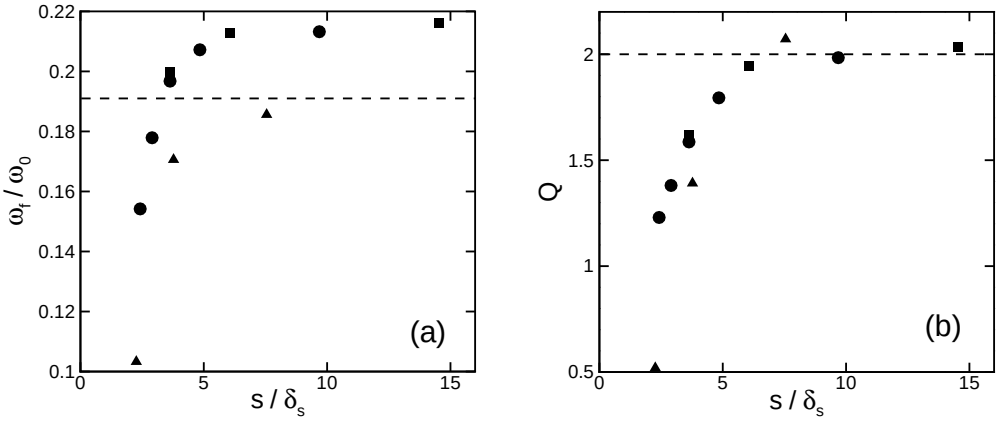

Figure 40: The variation of the peak frequency (panel (a)) and quality (panel (b)) of the fundamental mode of the V-shaped cantilever in fluid as a function of separation from a nearby wall. Results calculated using tip-deflection are circles, results using tip-angle are squares, and theoretical predictions using the results of Ref. [43] are triangles. The peak frequency and quality factor of the fundamental mode in an unbounded fluid are $\omega/\omega_f \approx 0.19$ and $Q \approx 2$ and are represented by the horizontal dashed line. The distance s is normalized by the Stokes length $\delta_s = 4.14\mu$m.

frequency oscillations and therefore higher quality oscillations. While this approach has yielded promising results [79], it requires constructing a cantilever for each experimental purpose. Instead, it is possible to use the stochastic dynamics of higher order cantilever modes for measurements. In this way existing cantilevers can be used to produce higher quality oscillations at higher frequencies.

7 Numerical Resolution Study for Higher Modes

7.1 Chapter Overview

Microscopic cantilevers have strong potential to analyze individual biological molecules in their ambient environments [5]. An open challenge to the study of single molecules in liquids using nanoscale cantilevers is the low quality resonance peaks resulting from strong viscous damping. In addition, Chapter 6 indicates that the presence of a solid surface further reduces the quality factor and peak frequency, eventually annihilating the first mode. However, it is desirable to have a high resonator quality factor for the purposes of measurement [77]. One possible approach is to use higher modes of cantilever oscillation. Chapter 3 shows that a significant amount of the total beam energy is distributed to the higher modes if one measures the angle of the cantilever tip. The energy has been shown to be further shifted to lower frequencies due to the presence of a solid surface, as shown in Chapter 6. This necessitates the use of higher frequency resonances. Also, the smaller magnitude of higher mode fluctuations means the magnitude of the thermal noise is smaller. Therefore it is possible to improve sensitivity of measurements by using higher modes [13]. A detailed description of the dynamics of higher order cantilever modes is necessary in order to implement measurements that take advantage of these modes.

7.2 Analytical Predictions

The approximations of infinite cylinder theory to account for the fluid dynamics over the beam accurately predict the dynamics of rectangular cantilevers in viscous fluid for the fundamental mode. This approximation is used here to describe the stochastic dynamics of a cantilever in viscous fluid for higher modes. The quality factor is linked to the resonant frequency through the Reynolds

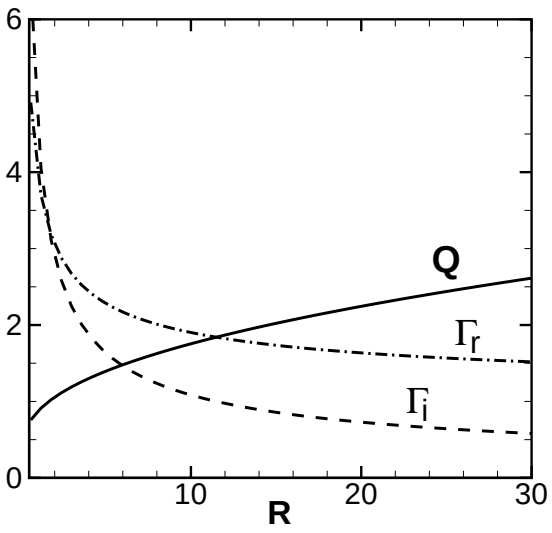

Figure 41: The quality factor Q as a function of Reynolds number R for a single mode. Also plotted are the real and imaginary parts of the hydrodynamic function for an infinite cylinder, Γ_r and Γ_i respectively.

number,

$$Q = \frac{\frac{1}{T_0} + \Gamma_r(R_0\tilde{\omega})}{\Gamma_i(R_0\tilde{\omega})}. \tag{107}$$

Here $R_0 = \omega_0 w^2/(4\nu)$ is the Reynolds number based on the resonant frequency in vacuum ω_0, and $\tilde{\omega} = \omega/\omega_0$ is the normalized frequency. The hydrodynamic function for a cantilever can be estimated using infinite cylinder approximations [65]. For moderate mode number this is the hydrodynamic function shown in Eq. (15). Higher modes generate more complex fluid dynamics and yield a modified solution [75].

The quality factor as a function of Reynolds number is plotted in Fig. 41 for a single mode. This figure shows that as the frequency increases, and therefore the Reynolds number, the quality factor also increases, see Fig. 42. Higher order modes have higher frequencies of oscillation [49]. The higher resonant

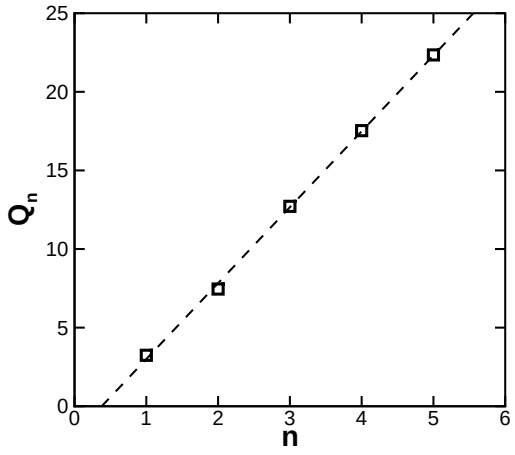

Figure 42: The quality factor for the first 5 modes of the C2 cantilever using eigenfrequencies $\omega_{f,n}$ in fluid from infinite cylinder theory. The dashed line is a linear fit, $Q_n = 5.829n - 1.828$.

frequencies of higher modes means that these modes will have increasingly larger quality factors than the first mode. Therefore, higher modes can be a useful tool for making measurements. Also, the higher resonant frequencies would improve the temporal resolution of measurements.

Another advantage of the higher eigenfrequencies of higher cantilever modes is the smaller associated Stokes lengths. In Chapter 6 it was shown that the fluid loading on the cantilever increases as the gap width decreases beyond $s \sim 5\delta_s$. As the resonant frequency increases the Stokes length decreases, meaning for the same wall-cantilever separation higher modes are less affected by the larger viscous damping, see Fig. 43. Therefore, as gap widths approach tens of nanometers the quality factor of higher modes remains large. This investigation is valid as long as the continuum hypothesis is valid and the frequency is low enough to neglect quantum dynamics. Quantum mechanics are negligible up to $f_{max} = \omega_{max}/2\pi \approx 10$ THz. The corresponding lower limit of separations in

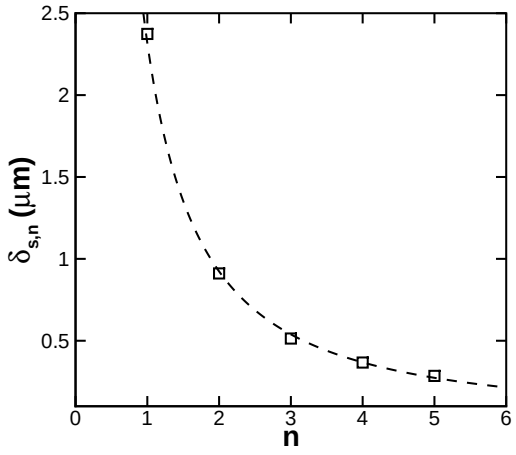

Figure 43: The Stokes lengths for the first 5 modes of the C2 cantilever using eigenfrequencies in fluid $\omega_{f,n}$ from infinite cylinder theory. The dashed line is a power law fit, $\delta_{s,n} = 2.32 \times 10^{-6}\ n^{-1.328}$.

water is $s_{min} \approx 3\mathring{A}$, approximately the size of a water molecule. The continuum hypothesis remains valid so long as gap widths as much larger than the mean free path, $\lambda \ll s$. This indicates that the separations must be much larger than the diameter of a water molecule.

The approximate solution based on infinite cylinder theory is two-dimensional. As the mode number increases, the associated mode shape becomes more complex, see Fig. 10. This generates three-dimensional flows along

L (μm)	w (μm)	h (μm)	k (N/m)	f_0 (kHz)
100	5	0.5	0.027	69.4

Table 12: The geometry of the high aspect ratio cantilever used to investigate higher mode dynamics. The aspect ratios are $L/w = 20$ and $w/h = 10$ so that infinite cylinder assumptions are valid. Also shown are the bulk spring constant k and resonant frequency in vacuum f_0. The cantilever is submerged in fluid with density of ρ=997 kg/m^3 and viscosity of $\mu_f = 1 \times 10^{-5}$kg/m-s.

n	$\omega_{f,n}/\omega_0$	Q_n	$\delta_{s,n}(\mu\text{m})$	$R_{0,n}$	$R_{f,n}$
1	0.41	5.48	0.236	272	112
2	3.04	13.83	0.087	1703	827

Table 13: Peak frequency, quality factor, and Stokes length for the first two modes of the high aspect ratio cantilever in low viscosity fluid ($\rho = 997\text{kg/m}^3$, $\mu_f = 1 \times 10^{-5}\text{kg/m-s}$).

the length of the cantilever [75]. It is therefore necessary to describe the complete flow around the cantilever. In this way it is possible to understand the effects of viscous damping and the mass of fluid entrained by the cantilever motion for all modes. This can be accomplished using the thermodynamic approach to calculate the stochastic dynamics from deterministic numerical simulations.

7.3 Numerical Simulations of Multiple Cantilever Modes

Numerical simulations are employed to determine the full, transient, three-dimensional fluid-structure interaction of a microscopic cantilever in viscous fluid [38]. This code has been validated for the first mode [59]. To verify the validity of this approach for higher modes, a high aspect ratio cantilever geometry is chosen that is well described by the infinite cylinder approximation. Therefore, the quality factors and resonant frequencies of the modal peaks calculated from numerical simulations should be comparable to the analytical predictions.

The geometry of the high aspect ratio cantilever is shown in Table 12, along with the bulk spring constant and resonant frequency in vacuum for the first mode. The deviation between the approximate values and those from numerics can be determined. These dynamics depend on the fluid surrounding the cantilever. In order to study the effects of the numerical parameters, such as time

n_p	$\Delta t(\mu\text{s})$	$\omega_{f,1}/\omega_0$	$\omega_{f,2}/\omega_0$	Q_1	Q_2
20	0.237	0.39	2.61	4.02	3.11
30	0.158	0.40	2.63	4.16	4.68
40	0.118	0.40	2.64	4.24	5.70

Table 14: Peak frequency and quality factor for the first two modes of the cantilever as calculated from numerics for three different time steps. n_p is the number of time steps per mode two oscillation. The values for peak frequency and quality factor from infinite cylinder theory are shown in Table 13. All simulations have the same bounding box ($s_y = 10\delta_{s,1}$) and spatial resolution ($\Delta x = 0.375\delta_{s,1}$).

step, grid resolution, and simulation domain size, it is desirable to run simulations that complete quickly. This is accomplished by diminishing the necessary size of the domain. An oscillator in a fluid with a lower viscosity will generate a smaller viscous boundary layer and therefore a smaller volume of fluid must be simulated. Also, the lower viscosity allows the beam to maintain a high quality factor, so that a simple harmonic oscillator is an accurate model. For this purpose a fluid with the density of water $\rho = 997\text{kg/m}^3$ and a fictitious viscosity of $\mu_f = 1 \times 10^{-5}\text{kg/m-s}$ is used.

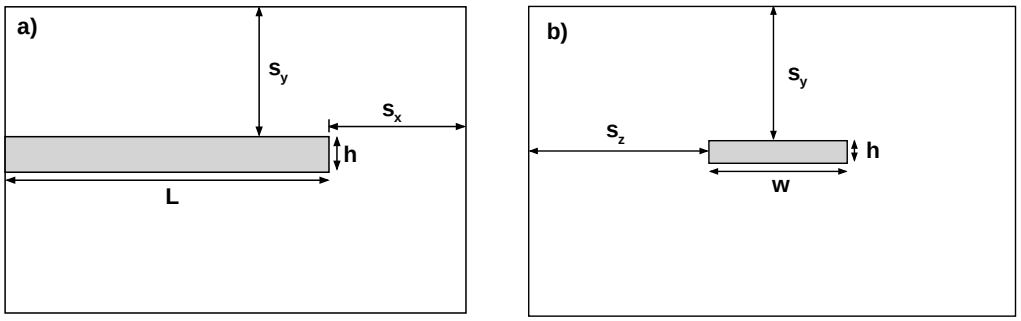

Figure 44: Schematics of the numerical domain including the cantilever and fluid in the a) $x - y$ and b) $y - z$ planes. The bounding box is a no-slip wall.

$\Delta x(\mu\text{m})$	$\Delta x/\delta s_1$	$\Delta x/\delta s_2$	$\omega_{f,1}/\omega_0$	$\omega_{f,2}/\omega_0$	Q_1	Q_2
0.375	1.59	4.31	0.40	2.63	4.16	4.68
0.300	1.27	3.45	0.39	2.63	4.60	4.48
0.250	1.06	2.87	0.38	2.63	4.09	4.09

Table 15: Peak frequency and quality factor for the first two modes of the cantilever as calculated from numerics for three different spatial resolutions, Δx. The values for peak frequency and quality factor from infinite cylinder theory are shown in Table 13. All simulations have identical time steps ($n_p = 20$) and bounding box size ($s_y = 10\delta_{s,1}$).

The analytical predictions for peak frequency and quality factor are shown in Table 13 along with the Stokes lengths for the first two modes. As expected the predicted values are close to the numerical results. In the following sections the deviation between numerics and theory for the second mode will be discussed. The goal is to determine the time step, spatial resolution, and bounding box size necessary to capture the fluid dynamics generated by the second mode of the cantilever. As a base simulation for comparison, a time step is chosen such that,

$$\Delta t = \frac{T_2}{n_p} = \frac{1}{n_p}\frac{2\pi}{\omega_{f,2}}, \tag{108}$$

where T_2 is the period of oscillation for the second mode in fluid and $n_p = 20$ is the number of time steps taken per period. The wall-cantilever separation for the base case is $s_x = 20\delta_{s,1}$, $s_y = 10\delta_{s,1}$, and $s_z = 20\delta_{s,1}$, see Fig. 44. In this notation, s_i is the distance from the cantilever to the simulation boundary in the i-direction. These separations are defined in units of Stokes lengths for mode one, $\delta_{s,1} = (\nu_f/\omega_{f,1})^{1/2} \approx 0.24\mu$m. The base resolution is approximately $\Delta x = 0.35\mu$m in each direction, for a total of $46,436$ cells.

7.3.1 Effects of Diminishing Time Step

The numerical approach described above resolves the first mode of an oscillating cantilever. It is expected that calculating 20 points in each oscillation with a well resolved and large domain is sufficient to resolve the peak frequency and quality factor for the fundamental mode within reasonable error. In order to resolve the dynamics of mode two, the time step is chosen such that at least 20 points are calculated for each oscillation of mode two. In this section the variation of the fluid parameters with decreasing time step is investigated. The goal is to determine the necessary temporal resolution to accurately describe the second mode.

Three time steps are used in this investigation, using $n_p = 20, 30, 40$ in Eq. (108). The geometry and spatial resolution of the domain for each simulation is kept constant. The ringdown from the numerics is used to calculate the autocorrelation in cantilever tip-deflection, which then yields the noise spectrum [59]. Values of peak frequency for each mode are the locations of maximum magnitude in the noise spectrum. The peak frequency for both modes is shown in Table 14. For all time steps the frequency of the first mode is within 5% of the predicted value. The peak frequency of the second mode approaches the predicted value as the steps per oscillation increases (and the time step decreases). The quality factor for each mode is obtained by fitting the noise spectrum to a Lorentzian in the neighborhood of the peak,

$$\hat{Y}(\omega) = \frac{Y_0}{Q((1-\tilde{\omega}_n^2)^2 + (\tilde{\omega}_n/Q)^2)}. \tag{109}$$

Here Y_0 is the amplitude of the Lorentzian and $\tilde{\omega}_n = \omega/\omega_{f,n}$ is the frequency normalized by the resonant frequency in fluid of mode n, $\omega_{f,n}$. The results are shown in Table 14. This shows the quality factor of the first two modes for the three values of n_p. It is evident that decreasing the time step improves the

$s_y/\delta_{s,1}$	$\omega_{f,1}/\omega_0$	$\omega_{f,2}/\omega_0$	Q_1	Q_2
10	0.40	2.63	4.16	4.68
15	0.42	2.70	4.63	3.38
20	0.43	2.76	4.86	3.50

Table 16: Peak frequency and quality for the first two modes of the cantilever as calculated from numerics for three different simulation domain sizes. The values for peak frequency and quality factor from infinite cylinder theory are shown in Table 13. All simulations have the same time step ($n_p = 30$) and spatial resolution ($\Delta x = 0.375\delta_{s,1}$).

prediction of the quality factor for both modes. However, the deviation for the smallest time step is still very large.

The deviation in quality factor for the first mode is relatively constant. This discrepancy may be attributed to effects of the bounding walls on the oscillating cantilever. It has been shown that the presence of a solid surface enhances the damping and will result in a decrease in quality factor. The smallest deviation between the second mode quality factor from numerics and infinite cylinder is substantial. This is a result of lack of spatial resolution around the cantilever. The Stokes length for the second mode is $\delta_{s,2} = 87$ nm. However the spatial resolution is significantly larger, $\Delta x/\delta_{s,2}= 4.3$. The viscous dynamics due to the second mode are being lumped into the cells on the cantilever boundary. In order to resolve the fluid dynamics within the Stokes layer, the spatial resolution near the cantilever should be at least as small as the Stokes length.

From Tables 14 it is evident that a small time step is necessary to capture the flow dynamics. For the spatial resolution and bounding box used here, the time step should be at most 1/40 of the second mode period. The following sections investigate how the accuracy of the numerical simulation depends on the spatial resolution and size of the numerical domain. These parameters are studied individually to determine their effects. The knowledge of how the three

numerical parameters affect the accuracy can then be used to create simulations capable of resolving higher order modes.

7.3.2 Effects of Improving Spatial Resolution

The next simulation parameter considered is the spatial resolution in the fluid. The resolution in the fluid determines to what scale the fluid motion is calculated and also the resolution for the fluid-structure interaction. If the grid resolution is too coarse, much of the flow dynamics are lumped into a single numerical cell. This means most of the viscous fluid flow is not fully resolved. Three simulations with different spatial resolutions and identical time step and bounding box size are compared. The peak frequencies and quality factors for the first two modes are shown in Table 15. A decrease in the grid spacing by a factor of 1.5 does not significantly affect the modal properties. In fact, the results shift away from the infinite cylinder predictions.

For the first mode this is attributed to the combination of improved resolution in a bounding box that is too small. This is more accurately calculating the fluid-structure interaction in the vicinity of a solid surface. The second mode dynamics are not well captured by the more resolved case, with the grid spacing $\Delta x = 2.87\delta_{s,2}$. The peak frequency does not change, indicating that the mass loading is the same for both resolutions. However, the quality factor decreases, indicating that the viscous damping is found to be higher for the higher resolution case (see Eq. (104)). As the grid spacing decreases, the fluid dynamics due to the second mode are better resolved, although not completely. The viscous boundary layer is calculated more accurately than for the lower resolution, permitting a better estimate of velocity gradients that affect the viscous damping.

μ_f (kg/m-s)	$\delta_{s,2}(\mu\text{m})$	N_c	Q_2	n_1	n_2
1.0×10^{-5}	0.087	7.0×10^6	13.9	832	2435
1.0×10^{-4}	0.30	1.2×10^6	4.47	269	900
8.55×10^{-4}	1.04	0.34×10^6	1.67	100	540

Table 17: Properties of the high aspect ratio cantilever and two different viscosity fluids used. The Stokes length for mode two $\delta_{s,2}$, the corresponding number of cells N_c, the quality factor Q_2, and the number of time steps for modes one and two, n_1 and n_2 respectively are shown. The total number of time steps is based on 20 points per mode two oscillation and three oscillations of the total ring-down, $t_{max,n} = 3\tau = 3(2\pi Q_n/\omega_{f,n})$.

7.3.3 Effects of Increasing Domain Size

The final simulation parameter investigated is the size of the numerical domain. This is the distance between the cantilever and the boundary wall of the numerical domain, see Fig. 44. In order to compare with theory it is necessary for the cantilever-wall separations to be large enough for the effects of the walls on the flow field to be negligible. If this separation is too small, the no slip boundary condition of the bounding wall increases the added mass of fluid and viscous damping, as seen in Chapter 6. In order to capture the fluid dynamics around a cantilever for a given mode it is necessary to determine the appropriate size of the numerical domain. Numerical simulations were run for three different domain sizes in $5\delta_{s,1}$ increments. The time step is the same for each, corresponding to $n_p = 30$. Also, the same spatial resolution is maintained in each simulation.

Table 16 lists the peak frequency for the first two modes. The frequency of the first mode is similar for each simulation. For the larger domain sizes the frequency is larger than predicted by infinite cylinder theory. It has been seen that the two-dimensional approximations tend to overpredict the mass loading, resulting in a smaller resonant frequency in fluid [26]. As the domain

size is increased, the location of the second peak approaches the prediction from infinite cylinder theory. If the y-direction separation between the cantilever and bounding wall s_y is doubled, the second mode peak frequency improves by 4%.

Table 16 shows the quality factor for the first two modes. As the domain size is increased the quality factor of the first mode approaches the value from infinite cylinder theory. However, there is only a marginal change in the second mode quality factor. The lower frequency of the first mode means the resulting Stokes length will be larger. By increasing the size of the bounding box the effects of the side walls on the cantilever dynamics diminish. The dynamics of the first resonance will propagate further into the fluid domain, and the larger distance to the wall has a greater impact on the parameters of this mode than higher harmonics. This indicates that in this range the bounding box size does not strongly affect the second mode. Therefore, the base simulation domain size is sufficient to capture the second mode dynamics.

It may be possible to take advantage of the fact that the size of the domain has a minimal affect on the second mode for the dimensions used here. A small simulation domain that causes enhanced dissipation in the first mode will not strongly affect the second mode. This simulation is useful to calculate the actual dynamics of the second mode from a lower quality first mode response. The time required to complete this simulation will be shorter than needed to simulate the actual response of the first mode due to the diminished quality factor. In addition, this result gives insight into experiments that measure higher mode dynamics near a wall. This preliminary result indicates that the presence of a solid boundary only appreciably affects modes when it is inside the Stokes region of that mode.

7.4 Numerical Simulation of Individual Cantilever Modes

From the above discussion it is evident that simulating the fluid-structure interaction for multiple modes simultaneously is difficult. In order to capture all of the flow for the lower modes the bounding box must be large. However, in order to capture the dynamics of the higher modes the time step must be small enough to resolve the higher frequency motion. The spatial resolution must be smaller than the Stokes length for the highest mode of interest. In order to meet all of these requirements, a simulation would be required to have a very large number of cells and run for many time steps. Instead, simulating the ringdown of only the mode of interest would require a smaller simulation with fewer time steps.

The length of time necessary for a simulation to complete is dependent on the number of cells in the domain and the number of time steps required. The total number of cells is a function of the size of the bounding box and the spatial resolution needed to capture the viscous motion near the cantilever. For a given beam geometry (L, w, h) the size of the domain depends on the volume of fluid it is necessary to incorporate. Once the total number of cells in the domain is calculated, the time required to complete a single time step can be determined. Then the total simulation time is this value multiplied by the number of time steps.

In order to estimate the size of the domain needed for a single mode, consider a number λ of Stokes lengths of fluid are required. This means that the wall-cantilever separation is $s = \lambda\delta_{s,n}$. For simplicity, assume that the bounding walls are the same distance in each direction ($s = s_x = s_y = s_z$). Here n is the mode number of interest. The number of cells N_c for this case would be the sum of the number of cells in the beam and the cells in the fluid. This can be

estimated as,

$$N_c = (\Delta x)^{-3}\left[4s^3 + (2w + 2h + 4L)s^2 + (2wL + 2hL + wh)s + Lwh\right]. \quad (110)$$

Here Δx is the spatial resolution and cubic elements are assumed ($\Delta x = \Delta y = \Delta z$). The spatial resolution should be at most the Stokes length, $\Delta x \leq \delta_{s,n}$. The minimum number of cells for a fluid simulation for mode n is,

$$N_c = (\delta_{s,n})^{-3}\left[4s^3 + (2w + 2h + 4L)s^2 + (2wL + 2hL + wh)s + Lwh\right]. \quad (111)$$

It is obvious that the number of cells and therefore the computational cost decreases with increasing Stokes length. In addition, the quality factor increases with decreasing Stokes length meaning more time steps are necessary to simulate the full ring-down. This means that the choice of a low viscosity fluid actually increases the time required to simulate the dynamics of a single mode. Table 17 shows the number of cells needed to resolve only mode n of the high aspect ratio cantilever and the number of time steps needed for 20 points per oscillation of mode two. Values are shown for $\lambda = 25$ and the viscosity used in previous sections, that of water, and an intermediate value.

In order to take advantage of the decreased simulation time of simulating only the mode of interest, the mode dynamics must be separated. In order to calculate the autocorrelation and corresponding noise spectrum, the response of the mode to the removal of a step force or torque is desirable. This is accomplished by initially deflecting the cantilever in the mode shape of interest. Deflecting the cantilever in this manner activates mode n only; no energy is distributed to other modes. This is a result of the orthogonality of the modes and the fact that small displacements do not couple the modes. In this way the quantity of fluid to be simulated must only meet the requirements of a single mode. In addition, the time step can be chosen to resolve this mode without

need to resolve the ringdown of lower frequency modes. This decreases the time required to simulate the dynamics of higher modes.

It is desirable to apply the approach of simulating only a single mode of a cantilever to the second mode of the C2 cantilever in water. The separation between the wall and cantilever is chosen to be $15\delta_{s,2}$ in the x-, y- and z-directions. The time step is chosen to resolve 40 points per oscillation of mode two. The Stokes length of mode two of the C2 cantilever in water is $\delta_{s,2} = 0.91\mu$m. This is therefore the maximum spatial resolution for a simulation of mode two. Using Eq. (111) it can be calculated that the minimum number of cells needed for this simulation is $N_c = 460,000$. Using the current FEM software a simulation with this number of cells requires more than 1.5 gigabytes of memory. A simulation of this size is at the upper bound to be placed in memory for a 32 bit computer and operating system. In order to obtain the necessary resolution while maintaining a sufficiently large bounding box, either an adaptive approach or a larger memory allocation per process is necessary. A possible adaptive approach is available using the ADINA fluid-structure interaction solver [1]. This solver can incorporate full viscous flow fluid elements as well as potential flow elements. Using such an approach the flow is well resolved near the cantilever and less resolved far from the beam and results in significant computational savings. The adaptive meshing available for fluid domains has been used to calculate the quality factor and peak frequency of a driven cantilever [9].

8 Quantifying the Mass Loading and Viscous Damping

8.1 Chapter Overview

The flow of a viscous fluid around an oscillating micro or nanoscale cantilever is complex. Analytical expressions for the added mass of fluid and viscous damping approximate the flow as two-dimensional flow around an infinite cylinder. These expressions are idealized and do not capture the complicated flow due to three-dimensional geometries. It is useful to calculate the added mass of fluid and the viscous damping from numerical simulations in order to determine the fluid dynamics for the exact configuration of interest.

8.2 Fluid Dynamics Around a Cantilever

The equation of motion for a single cantilever mode is,

$$m_e \ddot{U}_n + k_n U_n = F_f + F_D. \tag{112}$$

In this expression U_n is the position of the cantilever tip, $m_e = \alpha m_c$ is the effective mass such that the kinetic energy is correct, k_n is the dynamic spring constant of mode n, F_f is the force due to the fluid, and F_D is the driving force. In Fourier space this is,

$$-\omega^2 m_e \hat{U}_n + k_n \hat{U}_n = \hat{F}_f + \hat{F}_D. \tag{113}$$

The force due to the fluid can be separated into contributions due to the mass of fluid entrained by the cantilever and the viscous damping. The force due to the added mass is proportional to the cantilever tip acceleration, and the force due to the damping is proportional to the velocity. After rearranging this becomes,

$$-\omega^2 m_f \hat{U}_n - i\omega\gamma_f \hat{U}_n + k_n \hat{U}_n = \hat{F}_D. \tag{114}$$

and solving for $\hat{U}_n(\omega)$ gives,

$$\hat{U}_n(\omega) = \frac{\hat{F}_D(\omega)}{(k_n - m_f\omega^2) - i(\omega\gamma_f)} = \frac{\hat{F}_D(\omega)((k_n - m_f\omega^2) + i(\omega\gamma_f))}{(k_n - m_f\omega^2)^2 + (\omega\gamma_f)^2}. \tag{115}$$

For the case of an impulse driving force localized at the tip, $F_D = F_0\delta(t)$ this gives $\hat{F}_D(\omega) = F_0$ and,

$$\hat{U}_n(\omega) = \frac{F_0((k_n - m_f\omega^2) + i(\omega\gamma_f))}{(k_n - m_f\omega^2)^2 + (\omega\gamma_f)^2}. \tag{116}$$

Separating into the real and imaginary parts $\hat{U}_n = \hat{U}_{n,r} + i\hat{U}_{n,i}$ yields,

$$\hat{U}_{n,r}(\omega) = \frac{F_0(\omega\gamma_f)}{(k_n - m_f\omega^2)^2 + (\omega\gamma_f)^2}, \tag{117}$$

$$\hat{U}_{n,i}(\omega) = \frac{F_0(k_n - m_f\omega^2)}{(k_n - m_f\omega^2)^2 + (\omega\gamma_f)^2}. \tag{118}$$

This is the response of any damped spring-mass system in fluid. The mass of fluid entrained by the cantilever $m_f(\omega)$ and the viscous damping $\gamma_f(\omega)$ are functions of frequency. For infinite cylinder theory the parameters are expressed in terms of the hydrodynamic function,

$$m_f(\omega) = \alpha m_c(1 + T_0\Gamma_r(\omega)) \approx \Gamma_r(\omega), \tag{119}$$

$$\gamma_f(\omega) = \alpha m_{cyl}\omega\Gamma_i(\omega) \approx \omega\Gamma_i(\omega). \tag{120}$$

It should be noted that for moderate mode number $n \lesssim 4$ the mass loading and viscous damping are independent of mode number. These are plotted as the dashed lines in Fig. 45 and 46. The added mass is a decreasing function of frequency, while the viscous damping gradually increases with frequency.

Equation (116) is for a single mode. The dynamics of multiple modes together is considered in Section 8.4. It is straightforward to calculate the cantilever response to an impulse force using numerics. The Fourier transform of the cantilever impulse response gives the cantilever tip-deflection of the form in Eq. (116). For a single mode, the added mass and viscous damping are then,

$$m_f = \frac{-F_0\hat{U}_r + k_n(\hat{U}_r^2 + \hat{U}_i^2\omega^2)}{\omega^2(\hat{U}_r^2 + \hat{U}_i^2\omega^2)}, \tag{121}$$

$$\gamma_f = \frac{F_0\hat{U}_i^2}{(\hat{U}_r^2 + \hat{U}_i^2\omega^2)}. \tag{122}$$

These can be calculated from numerical simulations to include the full three-dimensional flow.

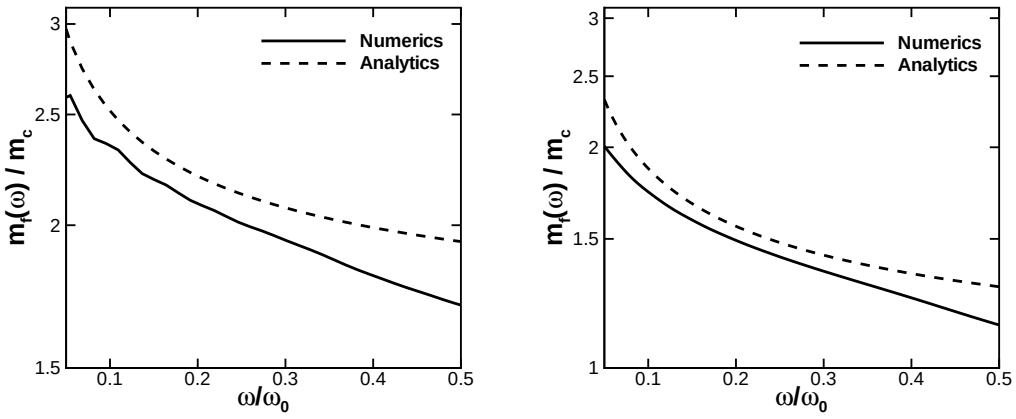

Figure 45: (left) The fluid mass loading for the C2 cantilever calculated from the tip-deflection numerics (solid) and infinite cylinder theory (dashed). (right) The mass loading for the C2 cantilever with half the width, $w' = w/2$, calculated from the tip-deflection numerics (solid) and infinite cylinder theory (dashed).

8.3 Fluid Dynamics for Three-Dimensional Rectangular Cantilevers

A numerical approach is necessary in order to calculate the fluid dynamics around a microscopic cantilever for the precise geometry of interest. Two-dimensional approximations are adept at predicting the noise spectrum and power spectrum for certain cantilevers. However, it is unknown how accurately these approximations predict the fluid added mass and viscous damping. This section presents a study of the fluid added mass and viscous damping for the full fluid-structure interaction of a three-dimensional cantilever in viscous fluid.

The response of a cantilever to an impulse force gives the power spectrum of cantilever tip oscillations [59]. Using a single mode model, the cosine (real) and sine (imaginary) Fourier transform of this response are shown in Eq. (117)

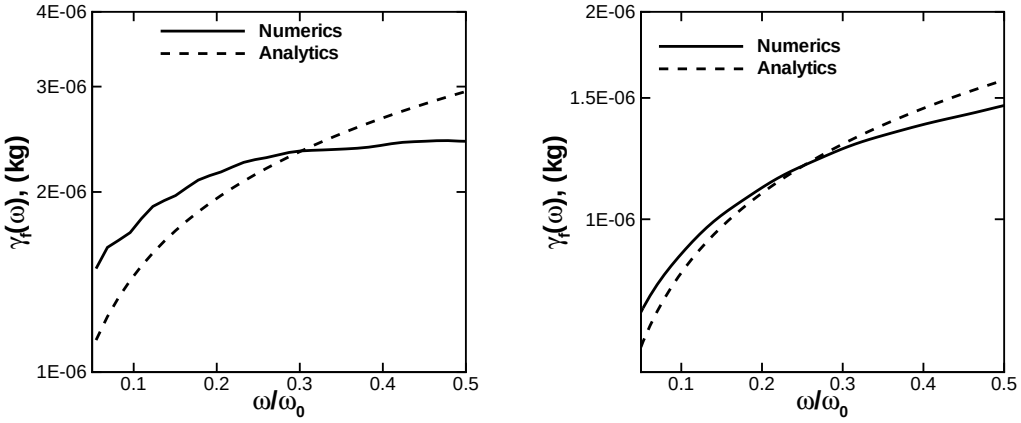

Figure 46: (left) The viscous damping for the C2 cantilever calculated from the tip-deflection numerics (solid) and infinite cylinder theory (dashed). (right) The viscous damping for the C2 cantilever with half the width, $w' = w/2$, calculated from the tip-deflection numerics (solid) and infinite cylinder theory (dashed).

and (118). The added mass of fluid and viscous damping are calculated using Eq. (121) and (122. These parameters for the C2 cantilever are plotted in Fig. 45(left) and 46(left), respectively, along with approximations based on infinite cylinder theory.

The mass loading from numerical simulations is similar to that from infinite cylinder theory. In the vicinity of the resonant peak ($\omega/\omega_0 \approx 0.34$) the lumped three-dimensional viscous damping is similar to infinite cylinder approximations. However, the two deviate for lower and higher frequencies. The low frequency variation is attributed to three-dimensional flow around the cantilever tip, while the high frequency variation is attributed to contributions from the second mode lumped into a single mode model. The comparison between viscous damping from numerics and infinite cylinder theory yields similar trends.

The infinite cylinder approximation is valid for $w/L \to 0$. As the width of the cantilever is decreased and all other parameters held constant we expect

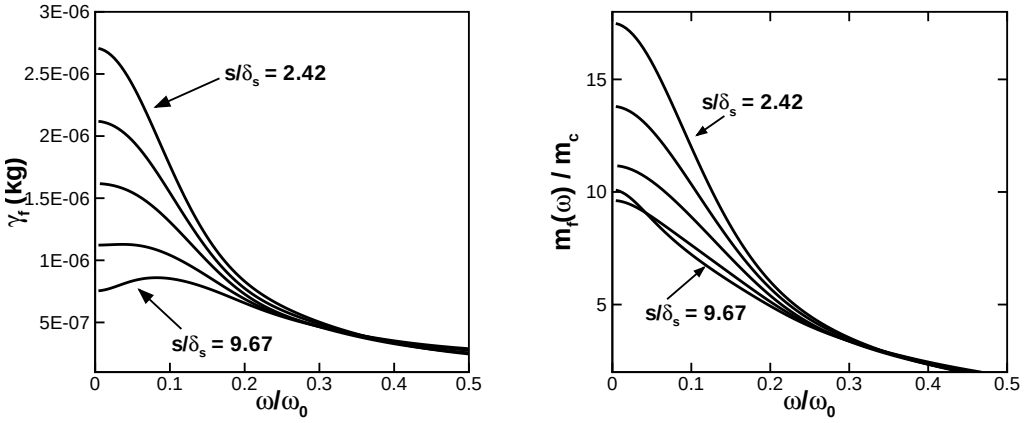

Figure 47: The three-dimensional (left) mass loading and (right) viscous damping for the V-shaped Veeco cantilever near a solid surface. The damping is shown for numerical simulations measuring cantilever tip-deflection.

the ratio of the spectra for the three-dimensional cantilever to approach the analytical solution. For the case of a cantilever with half the width the mass loading and viscous damping approaches that of the infinite cylinder theory, see Figs. 45(right) and 46(right). We have seen that infinite cylinder approximations accurately predict peak location and quality factor for the C2 cantilever. From these plots we see that the analytical predictions for the precise frequency variation of the fluid parameters can exhibit deviation even for rectangular cantilevers.

The approach outlined above is general and can be applied to any cantilever. In addition, the increased damping and added mass due to the presence of a solid surface can also be quantified using this approach. This application is straightforward and has been applied to the V-shaped Veeco MLCT Type E microlever used in Chapter 5. The added mass and viscous damping are shown in Fig. 47. It is evident from this plot that both the mass loading and viscous damping on the first cantilever mode increase with decreasing wall-cantilever

separation.

8.4 Fluid Dynamics around a Cantilever for Multiple Modes

In order to correct the frequency dependent parameters at higher frequencies, it is necessary to incorporate higher modes. This is accomplished by a linear superposition of the contributions from each mode. The corresponding sine and cosine Fourier transforms are,

$$\hat{U}_i = \sum_{n=1}^{\infty} \hat{U}_{n,i}, \tag{123}$$

$$\hat{U}_r = \sum_{n=1}^{\infty} \hat{U}_{n,r}. \tag{124}$$

The fluid mass loading and viscous damping can then be found in a similar approach by solving these equations. The Fourier transforms have the form,

$$\hat{U}_r(\omega) = \sum_{n=1}^{\infty} \frac{F_0 \omega \gamma_f}{(k_n - m_f\omega^2)^2 + (\omega\gamma_f)^2}, \tag{125}$$

$$\hat{U}_i(\omega) = \sum_{n=1}^{\infty} \frac{F_0 (k_n - m_f\omega^2)}{(k_n - m_f\omega^2)^2 + (\omega\gamma_f)^2}. \tag{126}$$

At moderate mode number the mass loading and viscous damping are functions of frequency alone. However, as the mode number increases these parameters begin to depend upon n [75]. For the case where the fluid parameters are independent of mode the expressions are functions of two variables and a solution is possible. Analytical expressions for the mass of fluid entrained by the cantilever and the viscous damping are not accessible. Instead, a numerical solution for the two functions is necessary. This can be accomplished using a Newton-Rhapson iterative solution [62].

This approach is capable of quantifying the fluid dynamics on a microscale cantilever in fluid. Using numerical simulations, this approach is valid for any cantilever geometry and configuration. Using the expressions for multiple

modes, the variation in the fluid dynamics for different modes can be studied. Such an analysis will give valuable insight into the fluid-structure interaction of microscopic cantilevers for experiments.

9 Conclusions

Micro and nanoscale systems are pushing experiment to improve resolution and sensitivity. In particular, microscopic cantilevers are promising tools for studying individual molecules. Experiments using small devices require an understanding of the physics at micro and nanoscales. Available theories are often highly idealized and only approximate the dynamics. A numerical approach is necessary to quantify the dynamics of microscopic structures in fluid for the precise conditions of experiment. The approach presented in this thesis is general and applicable to many systems of current technological and scientific interest.

The use of small cantilevers is a promising method to study the properties of biological systems in real time. In many cases this requires a cantilever to operate in viscous fluid. The fluid has the effect of spreading the resonant peak and shifting it to lower frequency, impeding measurements. In order to overcome strong damping it is necessary to understand the interaction between the fluid and cantilever. The infinite cylinder model for the fluid dynamics is adept at estimating the force of the fluid on a long and thin cantilever with uniform cross-section. The noise and power spectrum, and the corresponding quality factor and resonant frequency for rectangular cantilevers can be predicted using this approach. Numerical simulations can be employed instead in order to calculate the complete dynamics of cantilevers in fluid for the precise conditions of experiment.

The spectra describing the cantilever dynamics are found to depend upon the variable being measured. Measurements of tip-angle show a larger amount of energy in higher flexural modes of oscillation than what is found for tip-deflection measurements. This fact can be exploited to maximize or minimize the measured signal of higher modes by measuring tip-angle or tip-deflection,

respectively. The cantilever dynamics are found to depend upon the type of actuation employed. Thermally induced cantilever motion differs from externally driven motion, and the dynamics differ depending on the spatial distribution of the driving mechanism. In particular, an external driving that is uniformly distributed along the beam length yields smaller oscillations for higher modes than an external driving localized at the cantilever tip.

A further consideration for experiments using microscopic cantilevers for measurement is the oscillation of a cantilever in fluid in proximity to a solid surface. This is a common occurrence in experiments and is expected to modify the flow and therefore cantilever dynamics. The presence of a solid boundary in the proximity of a cantilever is found to generate larger viscous damping and increased added mass when compared with the same cantilever far from boundaries. This has the effect of further broadening the spectra and shifting the peak to lower frequency. A promising approach to overcome this larger viscous damping is to measure the dynamics of cantilever modes beyond the first. Higher modes oscillate at higher frequencies, have smaller viscous boundary layers, and have increased quality factors. This indicates that the cantilever-wall separation can be smaller before the surface begins to affect the flow generated by higher modes. The higher resonant frequency of higher modes also means measurements can be taken with improved time resolution.

In order to gain insight into the complete three-dimensional fluid-structure interaction it is beneficial to quantify the frequency dependence of the added mass of fluid entrained by a cantilever and the viscous damping. Numerical simulations are capable of calculating the full fluid flow and therefore can be used to quantify the added mass and viscous damping for the precise cantilever geometry and configuration of interest. For a rectangular cantilever, a single mode fit of the fluid parameters shows that infinite cylinder predictions are

accurate in the vicinity of the resonant peak. Multiple mode parameter fits are expected to determine the frequency dependence beyond the first mode.

The numerical approach discussed here is a powerful method for describing the complex motion of micro and nanoscale systems. Findings from this approach can explain phenomena encountered in current experiments and also guide future experiments. The approach is general and applies to the study of small scale elastic structure in fluid.

List of References

[1] ADINA FSI, www.adina.com.

[2] T. R. Albrecht, S. Akamine, T. S. Carver, and C. F. Quate. Microfabrication of cantilever styli for the atomic force microscope. *J. Vac. Sci. Technol. A*, 8(4):3386–3396, 1990.

[3] T. R. Albrecht and C. F. Quate. Atomic resolution imaging of a nonconductor by atomic force microscopy. *J. Appl. Phys*, 62(7):2599–2602, 1987.

[4] J. L. Arlett, J. R. Maloney, B. Gudlewski, M. Muluneh, and M. L. Roukes. Self-sensing micro- and nanocantilevers with attonewton-scale force resolution. *Nano Lett.*, 6(5):1000–1006, 2006.

[5] J. L. Arlett, M. R. Paul, J. Solomon, M. C. Cross, S. E. Fraser, and M. L. Roukes. Nanomechanical devices for single-molecule biophysics. In *Controlled Nanoscale Motion in Biological and Artificial Systems*, Nobel Symposium 131. Springer-Verlag, 2005.

[6] idrive actuation by asylum research, 2008. Asylum Research. www.asylumresearch.com, with J. E. Sader and J.P. Cleveland.

[7] I. Bargatin, I. Kozinsky, and M.L. Roukes. Efficient electrothermal actuation of multiple modes of high-frequency nanoelectromechanical resonators. *Appl. Phys. Lett.*, 90:093116, 2007.

[8] S. Basak and A. Raman. Hydrodynamic coupling between micromechanical beams oscillating in viscous fluid. *Phys. Fluids*, 19:017105, 2007.

[9] S. Basak, A. Raman, and S.V. Garimella. Hydrodynamic loading of microcantilevers vibrating in viscous fluids. *J. Appl. Phys.*, 99:114906, 2006.

[10] F. Benmouna and D. Johannsmann. Hydrodynamics interaction of AFM cantilevers with solid walls: An investigation based on AFM noise analysis. *Eur. Phys. J. E*, 9:435–441, 2002.

[11] G Binnig, C. F. Quate, and Ch. Gerber. Atomic force microscope. *Phys. Rev. Lett.*, 56(9):930–933, 1986.

[12] N. Bohr. The structure of the atom. Nobel Lecture, 1922.

[13] T. Braun, B. Viola, M.K. Ghatkesar, A.H. Bredekamp, C. Gerber, and M. Hegner. Micromechanical mass sensors for biomolecular detection in a physiological environment. *Phys. Rev. E*, 72:031907, 2005.

[14] R. Brown. Description of the random motion of dust particles, 1827.

[15] C. Bustamante, J. Macosko, and G. Wuite. Grabbing the cat by the tail: manipulating molecules one by one. *Nature Rev.*, 1:130–136, 2000.

[16] H.-J. Butt and M. Jaschke. Calculation of thermal noise in atomic force microscopy. *Nanotech.*, 6:1–7, 1995.

[17] H.-J. Butt, P. Siedle, K. Seifert, K. Fendler, T. Seeger, E. Bamberg, A.L. Weisenhorn, K. Goldie, and A. Engel. Scan speed limit in atomic force micropscopy. *J. Microsc.*, 169(1):75–84, 1993.

[18] H. B. Callen and R. F. Greene. On a theorem of irreversible thermodynamics. *Phys. Rev.*, 86(5):702–710, 1952.

[19] H. B. Callen and A. T. Welton. Irreversibility and generalized noise. *Phys. Rev. Lett.*, 83(1):34–40, 1951.

[20] C. Carvajal. The fluid-coupled motion of micro and nanoscale cantilevers. Master's thesis, Virginia Tech, 2007.

[21] D. Chandler. *Introduction to Modern Statistical Mechanics.* Oxford University, Press, 1987.

[22] J. W. M. Chon, P. Mulvaney, and J. E. Sader. Experimental validation of theoretical models for the frequency response of atomic force microscope cantilever beams immersed in fluids. *J. Appl. Phys.*, 87(8):3978–3988, 2000.

[23] L.A. Chtcheglova, G.T. Shubeita, S.K. Sekatskii, and G. Dietler. Force spectroscopy with a small dithering of afm tip: A method of direct and continuous measurement of the spring constant of single molecules and molecular complexes. *Biophys. J.*, 86:1177–1184, 2006.

[24] M.T. Clark. The stochastic dynamics of an array of atomic force microscopes in viscous fluid. Master's thesis, Virginia Tech, July 2006.

[25] M.T. Clark and M.R. Paul. The stochastic dynamics of an array of atomic force microscopes in viscous fluid. *Int. J. Non. Mech.*, 42(4):690–696, May 2007.

[26] M.T. Clark and M.R. Paul. The stochastic dynamics of rectangular and v-shaped atomic force microscope cantilevers in a viscous fluid and near a solid boundary. *J. Appl. Phys.*, 103:094910, 2008.

[27] M.T. Clark, M.R. Paul, J. E. Sader, and J.P. Cleveland. The driven dynamics of micro and nanoscale cantilevers in a viscous fluid. *To be published*, 2009.

[28] R. J. Clarke, S. M. Cox, P. M. Williams, and O. E. Jensen. The drag on a microcantilever oscillating near a wall. *J. Fluid Mech.*, 545:397–426, 2005.

[29] R. J. Clarke, O.E. Jensen, J. Billingham, A.P. Pearson, and P.M. Williams. Stochastic elastohydrodynamics of a microcantilever oscillating near a wall. *Phys. Rev. Lett.*, 96(5):050801, 2006.

[30] R. J. Clarke, O.E. Jensen, J. Billingham, and P.M. Williams. Three-dimensional flow due to a microcantilever oscillating near a wall: an unsteady slender-body analysis. *Proc. R. Soc. A*, 462:913–933, 2006.

[31] R.J. Clarke, O.E. Jensen, and J. Billingham. Three dimensional elastohydrodynamics of a thin plate oscillating above a wall. *Phys. Rev. E*, To be published, 2008.

[32] J.P. Cleveland, S. Manne, D. Bocek, and Hansma P.K. A nondestructive method for determining the spring constant of cantilevers for scanning force microscopy. *Rev. Sci. Instrum.*, 64(2):403–405, 1993.

[33] H. Craighead. Nanoelectromechanical systems. *Science*, 290:1532–1535, 2000.

[34] Z.G. Djuric and I.M. Jokic. Thermomechanical noise of nanooscillators with time-dependent mass. *Microelectronic Engineering*, 84:1639–1642, 2007.

[35] A. Einstein. On the motion—required by the molecular kinetic theory of heat—of small particles suspended in stationary liquid. *Annalen der Physik*, 17:549, May 1905.

[36] K. L. Ekinci and M. L. Roukes. Nanoelectromechanical systems. *Rev. Sci. Instrum.*, 76(6), 2005.

[37] R. Erlandsson, G.M. McClellan, C.M. Mate, and S. Chiang. Atomic force microscopy using optical interferometry. *J. Vac. Sci.*, 6(2):266–270, 1988.

[38] ESI CFD Headquarters, Huntsville AL 25806. We use the CFD-ACE+ solver.

[39] R.P. Feynman. There's plenty of room at the bottom. *Engineering and Science, Caltech*, 1960.

[40] R. Garcia and R. Perez. Dynamic atomic force microscopy methods. *Surf. Sci. Rep.*, 47:197–301, 2002.

[41] M. K. Ghatkesar, T. Braun, V. Barwich, J.-P. Ramseyer, C. Gerber, M. Hegner, and H.P. Lang. Resonating modes of vibrating microcantilevers in liquid. *Appl. Phys. Lett.*, 92:043106, 2008.

[42] F. J. Giessibl. Advances in atomic force microscopy. *Rev. Mod. Phys.*, 75:949–983, 2003.

[43] C. P. Green and J. E. Sader. Frequency response of cantilever beams immersed in viscous fluids near a solid surface with applications to the atomic force microscope. *J. Appl. Phys.*, 98:114913, 2005.

[44] C. P. Green and J. E. Sader. Small amplitude oscillations of a thin beam immersed in a viscous fluid near a solid surface. *Phys. Fluids*, 17:073102, 2005.

[45] P. K. Hansma, J. P. Cleveland, M. Radmacher, D. A. Walters, P. E. Hillner, M. Benzanilla, M. Fritz, D. Vie, H. G. Hansma, C. B. Prater, J. Massie, L. Fukunaga, J. Gurley, and V. Elings. Tapping mode atomic force microscopy in liquids. *Appl. Phys. Lett.*, 64(13):1738–1740, 1994.

[46] C. Harrison, E. Tavernier, O. Vancauwenberghe, E. Donzier, K. Hsu, A.R.H. Goodwin, F. Marty, and B. Mercier. On the response of a resonating plate in a liquid near a solid wall. *Sens. Actuators, A*, 134:414–426, 2007.

[47] W. Heisenberg. The development of quantum mechanics. Nobel Lecture, 1932.

[48] R. Hooke. *Micrographi: Or some physiological descriptions of minute bodies, made by magnifying glasses, with observations and inquiries thereupon.* Dover Phoenix Editions, 1664.

[49] L. D. Landau and E. M. Lifshitz. *Theory of elasticity.* Butterworth-Heinemann, 1959.

[50] Y. Martin, C. C. Williams, and H. K. Wickramasinghe. Atomic force microscope force mapping and profiling on a sub 100-a scale. *J. Appl. Phys.*, 61:4723–4729, 1987.

[51] J. C. Meiners and S. R. Quake. Direct measurement of hydrodynamic cross correlations between two particles in an external potential. *Phys. Rev. Lett.*, 82(10):2211–2214, 1999.

[52] J. Melcher, S. Hu, and A. Raman. Equivalent point-mass models of continuous atomic force microscope probes. *Appl. Phys. Lett.*, 91:053101, 2007.

[53] I. Nnebe and J. W. Schneider. Characterization of distance-dependent damping in tapping-mode atomic force microscopy force measurements in liquid. *Langmuir*, 20:3195–3201, 2004.

[54] C. Oatley. Scanning electron-microscope and other electron-probe instruments. *Proc. Inst. Elec. Eng.-London*, 122(9):942–946, 1975.

[55] L. O'Connor. MEMS: Microelectromechanical systems. *ASME*, 114(2):40–47, 1992.

[56] Olympus, http://www.olympus.co.jp/en/insg/probe/en/specsisoftE.html.

[57] L. Onsager. Reciprocal relations in irreversible processes. ii. *Phys. Rev.*, 38:2265–2279, 1931.

[58] R. L. Panton. *Incompressible fluid flow*. Wiley, 2005.

[59] M. R. Paul, M.T. Clark, and M. C. Cross. Stochastic dynamics of micron and nanoscale elastic cantilevers in fluid: fluctuations from dissipation. *Nanotechnology*, 17:4502–4513, 2006.

[60] M. R. Paul and M. C. Cross. Stochastic dynamics of nanoscale mechanical oscillators immersed in a viscous fluid. *Phys. Rev. Lett.*, 92(23):235501, 2004.

[61] M. Planck. Ueber electrische schwingungen, welche durchresonanz erregt und durch strahlung gedämpft werden. *Annalen der Physik und Chemie*, 296(4):577–599, 1897.

[62] W.H. Press, S.A. Teukolsky, W.T. Vetterling, and B.P. Flannery. *Numerical Recipes in C*. Cambridge University Press, New York, 1992.

[63] M. Radmacher, M. Fritz, H. Hansma, and P. K. Hansma. Direct observation of enzymatic activity with the atomic force microscope. *Science*, 265:1577–1579, 1994.

[64] A. Raman, J. Melcher, and R. Tung. Cantilever dynamics in atomic force microscopy. *Nano Today*, 3(1-2):20–27, 2008.

[65] L. Rosenhead. *Laminar Boundary Layers*. Oxford University Press, 1963.

[66] M. L. Roukes. Nanoelectromechanical systems. condmat/0008187, 2000.

[67] E. Rutherford, J. Chadwick, and C. D. Ellis. *Radiation from Radioactive Substances*. Cambridge University Press, New York, 1919.

[68] J. E. Sader. Parallel beam approximation for v-shaped atomic force cantilevers. *Rev. Sci. Instrum.*, 66(9):4583–4587, 1995.

[69] J. E. Sader. Frequency response of cantilever beams immersed in viscous fluids with applications to the atomic force microscope. *J. Appl. Phys.*, 84(1):64–76, 1998.

[70] J. E. Sader and L. White. Theoretical-analysis of the static deflection of plates for atomic-force microscope applications. *J. Appl. Phys*, 74(1):1–9, 1993.

[71] T. E. Schaffer and P. K. Hansma. Characterization and optimization of the detection sensitivity of an atomic force microscope for small cantilevers. *J. Appl. Phys.*, 89(9):4661–4666, 1998.

[72] K. C. Schwab and M. L. Roukes. Putting mechanics into quantum mechanics. *Phys. Today*, 58:36–42, 2005.

[73] Sir G.G. Stokes. The effect of the internal friction of fluids on the motion of pendulums. *Trans. Camb. Phil. Soc.*, 9:8, 1850.

[74] E. O. Tuck. Calculation of unsteady flows due to small motions of cylinders in a viscous fluid. *J. Eng. Math*, 3(1):29–44, 1969.

[75] C. A. van Eysden and J. E. Sader. Frequency response of cantilever beams immersed in viscous fluids with applications to the atomic force microscope: Arbitrary mode order. *J. Appl. Phys.*, 101:044908, 2007.

[76] Veeco Probes, www.veecoprobes.com.

[77] S.S. Verbridge, L.M. Bellan, J.M. Parpia, and H.G. Craighead. Optically driven resonance of nanoscale flexural oscillators in liquid. *Nano Lett.*, 6(9):2109–2114, 2006.

[78] M. B. Viani, T. E. Schaffer Schaffer, and A. Chand. Small cantilevers for force spectroscopy of single molecules. *J. Appl. Phys.*, 86(5):2258–2262, 1999.

[79] M. Villa and M. R. Paul. The effects of geometry on the dynamics of microscopic cantilevers in fluid. Unpublished.

[80] E. Voltera and E. Zachmanoglou. *Dynamics of Vibrations*. Charles E. Merrill Books, 1965.

[81] M. von Ardenne. Development of the scanning electron microscope., 1937.

[82] G. M. Whitesides. The 'right size' in nanobiotechnology. *Nat. Biotechnol.*, 21(10):1161–1165, 2003.

[83] X. Xu and A. Raman. Comparative dynamics of magnetically, acoustically, and brownian motion driven microcantilevers in liquids. *J. Appl. Phys.*, 102:034303, 2007.

[84] H. Q. Yang and V. B Makhijani. A strongly-coupled pressure-based CFD algorithm for fluid-structure interaction. *AIAA-94-0179*, pages 1–10, 1994.